

Calibration of the Neutral Gas and Ion Mass Spectrometer for the JUpiter ICy moons Explorer

**Inauguraldissertation der
Philosophisch-naturwissenschaftlichen Fakultät der
Universität Bern**

**vorgelegt von
Martina Föhn**

2021

**Leiter der Arbeit
Prof. Dr. Peter Wurz**

Physikalisches Institut der Universität Bern

Abstract

The JUPiter ICy moons Explorer (JUICE) of the European Space Agency (ESA) has the purpose to investigate Jupiter and his icy moons Europa, Ganymede and Callisto. JUICE will investigate the Jupiter system as a potential habitable system because the three icy moons have subsurface oceans where life might be possible. On board of JUICE is the Particle Environment Package (PEP), which consists of six individual sensors measuring electrons, ions and neutral particles in an energy range from meV up to MeV. One of these six sensors is the Neutral gas and Ion mass spectrometer (NIM). The NIM instrument is designed to measure the chemical and isotope composition of the icy moons' exospheres during the flybys of JUICE on the icy moons and also during JUICE final destination on Ganymede. The chemical and isotope composition allow a better understanding of the formation processes involved in the formation of the icy moons and our solar system.

NIM is a time-of-flight mass spectrometer able to measure thermal neutral molecules and ionospheric ions. This contribution shows the journey from finalizing the flight design of the NIM instrument to the actual testing and delivery of the NIM Proto-Flight (PFM) sensor in December 2020 to the JUICE spacecraft. On this journey, different flight components were tested and analysed as they came available during the development and finalization of the Proto-Flight (PFM) and Flight-Spare (FS) sensor. The two NIM sensors have a demonstrate mass resolution $m/\Delta m$ of 750 (FWHM) for the PFM and 850 for the FS. Both sensors have a SNR of almost 6 decades.

Contents

1. Introduction	1
1.1. Mission Introduction	1
1.2. Thesis Outline	4
2. Theory	7
2.1. Mass Resolution Corrections completed	8
2.2. Signal-to-Noise Ratio finished	15
2.3. Filament Draft	15
2.3.1. Power Calculation finished	16
2.3.2. Flight Filament Controller Boards Characterisation	17
2.4. Ion Storage Corrections completed	19
2.5. Density enhancement of a Closed Source finished	21
2.6. Field-of-View Analysis finished	28
2.7. Shutter Performance finished	34
2.8. Multichannel Plates finished	36
2.8.1. Gain	37
2.8.2. Dead time	39
3. Instrument	41
4. Experiments	50
4.1. Flight Ion-Mirror Finished	50
4.2. Flight Antechamber finished	51
4.3. Density Enhancement finished	53
4.4. Entrance Ion and Electron Position Simulations	56
4.5. Shutter Performance Test finished	61
4.6. Pulser finished	62
4.7. Detector Tests finished	63
4.8. Sensor performance tests	67
4.8.1. PFM	67
4.8.2. FS finished	68
5. Conclusion	73
6. Outlook	77
References	78
A. Appendix	82
A.1. Papers	82
A.2. Datasheets	82

List of Acronyms

ADC	Analog-to-Digital Converter
ESA	European Space Agency
FoV	Field-of-View
FS	Flight-Spare Model
FWHM	Full Width at Half Maximum
JDC	Jovian plasma Dynamics and Composition analyzer
JEI	Jovian Electrons and Ions
JENI	Jovian Energetic Neutrals and Ions
JNA	Jovian Neutrals Analyzer
JoEE	Jovian Energetic Electrons
JUICE	JUperiter ICy moon Explorer
MCP	Multi-Channel-Plate
MEAP	Mars Environment Analog Platform
NIM	Neutral Gas and Ion Mass Spectrometer
NGMS	Neutral Gas Mass Spectrometer
P-BACE	Polar Balloon Atmospheric Composition Experiment
PCB	Printed Circuit Board
PEP	Particle Environment Package
PFM	Proto-Flight Model
ROSINA	Rosetta Orbiter Spectrometer for Ion and Neutral Analysis
RTG	Radioisotope Thermoelectric Generators
RTOF	Reflectron Time-Of-Flight mass spectrometer
S/C	Spacecraft
SNR	Signal-to-Noise Ratio
TF	Time focus
TOF	Time-Of-Flight

1. Introduction

1.1. Mission Introduction

Investigation of the stars and the night sky started a long time ago. The back then, the movement of the Sun, the Moon and the stars was used to derive time, for navigation and for religious rituals. First records of systematic observations of the night sky date back to the Assyro-Babylonians around 1000 BCE. In the third century BCE Greek astronomers tried to estimate the distances between the different cosmic objects with geometrical tools [3]. The invention of telescopes in the early 17th century allowed then a closer look at the objects in the night sky and lead to the discovery of the Galilean moons' Io, Europa, Callisto and Ganymede by Galileo Galilei in 1610. Galileo discovered that these objects were orbiting around another object than the Sun (Jupiter).

The invention of the first modern rockets during the cold war, opened the opportunity of on site exploration of solar system bodies. The data acquired through those in situ measurements gave further insight into the formation processes and history of our solar system. The missions Pioneer 10 & 11 and Voyager 1 & 2 were the first space missions, which took close images of Jupiter and its icy moons. They discovered Jupiter's ring system and detected more small moons of Jupiter than only the four big Galilean moons. The missions Galileo (1995-2003) and JUNO (2016-2025) were two missions specifically with the objective to further investigate Jupiter itself (JUNO) and its icy moons (Galileo) with the main outcome of giving strong evidence for salty subsurface oceans on the moons Europa, Ganymede and Callisto by measuring the induced magnetic fields. These oceans could be environments where life might be possible. In addition, Galileo observed that Ganymede has an intrinsic magnetic field interacting with the strong magnetic field of Jupiter [40].

The Jupiter ICy moons Explorer JUICE built by the European Space Agency ESA has the objective to further investigate Jupiter, its environment and its icy moons with regards to their potential of harbouring life. JUICE will characterise Jupiter as a planet, Jupiter's plasma environment and it will characterise Jupiter's icy moons Europa, Ganymede and Callisto. JUICE will characterise Jupiter's atmospheric dynamics, composition and chemistry and the atmo-



Figure 1: Artist impression of the Juice mission exploring the Jupiter system [14].

sphere's vertical structure. It will characterise Jupiter's magnetosphere to understand the role of the moons as sources and sinks for the magnetospheric plasma. JUICE will study Jupiter's ring system, its small satellites and it will study Io's activity and surface composition with its remote sensing instruments.

With regards to the icy moons, the main objectives are to characterise their potential subsurface oceans and their non-icy material. Europa consists mainly out of silicates with a water layer and an ice crust on top of that. Europa's surface is fairly young showing almost no impact craters which implies that the icy layer frequently moves similar to plate tectonics. Ganymede is until now the only satellite in our solar system known having an intrinsic magnetic field generated by a magnetic dipole field. Therefore, JUICE will investigate the interaction processes of that magnetic field with Jupiter's magnetic field because it is strong enough to successfully shield the moon against the plasma flow from Jupiter's magnetosphere. Callisto is the outer most of the Galilean moons and by far the most cratered. It lacks of small craters indicating some minor erosion processes. Compared to the other three Galilean moons, Callisto lacks any greater tectonic activity [24].

To fulfil the scientific goals, JUICE has an instrument suit consisting of 11 instruments on

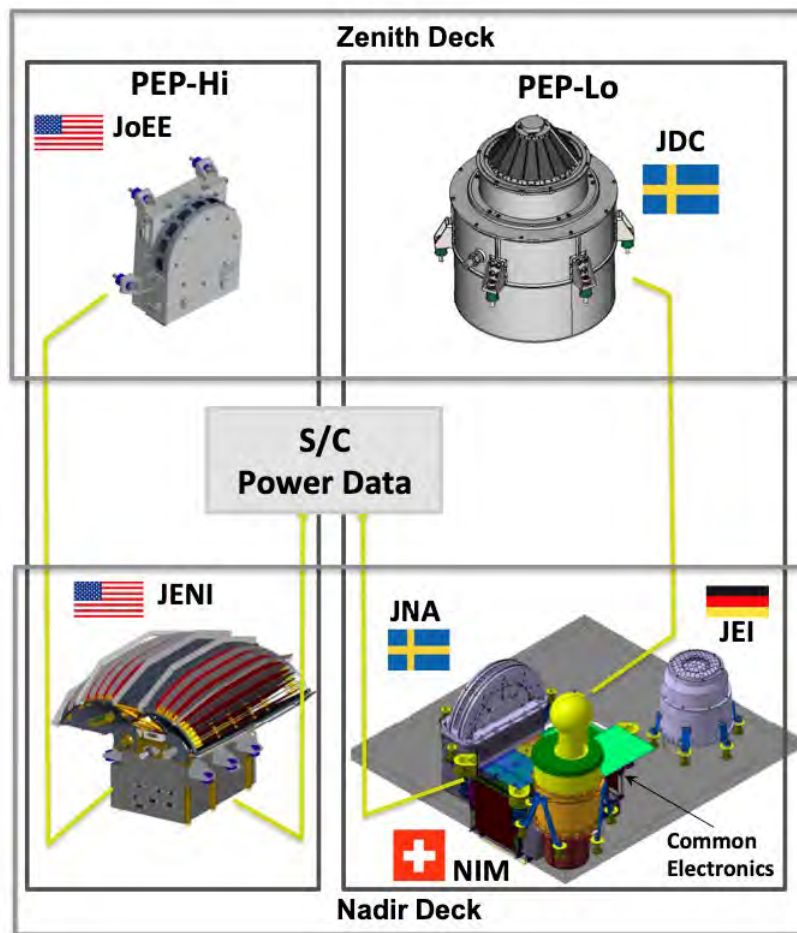


Figure 2: Sketch of the six PEP instruments [8].

board ranging from cameras to magneto and gravity meters to particle detectors. One of these instruments is the Particle and Environment Package System PEP (Fig. 2). The main focus of PEP is to characterise Jupiter's plasma environment and the composition of the icy moons' exosphere. Therefore, PEP has six sensors to measure neutral particles, ions and electrons with energies from thermal (< 5 eV) up to 5 MeV (ions) [8]. One of these six sensors is the Neutral Gas and Ion Mass Spectrometer NIM. The focus of NIM lays on the characterisation of the icy moons exosphere and the detection of ions with an energy less than 100 eV to complete the plasma measurements for slow ions of the other PEP instruments. With the capability of measuring slow ions, NIM is able to detect a potential ionosphere of the icy moons [30]. NIM will be the first mass spectrometer taking in situ measurements of the icy moons exosphere. The exosphere is formed by particles released from the moons' surface by ion bombardment, sublimation and photon interaction processes. By sampling the exosphere, we get a deeper insight in the surface composition and the formation processes involved of the icy moons themselves. For example, there are two major theories about when the icy moons were formed. One suggests that the icy moons' were formed in the protostar nebula of our solar system implying that the moons have a similar age as Jupiter. Another hypothesis suggests that the icy moons' were formed in the subnebula of Jupiter, implying that they are younger than Jupiter. By determining the particle density and isotope ratios of the detected species, we can distinguish between these two formation processes giving us a deeper insight in how our solar system was formed and which processes in the formation of the icy moons' are the most relevant [39, and references therein].

The instruments sent to space missions are customised to fulfil the specific requirements. For space missions, the instruments have to be small, light and low power consumptive. Especially for missions having targets in the outer solar system, such as JUICE with target Jupiter, power is a very limited resource. At Jupiter, the solar flux density is by a factor 25 lower than at Earth because Jupiter is five times farther away from the Sun than Earth. Therefore, missions flying to the outer solar system often use radioisotope thermoelectric generators (RTGs) as power sources instead of solar panels because they are longer lasting and provide more power. The biggest drawback is that they are very inefficient and produce a lot of heat, which cannot be used [25]. Another main challenge is the harsh radiation environment of Jupiter. The penetrating particles lead to upset in the electronics and damage components. Therefore, a proper shielding concept was necessary.

NIM is a time-of-flight mass spectrometer with heritage from previous TOF instruments developed at the university of Bern. These are the RTOF/ROSINA/Rosetta [7, 35], P-BACE/MEAP [2] and NGMS/Luna-Resurs [44, 16]. Mass spectrometers are single ion counting instruments. Therefore, they can estimate the density distributions of the measured species much more precisely than remote sensing instruments. The biggest advantages of time-of-flight mass spectrometers compared to other mass spectrometer types is that they are extremely robust from the mechanical point of view and have a better sensitivity than scanning instruments. Magnetic sectors are heavy and require high accuracy mechanics. Quadrupole mass spectrometers fulfil the requirements regarding size, weight and power but have a lower sensit-

ivity than TOF instruments because to increase the mass resolution they loose sensitivity [18]. In addition, scanning instruments have a relatively long cadence [6] leading to a bad spacial resolution during the flybys of the spacecraft on the icy moons. Therefore, TOF instruments are often used in space missions.

NIM is designed to measure complex molecules up to 1000 u with a mass resolution up to $m/\Delta m$ 1000 with a signal-to-noise ratio (SNR) of 6 decades. In the icy moons exosphere we only expect species with masses up to 100 u but with the ability to measure also species with higher masses, NIM is able to detect also potential organic compounds if they are present [4]. To separate species with such high masses, it requires a mass resolution of $m/\Delta m$ 1000 to be able to distinguish between the different unit masses. With a SNR of 6 decades, NIM is able to measure down to partial pressures of 10^{-16} mbar corresponding to a particle density of 1 cm^{-3} . During the flybys at the icy moons, the spacecraft velocity is 1-8 km/s. Depending on the mass of the particles, the highest energy they have is up to 100 eV which is the highest energy NIM has to deal with. NIM is designed to measure particles with thermal energy up to energies of 100 eV. NIM has an open and a closed source entrance for neutral particles and ions. Through the open source entrance slit, neutral particles and ions enter the ionisation region directly without interacting with the instrument structure. The closed source consists of an antechamber which thermalises incoming neutrals. Neutrals with higher speeds are therefore easier to detect than with the open source channel where particles enter the ionisation region with spacecraft velocity. As mentioned above, mass and power are for these missions very limited resources. The NIM ion-optical system has a mass of 3.13 kg from which 48 % is shielding mass to shield the detector locally to reduce noise induced by high energetic particles originating from Jupiter's plasma environment. The power allocated for the NIM instrument from the spacecraft is 18.5 W.

1.2. Thesis Outline

This thesis follows up the PhD thesis of Stefan Meyer [30]. At the end of his thesis, the NIM prototype was built and the flight design the NIM was almost completed.

The objective of this thesis was to finalize the design of the NIM flight model, to build and test the NIM PFM to deliver it to the JUICE spacecraft and to build and test the NIM Flight-Spare (FS) model, which stays on Earth as a ground reference. This required environmental tests of various flight subcomponents as they came available with finally testing the ion-system of the NIM PFM and FS sensor. Ion-optical simulations were performed to set constrains on the design of the flight power supplies as they were still under development during the early phases of this thesis.

The thesis consists of three main parts: Chap. 2 shows theoretical analyses of key components of the NIM instrument such as the performance of the closed source antechamber. In addition, it sums up the theoretical aspects needed to understand the performance results of the different subsystems presented in Chap. 4. Chap. 3 compares the design of the NIM prototype with the final flight design and shows the main differences between the two models. A special focus lays there in the improvements done on the design of the detector. Chap. 4 sums up the performance tests of different subsystems partially tested stand alone (detector) or as part of

the NIM Prototype (antechamber, ion-mirror). The chapter ends with performance tests of the two NIM flight models (PFM and FS).

2. Theory

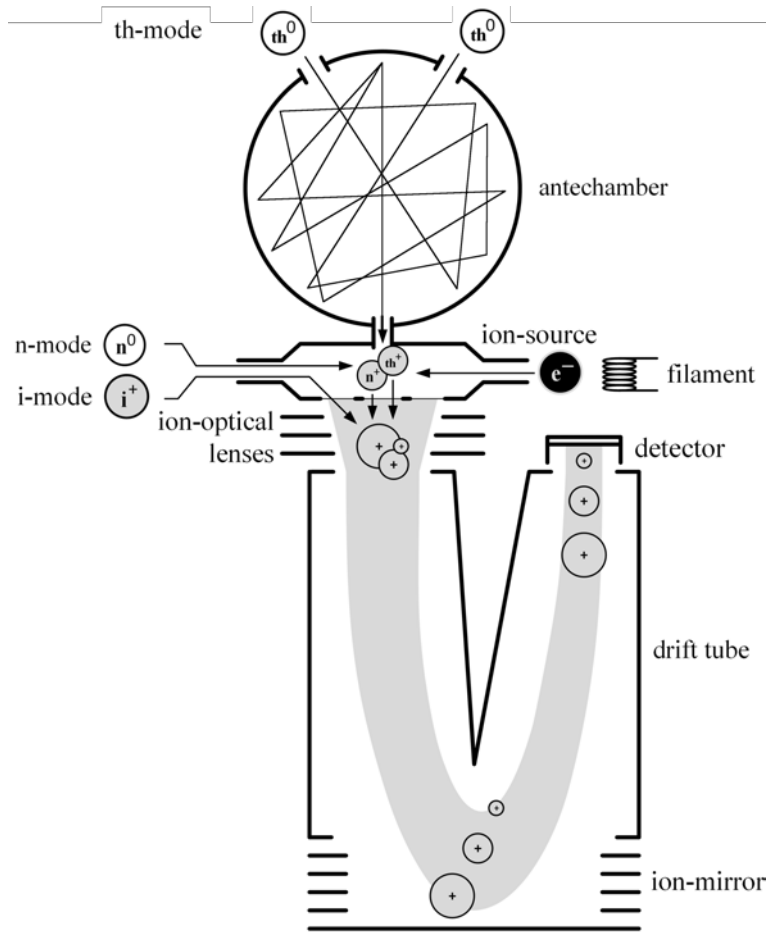


Figure 3: Schematics of the NIM mass spectrometer. Adapted from [30].

NIM is a time-of-flight mass spectrometer consisting of an ion-source, a mass analyser and a detector. Fig. 3 shows a schema of the NIM ion-optical system. Gaseous particles enter the ion-source either through a closed source antechamber where they get thermalized or directly through an entrance slit. When particles enter through the antechamber, the measuring mode is called thermal mode (th-mode). When neutral particles enter through the entrance slit, the mode is called neutral mode (n-mode) and when ions enter the slit, the mode is called ion mode (i-mode). The neutral particles are ionized by electron impact ionization. A filament is heated until it emits electrons. The electrons are accelerated up to an energy of about -70 eV. In the ionization region, the electrons knock out electrons from the neutral gas generating positive ions. The ions are then accelerated to an energy of about 250 eV by applying a high voltage pulse on the extraction grid. NIM has a two-field ion source meaning that with the ion-optical lenses the ions are additionally accelerated and focused to compensate when the ions have different initial energies. Light species fly faster through the spectrometer than heavier ones resulting in a separation of the species by their mass. An ion-mirror is used to increase the

flight distance and to refocus ions of the same species with different energies. The ions are detected with a Multi-Channel-Plate (MCP) detector.

This chapter gives an overview from the theoretical perspective over the different subunits of the NIM ion-optical system. Chap. 4 shows test results of the different subunits and performance tests of the NIM Prototype, the NIM Proto Flight Model (PFM) and the Fligh Spare (FS) models.

2.1. Mass Resolution **Corrections completed**

The generated ions in the ion-source are trapped in the centre by the potentials of the electrodes and the electron beam. The ions are extracted by a high voltage pulse applied onto the extraction grid. All ions are accelerated to the same energy W :

$$W = \int_0^{s_0} qE_s ds = \frac{qU_0}{2} \quad (1)$$

With s_0 the distance from the centre of the ion-source to the extraction grid corresponding to half the height of the ion-source. q is the particle charge, E_s is the applied electric extraction field strength induced by the voltage U_0 applied on the extraction grid. The ions start in the centre of the ion-source. Therefore, they have the kinetic energy $qU_0/2$ when reaching the extraction grid:

$$\frac{qU_0}{2} = \frac{1}{2}mv^2 \quad (2)$$

With m and v the mass and velocity of the ion. Rearranging this formula results in:

$$\frac{m}{q} = U_0 \frac{t^2}{D^2} \quad (3)$$

With t the time of flight and D the flight distance from the extraction grid to the detector. U_0 and D^2 are merged into one constant C resulting in:

$$\frac{m}{q} = C(t - t_0)^2 \quad (4)$$

t_0 corresponds to a time offset between the start of the mass axis and the time axis. The two calibration constants C and t_0 are determined by at least knowing two species in the mass spectrum. The correctness of the mass scale can be verified by checking the other mass peaks in the mass spectrum, which all have to be on integer masses, ignoring the small deviations for now. The mass is therefore proportional to t^2 :

$$m = c \cdot t^2 \quad (5)$$

The derivative is:

$$\frac{dm}{dt} = 2ct \quad (6)$$

$$dm = 2ct \cdot dt \quad (7)$$

Dividing Eq. (5) through Eq. (7) results in:

$$\frac{m}{dm} = \frac{ct^2}{2 \, ct \cdot dt} \quad (8)$$

$$\frac{m}{dm} = \frac{t}{2 \, dt} = \frac{\mu}{2 \cdot FWHM} \quad (9)$$

With μ the centre of the mass peak in the time domain and $FWHM$ is the full width at half maximum of the mass peak [43].

In the following section, the different contributions affecting the mass resolution are analysed. The focus is on the contributions originating from the ion source because they have the biggest impact on the mass resolution of the instrument.

The total time spread dt_i of the signal of a particle species i at the detector is:

$$dt_i = \sqrt{\sum_k dt_k^2} = \sqrt{dt_D^2 + dt_{ADC}^2 + dt_{th}^2 + dt_s^2 + dt_{tfall}^2} \quad (10)$$

With the different contributions dt_k . When an ion hits the detector, it generates a charge pulse with pulse width dt_D . For the NIM detector, the pulse width is ~ 0.7 ns. The generated pulse is converted into a digital signal with an analog-to-digital converter (ADC). The ADC used in the laboratory has a sampling rate of 4 GHz resulting in a time resolution dt_{ADC} of 0.25 ns. The flight ADC has a maximal sampling rate of 2 GHz corresponding to a time resolution of 0.5 ns.

The time spreads resulting from the thermal energy of the ions dt_{th} , from the different start positions of the ions within the ionisation region dt_s and from the fall time of the high voltage pulse dt_{tfall} are coupled because they all affect the energy deviation of the ions. Initially, the ions in the ion-source have thermal energy W_{th} :

$$W_{th} = \frac{3}{2} \cdot k_B \cdot T \quad (11)$$

With k_B the Boltzmann constant and T the temperature. The thermal energy leads to an initial velocity distribution of the ions with a mean velocity of v_{init} (Fig. 4 top panel). Ions number 1 and 3 have the same thermal energy but one is directed towards the extraction grid where the other one is directed towards the backplane. When a high voltage pulse is applied on the extraction grid, ion number 3 has to be turned around. The time difference between ions 1 and 3 is called turn-around time. At a certain point in time, ion 3 will overtake ions with less energy (ion 2). The turn-around time cannot be corrected with the ion optics. The only option to reduce the turn-around time would be to cool the ions, which is not possible for a space instrument.

The total energy W the ions get in the ionisation region is:

$$W = \int_{s_{init}}^{s_0} q \cdot E(t) \cdot ds \quad (12)$$

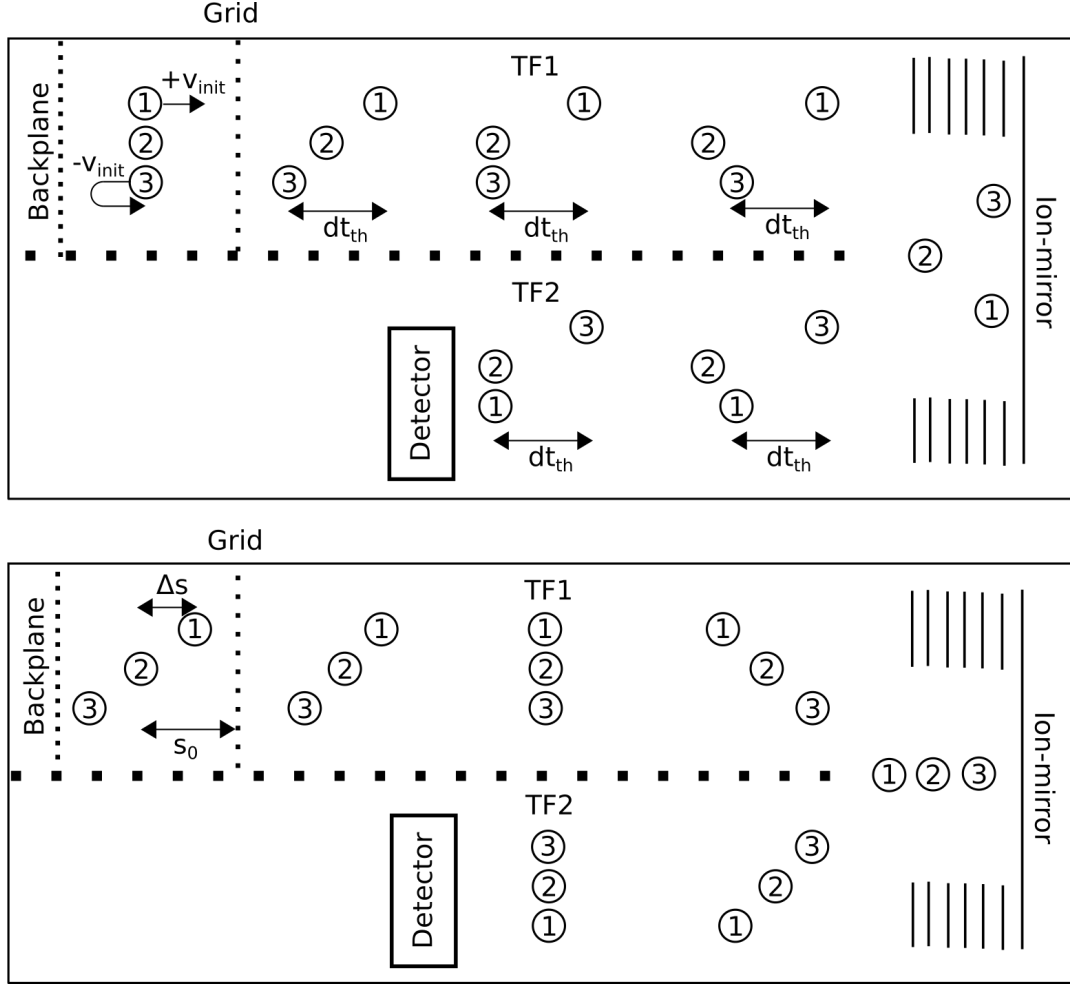


Figure 4: Flight path of ions with different thermal energy (top panel) and start positions (lower panel). v_{init} is the initial velocity of the ions and dt_{th} the turn-around time. $TF1$ and $TF2$ are the locations of the first and second time focus respectively.

With s_{init} the initial position of the ions, s_0 the distance from the centre of the ionisation region to the acceleration grid, q the particle charge and $E(t)$ the electric field strength depending on the time t . When the ions start at different positions in the ionisation region s_{init} , they receive a different amount of energy because their flight distance in the acceleration field is different (Fig.4 lower panel). At a certain distance on the flight path, ions with higher energy will overtake ions with lower energy. The time deviation induced by the different start positions of the ions is dt_s . With a two-field ion source, like NIM, dt_s can be minimized at the first time focusing point $TF1$. With an ion-mirror ions with an energy deviation up to 10% are refocused. Ions with higher energy penetrate deeper into the ion-mirror resulting in a longer flight path of the higher energetic ions. The best position for the detector is when all ions with different energies are at the same position, which is at the time focus of the ion mirror $TF2$.

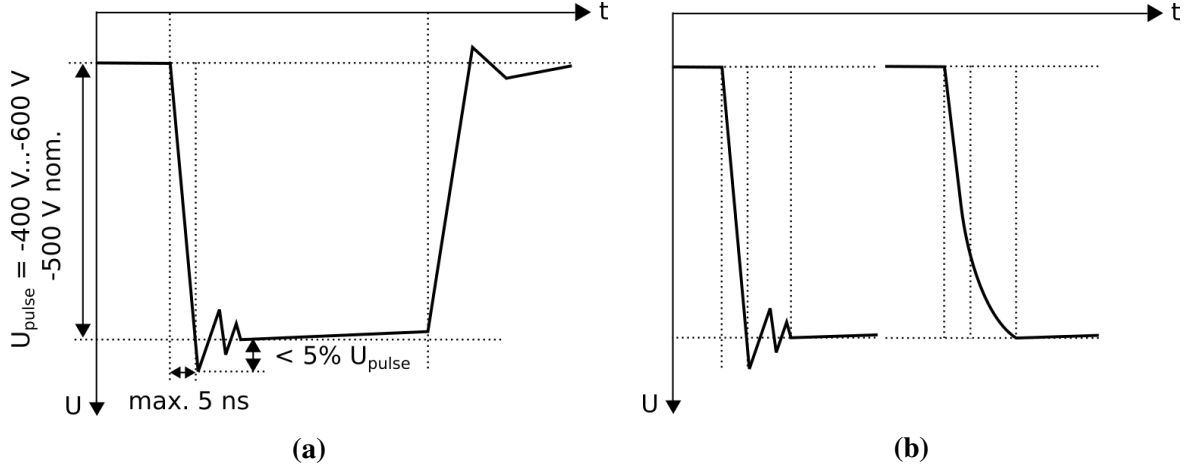


Figure 5: a) Shape of a realistic high voltage pulse applied on the extraction grid. b) Two different possible shapes of the falling edge of the high voltage pulse.

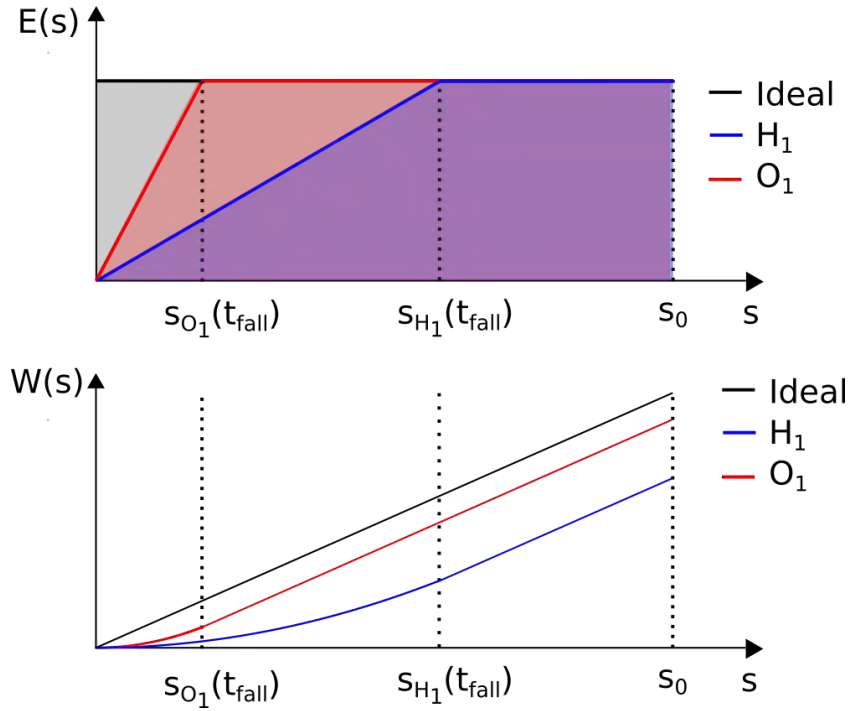


Figure 6: Top panel: Electric field $E(s)$ an ion experiences, as a function of the distance between the centre of the ionisation region and the extraction grid s_0 for two hydrogen (H_1) and oxygen (O_1). $s_i(t_{\text{fall}})$ is the position of the corresponding species at the fall time t_{fall} . Lower panel: Energy $W(s)$ of the ions as a function of their position.

Ideally, the shape of the extraction pulse is a rectangle. Fig. 5a) shows the shape of a realistic extraction pulse. The pulse needs the time t_{fall} to build up the extraction potential on

the extraction grid. Fig. 6 top shows the changing electric field as a function of the position for atomic hydrogen (H_1) and oxygen (O_1) in case when these two species start at the same position. The total energy W of the ions corresponds to the area under the curves. The energy as a function of the flight distance s in the ionisation region and is plotted on the bottom panel of Fig. 6. Hydrogen is lighter than oxygen and therefore, it leaves the ionisation region earlier. This results in a smaller amount of energy for hydrogen than for oxygen. The shorter the fall time of the high voltage pulse is, the smaller is the energy difference because it shifts the position of the ions at the fall time $s_i(t_{fall})$ towards zero. When looking at the shape of the falling edge of the pulse (Fig. 5b), it is more important to have a small fall time with an overshoot than a pulse slowly converging to the maximum because the resulting energy deviation in the first case is much smaller than in the second.

In the following section the influence of the fall time of the high voltage pulse t_{fall} in combination with the longitudinal spacial spread Δs of the ionisation region and the thermal energy of the ions on the mass resolution is analysed. To investigate the impact of these effects, this model does not include any focusing lenses and has no ion-mirror.

The derivation of the equation of motion is based on [1]. The electric field $E(t)$ in the ionisation region is approximated with a linear function during the fall time t_{fall} and as a constant during the rest of the time:

$$E(t) = \begin{cases} E_1 \cdot \frac{t}{t_{fall}}, & (0 \leq t \leq t_{fall}) \\ E_1, & t_{fall} < t \end{cases} \quad (13)$$

E_1 is the electric field strength when the high voltage pulse is fully applied:

$$E_1 = \frac{U_0}{2 \cdot s_0} \quad (14)$$

With U_0 the voltage on the extraction grid. The equation of motion for the ions during the fall time is:

$$a_{fall}(t \leq t_{fall}) = \frac{q \cdot E_1}{m \cdot t_{fall}} \cdot t \quad (15)$$

With a_{fall} the acceleration of the ions and m the ion mass. The velocity of the ions v_{fall} is:

$$v_{fall}(t \leq t_{fall}) = \frac{q \cdot E_1}{2 \cdot m \cdot t_{fall}} \cdot t^2 + v_{init} \quad (16)$$

With v_{init} the initial velocity of the ions before applying the extraction pulse. v_{init} originates from the ion's thermal energy. The position of the ions s_{fall} at the time t is:

$$s_{fall}(t \leq t_{fall}) = \frac{q \cdot E_1}{6 \cdot m \cdot t_{fall}} \cdot t^3 + v_{init} \cdot t + s_{init} \quad (17)$$

With s_{init} the initial position of the ions. When the high voltage pulse is fully applied and the ions did not reach the extraction grid until that time, the acceleration of the ions a_p is:

$$a_p(t > t_{fall}) = \frac{q \cdot E_1}{m} \quad (18)$$

The velocity v_p is:

$$v_p(t > t_{fall}) = \frac{q \cdot E_1}{m} (t - t_{fall}) + v_{fall}(t_{fall}) \quad (19)$$

With $v_{fall}(t_{fall})$ the velocity of the ions at the time t_{fall} . The position s_p is:

$$s_p(t > t_{fall}) = \frac{q \cdot E_1}{2 \cdot m} (t - t_{fall})^2 + v_{fall}(t_{fall})(t - t_{fall}) + s_{fall}(t_{fall}) \quad (20)$$

With $s_{fall}(t_{fall})$ the position of the ions at the time s_{fall} . When the ions leave the ionisation region before full high voltage is applied on the extraction grid, the time they spend in the ionisation region t_{IS} is calculated by setting $s_{fall} = s_0$ and solving the cubic Eq. (17) to t . The velocity v_{Grid} of the ions at the extraction grid is determined by inserting t_{IS} in Eq. (16). When the ions leave the ionisation region after the high voltage is fully applied, the time they spend in the ionisation region t_{IS} is calculated by setting $s_p = s_0$ and solving Eq. (20) to t . The velocity v_{Grid} of the ions at the extraction grid is determined by inserting t_{IS} in Eq. (19). The total flight time of the ions in this model is:

$$t_{TOF} = t_{IS} + t_D \quad (21)$$

With t_D the time of flight the ions need for the distance between the extraction grid and the detector. The mass resolution is calculated according to Eq. (9). To have a measure for the impact of the fall time on the different masses, the deviation R of the mass resolution of ions with a mass/charge ratio i relative to the mass resolution of ions with a mass/charge ratio of 200 is calculated:

$$R = 1 - \frac{m_i / \Delta m_i}{m_{200} / \Delta m_{200}} \quad (22)$$

The mass resolution reaches a plateau for high mass ions (see Fig. 7 left). The deviation R is a measure by what fraction the mass resolution of the low mass particles deviates from that plateau. The mass resolution of mass/charge ratio 200 was taken as a reference.

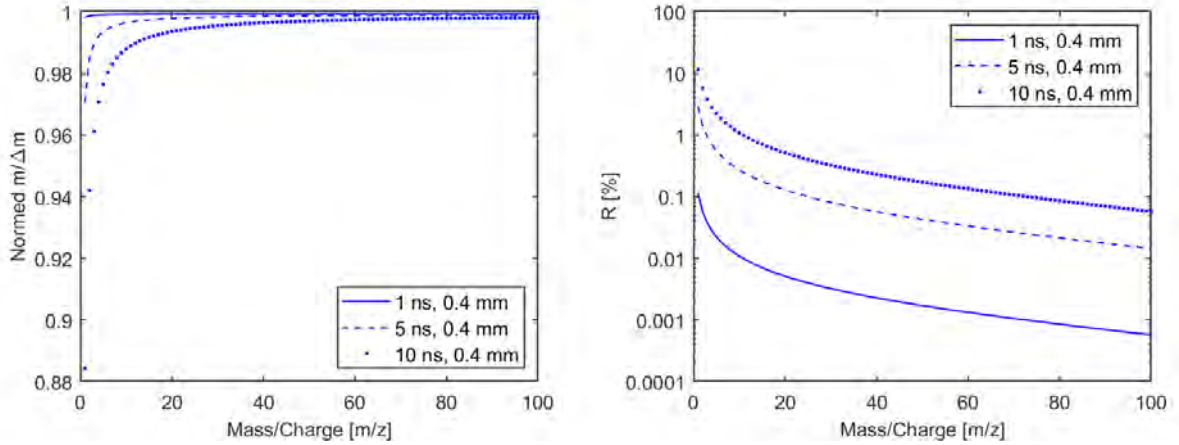


Figure 7: Left: Calculated mass resolution as a function of the mass/charge ratio of the ions for three different fall times of the extraction pulse. Right: relative deviation of the mass resolution from the mass resolution plateau as a function of the mass/charge ratio.

The calculations revealed that the impact of the ion temperature is negligible compared to the impact of the spacial spread Δs and the pulse fall time t_{fall} . The impact of t_{fall} is shown in Fig. 7 left. The position deviation is ± 0.4 mm which corresponds to the diameter of the electron beam in the ionization region. With decreasing fall time, the deviation in mass resolution decreases. This is also visible in the right figure. An improvement in the fall time by one decade results in an improvement of 1 decade of the relative error. With a fall time of 1 ns, the maximum relative deviation is only 10^{-3} . The impact of the fall time is also visible in measurements. Fig. 8 shows measurements with two different pulse generators with fall times of 1.5 ns and 3.5 ns.

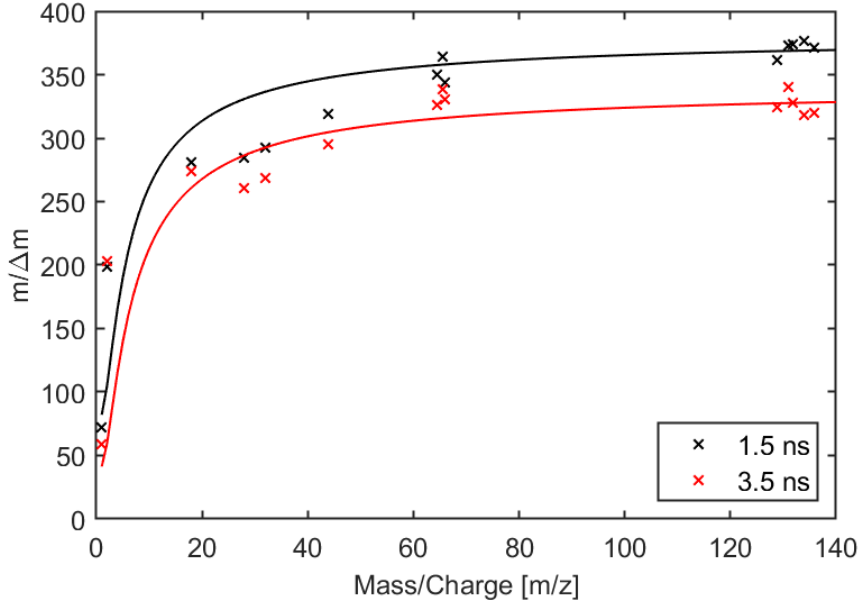


Figure 8: Measurement results of two different pulser generators with 1.5 ns and 3.5 ns fall time. Crosses are measurement points and solid lines are trend lines.

Fig. 9 left shows the mass resolution as a function of the position deviation Δs for mass 1 u. The ionisation region has a diameter of 2 mm. Therefore the maximal deviation of the ions is 1 mm. With increasing Δs the mass resolution drops very rapidly. Therefore it is very important to focus the ions in the centre of the ionisation region. The better the ions are focused, the better is the mass resolution. The relative deviation increases significantly for position deviations close to 1 mm because there, some ions already leave the source when the high voltage pulse is not fully applied.

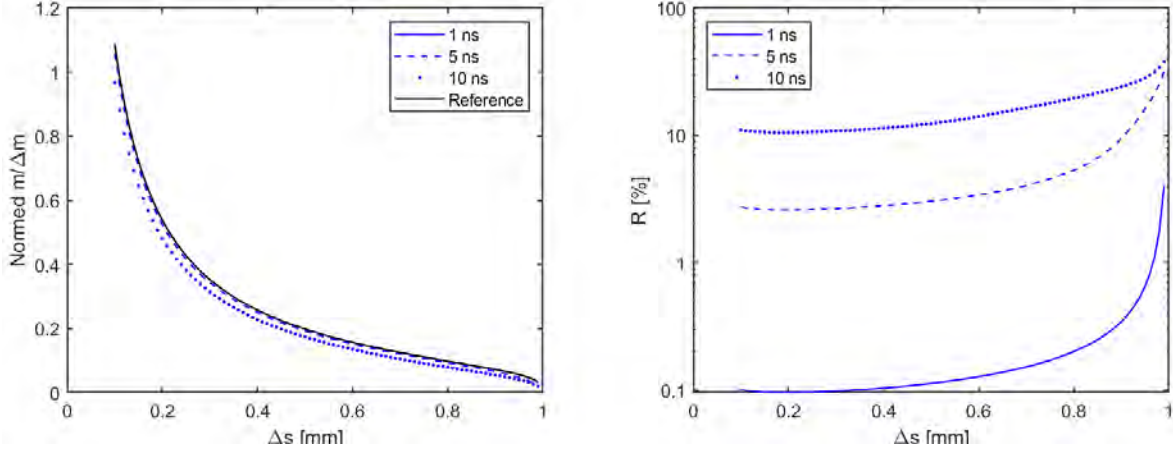


Figure 9: Left: Calculated mass resolution as a function of the spacial spread Δs for three different pulser fall times. Right: relative deviation of the mass resolution from the plateau as a function of the mass/charge ratio.

2.2. Signal-to-Noise Ratio **finished**

The Signal-to-Noise Ratio (SNR) is defined as the ratio of the background corrected mass peak amplitude I_p and the standard deviation of the base line σ_{Base} [20, 29]:

$$SNR = \frac{I_p}{\sigma_{Base}} \quad (23)$$

The number of detected ions is proportional to the area under the detected mass peak. Therefore, a better focusing of the ions leads to a higher and narrower signal peak resulting in a better mass resolution and signal-to-noise ratio. This is a special feature of time-of-flight mass spectrometers. For magnetic sector instruments, the mass resolution is improved by limiting the phase space leading to a loss in signal intensity and therefore a worse signal-to-noise ratio. The noise in the spectrum originates from different sources such as from the electronics operating the instrument. Noise with a fixed frequency is subtracted later from the signal. The random noise induced by high energetic particles from Jupiter's harsh radiation field is damped by shielding the detector with a tungsten copper shield [17]. In addition, NIM has a special designed ion-storage source to store the produced ions during the time when no extraction pulse is applied at the ion extraction grid (Chap. 3). Ions which are produced and not stored in the ionization region are lost and also contribute to the random noise of the measured signal [1].

2.3. Filament **Draft**

NIM uses special designed Y_2O_3 filaments provided by *Kimball Physics, Wilton, USA* to ionise neutral particles entering the ionisation region. These filaments have an enhanced coating Y_2O_3 to enhance the filament lifetime to 10'000 h of operation time. In addition, they have

longer filament wires to reduce the power loss by thermal conductivity (Fig. 10). The longer wires make the filament more delicate in terms of mechanical stress. Therefore, a vibration and shock test were done which showed no anomalies in terms of performance between the normal Y_2O_3 and the special designed Y_2O_3e filaments [15]. In the following sections a power estimation of these filaments is done and also a characterisation of the NIM PFM and FS filament controller boards which provide the power for the filaments in the NIM PFM and FS instruments.

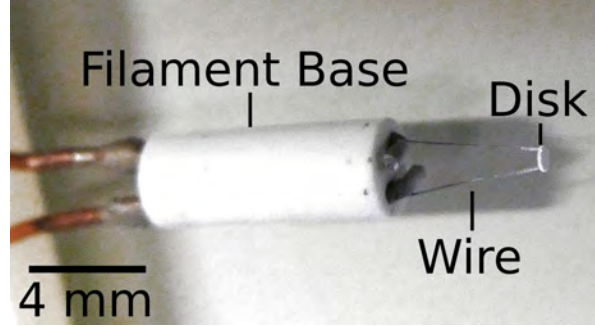


Figure 10: Y_2O_3e filament.

2.3.1. Power Calculation **finished**

In this chapter, the power of the Y_2O_3e filaments (Fig. 10) used in the NIM instrument is estimated and compared with the power consumption of the standard filaments Y_2O_3 filaments. The Y_2O_3 is heated up by the heated current I_{heat} until it emits electrons. The required temperature depends on the desired emission current I_{em} . The Richardson law gives the emission current density j for a material as a function of the temperature T_d :

$$j = A_G T_d^2 e^{-\frac{W}{k_B T_d}} \quad (24)$$

With A_G the Richardson constant which is for Y_2O_3 $10^4 \text{ A m}^{-2} \text{ K}^{-2}$ [11], W is the work function of Y_2O_3 which is 2.4 eV [11] and k_B the Boltzmann constant. The emission current I_{em} is the current density multiplied by the area A_d of the filament disk:

$$I_{em} = j \cdot A_d \quad (25)$$

The total power required to reach the temperature at the disk to emit electrons is the power lost through thermal conductivity P_{cond} through the thin wires connecting the filament disk with the filament base and the power lost through thermal emissivity P_{rad} of the wire and the disk. This power corresponds to the power generated by the resistive losses P_R of the wire:

$$P_R = P_{cond} + P_{rad} \quad (26)$$

The power lost through thermal conductivity is:

$$P_{cond} = 2 \cdot A_w k \frac{dT}{l_w} \quad (27)$$

With A_w the wire cross section, k the thermal conductivity (150 W/Km for W3Re [27] and 150 W/Km for Ir [22]). dT is the temperature difference between the disk and the filament base and l_w the wire length. The factor 2 is because there are two legs connecting the disk with the base. The power lost through thermal radiation P_{rad} is the sum of the power lost by the wire P_{wire} and by the disk P_{disk} :

$$P_{rad} = P_{wire} + P_{disk} \quad (28)$$

$$= 2\sigma \cdot \epsilon_w \cdot A_w T_w^4 + \sigma \cdot \epsilon_{df} \cdot A_d T_d^4 + \sigma \cdot \epsilon_{db} \cdot A_d T_d^4 \quad (29)$$

With σ the Stefan-Boltzmann constant, ϵ_w the emissivity of the wire material (0.2 for W3Re [27] and 0.3 for Ir [10]), ϵ_{df} the emissivity of the coating (0.5 for Y_2O_3 [28]), ϵ_{db} the emissivity of the disk material (0.325 for Ta [32] and 0.3 for Ir [10]) and T_w the temperature of the wire. The thermal emission depends strong on the temperature. To estimate the radiation power of the wire, the temperature profile was assumed to be linear resulting in:

$$P_{wire} = 2\sigma \cdot \epsilon_w \cdot 2r\pi \int_0^{l_w} \left(\frac{dT}{dl} + T_{base} \right)^4 \cdot dl \quad (30)$$

With r the wire radius and T_{Base} the temperature of the filament base. The power generated by ohmic losses P_R is:

$$P_R = RI_{heat}^2 \quad (31)$$

$$= \rho \frac{l_w}{A_w} \cdot I_{heat}^2 \quad (32)$$

With ρ the electric resistivity of the wire (0.45 $\mu\Omega$ m for W3Re [13] and 0.45 $\mu\Omega$ m for Ir [5]). The resulting power matches the values measured in the laboratory with a deviation of about 10 % which is good enough for this rough estimation. The Y_2O_3 filaments consume about 40 % less power than the standard Y_2O_3 filaments. The biggest loss in power is through thermal conductivity which makes about 70-80 % of the whole power loss for the two filament types.

2.3.2. Flight Filament Controller Boards Characterisation

In this chapter the electrical characteristics of the NIM PFM and FS controller boards used to power the electron emitting filaments in the NIM instrument is discussed.

Fig. 11 shows the electrical characteristics of the load line of a sample filament controller board (black) and a theoretical filament (blue). The intersection of the load line with the x-axis corresponds to the maximal current the filament controller board can provide and the intersection with the y-axis corresponds to the maximal voltage. Every point below the load line can be reached by the controller board. The red curves show the lines of constant power. Depending on the desired emission current, the filament disk has to be heated to a certain temperature (Eq. (24)). The higher the temperature is, the higher is the power consumption of the filament due to power losses through thermal conductivity and thermal radiation. Therefore,

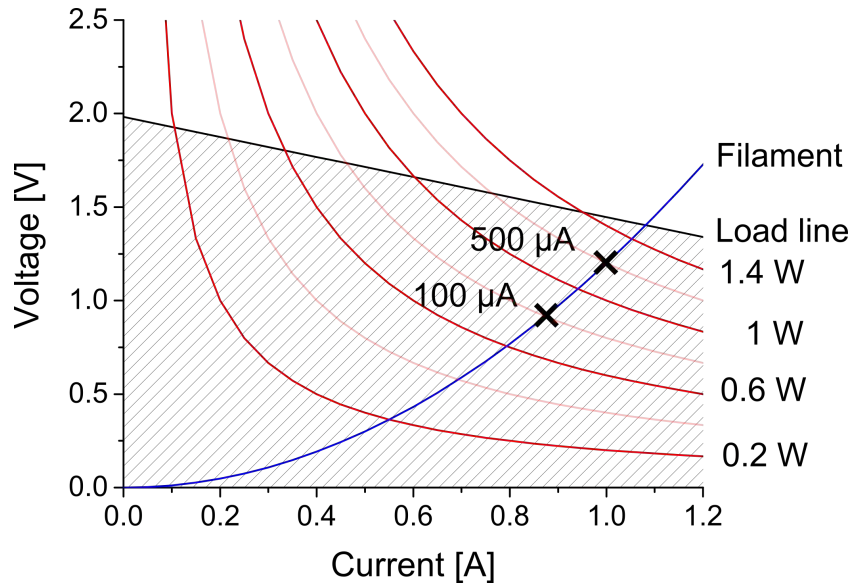


Figure 11: Electrical characteristics of a sample filament (blue) and the load line of an electronic board (black). The red lines show different power levels.

a higher emission current requires higher power. The current and voltage settings for a given emission current are the intersection of the filament line with the corresponding power line. For two emission currents, these points are marked as black crosses as an example.

Fig. 12 shows the electrical characteristics of the NIM PFM (black) and FS (grey) controller boards once for nominal supply voltage of 12.0 V and once for the minimal supply voltage of 11.4 V from the spacecraft. The blue line shows the nominal behaviour of a Y_2O_3 filament. At the current state, long term tests with filaments at different emission currents are running to verify their operation time of 10'000 h. The filaments displayed in this graphic are the once with the worst electrical characteristics from each batch. Filament 525-2343B has a target emission current of 50 μA and filament 525-2338B has a target emission current of 300 μA . For a bad filament such as 525-2338B the flight controller boards could not provide the required power. If the target emission is 50 μA the two boards can provide the power even after 2300 h of operation time. The difference in performance between the nominal filament and the filaments used in our tests originates from the different test setups in which the filaments were tested. The extraction fields in the test setup of the nominal filament were set to optimize electron emission to minimize power consumption. This is not a realistic case for a flight instrument where the extraction fields also have to focus the electron beam in the ionization region. Therefore, the test setup for the long term tests was built as a replicate of NIM's electron extraction region. The applied extraction voltages are set to nominal values used during filament operation. Therefore, the filaments are more stressed than in a setup which is optimized to extract the electrons from the filament disk [15].

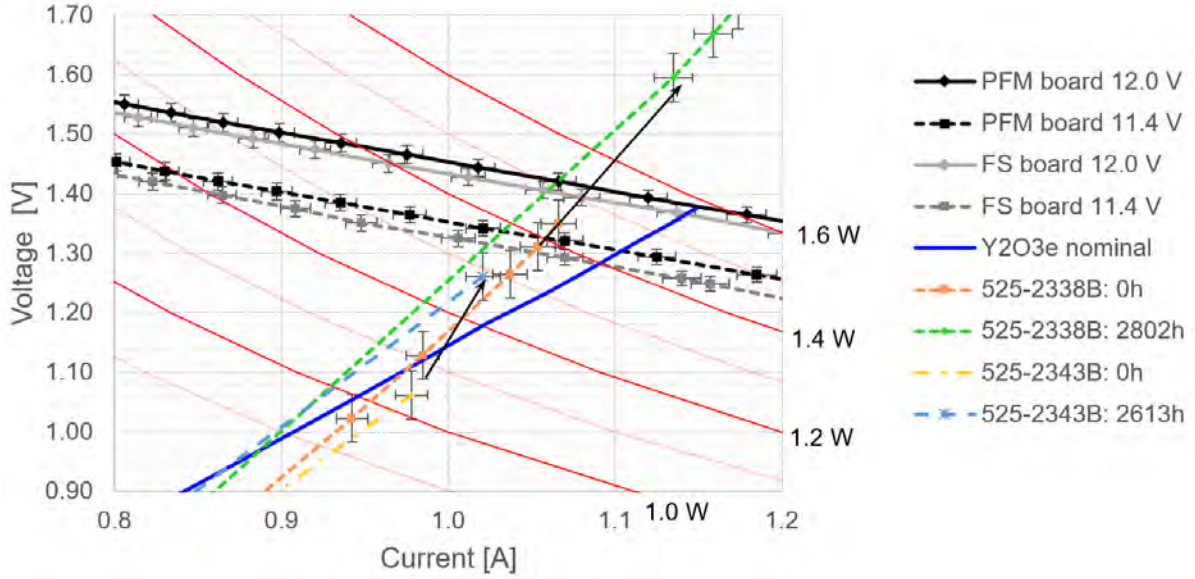


Figure 12: Electrical characteristics of selected $\text{Y}_2\text{O}_3\text{e}$ filaments and the NIM PFM and FS controller boards showing the maximal I-V capabilities of the two power supplies at nominal supply voltage of 12.0 V and reduced supply voltage of 11.4 V. The red hyperbolas in the background show the power levels (adapted from [15]).

2.4. Ion Storage **Corrections completed**

Ion storage of positive ions in the ionisation region is mainly achieved by the negative space charge potential of the electron beam. Together with the other focusing electrodes in the ionization region, a 3D trapping field is generated to store the ions during the time when no high-voltage pulse is applied on the extraction grid ($IS5$ in Fig. 13). Ion storage is important because of the duty cycle of TOF instruments with pulsed extraction, where every ion generated outside the extraction pulse is lost in case it is not stored. NIM has a nominal duty cycle of 10 kHz and the pulse duration of the extraction pulse is 1-2 μs . In the remaining 98 μs per cycle ions are produced which have to be stored in the source between two extraction pulses. Lost ions add to the random noise level. In the following section, the potential in the centre of the electron beam is calculated. The electron emission current I_e is:

$$I_e = n_e q_0 v \pi R_e^2 \quad (33)$$

With n_e the electron number density, q_0 the elementary charge, v the velocity of the electrons and R_e the radius of the electron beam (Fig. 14). The electrons get accelerated by the negative potential applied at the filament base. This potential is -70 V resulting in a kinetic energy U of 70 eV. The velocity of the electrons is:

$$v = \sqrt{\frac{2U}{m_e}} \quad (34)$$

With m_e the mass of the electron. Solving Eq. (33) for the volume density n_e and inserting Eq. (34) for the velocity results in:

$$n_e = \frac{I_e}{q_0 \pi R_e^2} \sqrt{\frac{m_e}{2U}} \quad (35)$$

The electric field $E(r)$ from the space charge of the electron beam in the ionization region is calculated for $R_e < r < h_{Is}/2$ with r the distance from the centre of the beam and h_{Is} the height of the ion source. The electric flux is defined as the surface integral of the electric field through the surface of an enclosed volume, which is in this case a cylinder volume. Using Gauss's law the electric flux through the beam surface A_{beam} is equal to the total charge Q inside the cylinder volume. In this calculation, the base and deck area are neglected:

$$A_{beam} E(r) = \frac{Q}{\epsilon_0} \quad (36)$$

$$2\pi r l E(r) = \pi R_e^2 l n_e q_0 \frac{1}{\epsilon_0} \quad (37)$$

With l the cylinder length, q_0 the elementary charge and ϵ_0 the vacuum permittivity. Replacing the number density n_e with Eq. (35) and solving the equation for the electric field $E(r)$ results in:

$$E(r) = \frac{I_e}{2\pi\epsilon_0} \sqrt{\frac{m_e}{2U}} \frac{1}{r} \quad (38)$$

The potential $\Phi_o(r)$ at a position r outside of the electron beam is:

$$\Phi_o(r) = - \int_{h_{Is}/2}^r E(r') dr' = - \frac{I_e}{2\pi\epsilon_0} \sqrt{\frac{m_e}{2U}} \ln \left(\frac{r}{h_{Is}/2} \right) \quad (39)$$

The electric field inside the electron beam at position $0 < r < R_e$ is calculated by using again Gauss's law:

$$2\pi r l E(r) = \pi r^2 l n_e q_0 \frac{1}{\epsilon_0} \quad (40)$$

Replacing the number density n_e with Eq. (35) and solving the equation for the electric field $E(r)$ results in:

$$E(r) = \frac{I_e}{2\pi\epsilon_0} \sqrt{\frac{m_e}{2U}} \frac{r}{R_e^2} \quad (41)$$

The electric potential $\Phi_i(r)$ is:

$$\Phi_i(r) = - \int_{R_e}^r E(r') dr' = - \frac{I_e}{4\pi\epsilon_0} \sqrt{\frac{m_e}{2U}} \left(\frac{r^2}{R_e^2} - 1 \right) \quad (42)$$

And relative to the border of the ion source:

$$\Phi_i(r) = - \frac{I_e}{4\pi\epsilon_0} \sqrt{\frac{m_e}{2U}} \left(2 \ln \left(\frac{R_e}{h_{Is}/2} \right) + \frac{r^2}{R_e^2} - 1 \right) \quad (43)$$

For an electron emission current of 100 μA the electric potential in the centre of the electron beam is 0.75 V. This potential is strong enough to trap species at thermal energies. For faster species, NIM has a special designed ionisation region (Fig. 13). The electrodes $IS1$, $IS5$ and $IS6$ trap the ions in x-direction where the two ring electrodes $IS2$ and $IS4$ trap the ions in the other two directions.

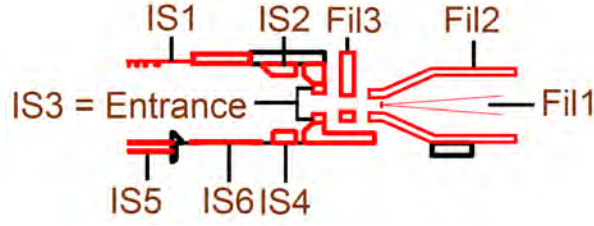


Figure 13: Detail of NIM's ionisation region.

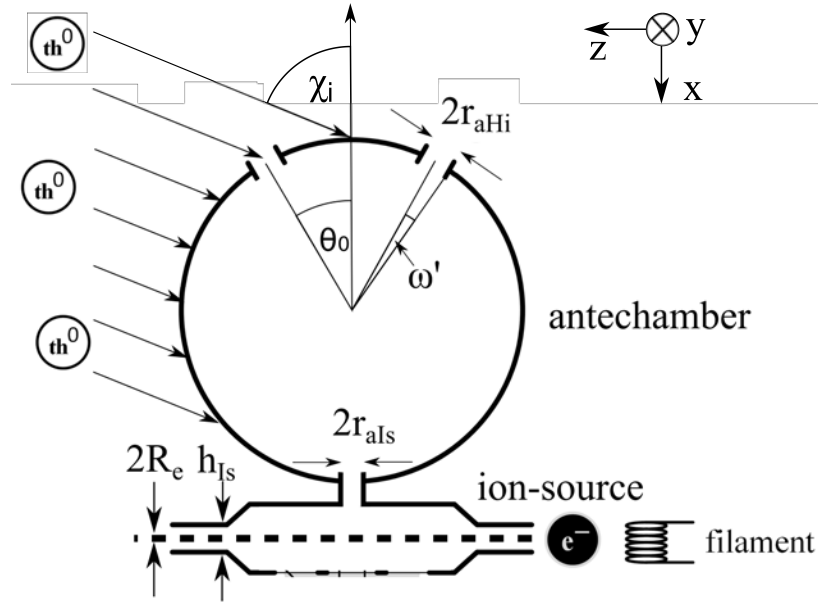


Figure 14: Schematics of the antechamber and the ionisation region.

2.5. Density enhancement of a Closed Source **finished**

NIM has an open source entrance where neutral particles and ions enter the ionisation region directly and a closed source entrance where particles enter the ionization region after being thermalized in an antechamber. In this chapter the density enhancement of the closed source entrance is determined. The density enhancement model described in [42] is used and adapted for the geometry of NIM's antechamber. The particle density n_{cs} in the ionization region is:

$$\frac{n_{cs}}{n_a} = \sqrt{\frac{T_a}{T_s}} \cdot \frac{k \cdot \sin^2\left(\frac{\omega}{2}\right) \cdot \cos^2\left(\frac{\omega}{2}\right) \left(F(S_1) + F(S_2)\right)}{1 - k \cdot \cos^2\left(\frac{\omega}{2}\right)} \cdot \frac{r_{aIs}^2 \cdot a}{2 \cdot r_{aHi}^2 + r_{aIs}^2 \cdot a} \quad (44)$$

With:

$$F(S_i) = e^{-S_i^2} + \pi^{1/2} \cdot S_i \cdot (1 + \text{erf}(S_i)) \quad (45)$$

With n_a the ambient particle density of the gas outside the instrument. For the tests in the laboratory n_a is the particle density of the neutral gas beam. In flight, the ambient particle density is the particle density of the moons atmosphere. T_a is the temperature of the ambient

gas. In the laboratory it is the temperature of the neutral particle beam. T_s is the temperature of the antechamber. k is the probability of a particle being re-emitted after colliding with the antechamber's inner surface during thermalization and is close to 1 because otherwise the particle would be absorbed. Ω is the total solid angle of all openings leading into the antechamber. NIM has two entrance holes with the same hole diameter and therefore the total solid angle Ω is the sum of the two solid angles of the entrance holes Ω' :

$$\Omega = 2 \cdot \Omega' \quad (46)$$

All openings into the antechamber have a circular shape therefore, the solid angle Ω is replaced by an angle ω in the x-z-plane to simplify the equation Eq. (44) [21]:

$$2\pi(1 - \cos(\omega)) = 2 \cdot 2\pi(1 - \cos(\omega')) \quad (47)$$

$$\cos(\omega) = 2 \cos(\omega') - 1 \quad (48)$$

$$\omega = \cos^{-1}(2 \cos(\omega') - 1) \quad (49)$$

ω' is the half angle of one entrance hole (Fig. 14). S_i in Eq. (45) is the speed ratio along the normal axis of the entrance holes:

$$S_i = \begin{cases} 0, & \cos(\chi \pm \theta_0) < 0 \\ v_{sc} \cdot \cos(\chi + \theta_0) \cdot \sqrt{\frac{m}{2k_B T_a}}, & i = 1 \\ v_{sc} \cdot \cos(\chi - \theta_0) \cdot \sqrt{\frac{m}{2k_B T_a}}, & i = 2 \end{cases} \quad (50)$$

with v_{sc} the velocity of the neutral gas beam relative to the antechamber corresponding to the spacecraft velocity, m the average particle mass of the gas and k_B the Boltzmann constant. χ is the angle of the test gas relative to the x-axis of the instrument and θ_0 is the angle between the x-axis and the axis normal of the entrance hole. $\chi \pm \theta_0$ is the angle between the normal axis of the entrance hole and the gas inflow direction. $\chi \pm \theta_0$ has to be between $\pm 90^\circ$ to enter the antechamber which implies that $\cos(\chi \pm \theta_0)$ cannot have negative values. $i = 1$ is the index of one of the two entrance holes and $i = 2$ is the index of the other entrance hole. The antechamber has three openings for the gas to flow out of the antechamber. The last term in Eq. (44) gives the ratio of how many particles leave the antechamber through the hole connecting the antechamber with the ionization region compared to the amount of particles leaving the antechamber through the two entrance holes. The radius of the entrance holes is r_{aHi} and the radius of the hole connecting the antechamber with the ionization region is r_{aIs} . This term takes the molecular flow conductance of the different holes into account. The molecular flow conductance of a thermalized gas is:

$$C_0 = A\bar{v}/4 \quad (51)$$

with A the cross-section of the opening and \bar{v} the average velocity of the thermalized gas flowing through that opening. This formula is only valid in case the length of the tube is close to zero. Otherwise, the transmission probability a has to be added resulting in:

$$C = C_0 \cdot a \quad (52)$$

The transmission probability depends on the length-to-radius ratio L/R of the opening. van Essen and Heerens [37] compared different models to determine the transmission probability and calculated the values for specific length-to-radius ratios. The model which comes closest to reality is the one by Nawyn and Meyer (published by [37]). To calculate the transmission probability for any length-to-radius ratio, the data resulting from Nawyn and Meyer's model were fitted with the following function:

$$a = y_0 + y_1 \left(1 - e^{-\frac{L/R}{t_1}}\right) + y_2 \left(1 - e^{-\frac{L/R}{t_2}}\right) \quad (53)$$

y_0	0.998 ± 0.001	t_1	7.4 ± 0.3
y_1	-0.48 ± 0.01	t_2	1.13 ± 0.04
y_2	-0.45 ± 0.01		

Table 1: Fit parameters of Eq. (53).

The fit parameters are listed in Table 1. For the two gas entrance openings of the antechamber a is 1 because they have a sharp edge and therefore the length of the opening is close to zero. The opening between the antechamber and the entrance has a length-to-diameter ratio of 8 resulting in a $a = 0.23$. The amount of gas flowing through this opening relative to the total outflow is:

$$G_{open} = \frac{C_{aIs}}{C_{aIs} + 2 \cdot C_{aHi}} \quad (54)$$

$$G_{open} = \frac{\frac{r_{aIs}^2 \cdot a \cdot \bar{v}}{4}}{\frac{r_{aIs}^2 \cdot a \cdot \bar{v}}{4} + 2 \frac{r_{aHi}^2 \cdot \bar{v}}{4}} \quad (55)$$

$$G_{open} = \frac{r_{aIs}^2 \cdot a}{r_{aIs}^2 \cdot a + 2 \cdot r_{aHi}^2} \quad (56)$$

With $r_{aIs} = 2$ mm and $r_{aHi} = 2.5$ mm resulting in $G_{open} = 0.067$ meaning that about 6.7% of all particles entering the antechamber actually reach the ionization region due to losses of the geometry.

In the following section the different parameters of the density enhancement equation Eq. (44) were varied to determine their impact. For this analysis the particle density in the ionization region n_{cs} was divided by the particle density of the test gas n_a outside of the antechamber and n_a was set 1 to get the amplification of the antechamber. For this analysis the parameters were set according to Table 2 unless otherwise mentioned. The temperatures are the ones used in the laboratory. The used particle velocity was 2.5 km/s because it is the velocity of the spacecraft in Ganymede orbit and therefore the velocity at which most of the measurements

T_a	295 K	r_{aHi}	2.5 mm	χ	0°
T_s	320 K	r_{aIs}	2 mm	θ_0	30°
k	1	v_{sc}	2.5 km/s	m	18 u
a	0.23				

Table 2: Values used for the variation of the different variables of the amplification factor of the antechamber (Eq. (44)).

will be done. The particle reflection coefficient k of the inner coating of the antechamber was set 1 assuming an ideal coating reflecting all particles. The transmission probability a of the hole connecting the antechamber with the ionization region, the radius of the antechamber entrance holes r_{aHi} , the radius of the hole connecting the antechamber with the ionization region r_{aIs} and the angular position of the entrance holes θ_0 are defined by the geometry of the antechamber. χ was set to 0° . The main gas inflow direction lies then between the two entrance holes. The used test gas was water with a unit mass of 18 u.

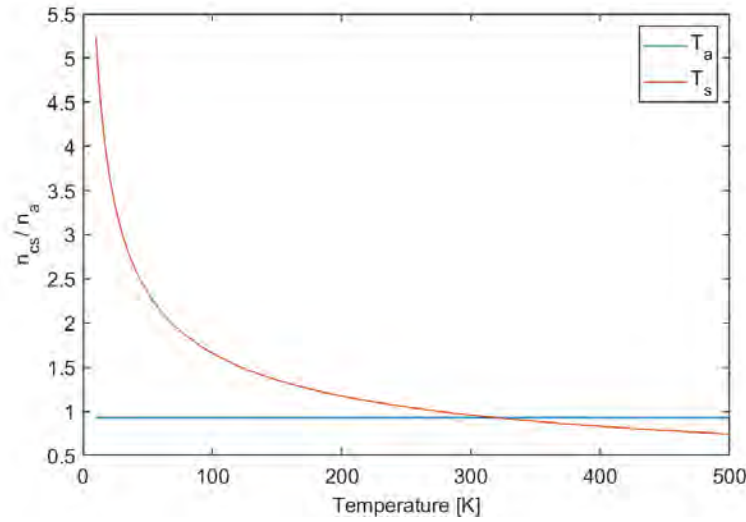


Figure 15: Density enhancement n_{cs}/n_a of the antechamber as a function of the ambient gas temperature T_a and the temperature of the antechamber wall T_s according to Eq.(44).

The first parameter that was varied was the gas temperature T_a . This temperature can be varied between 0 and 1000 K without significantly influencing the density enhancement of the antechamber (Fig. 15). When looking closer, a slight increase in density enhancement is observed with increasing temperature.

The temperature of the antechamber T_s has a bigger impact on the density enhancement. Ideally this temperature should be as low as possible to slow down the particles when they

hit the chamber inner walls (see also Eq. (44)). When the temperature of the antechamber is too low, the gas condenses at the antechamber walls. Therefore, the particle reflection coefficient of the k will decrease with decreasing temperature depending on the particle species. For this calculation, this effect was not taken into account. In flight, the antechamber is kept at temperatures higher than -17°C during measurements to avoid condensation on the antechamber walls.

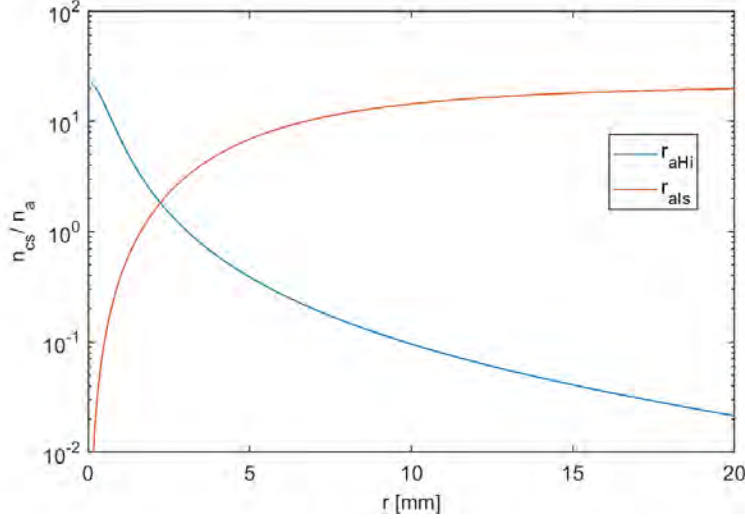


Figure 16: Density enhancement n_{cs}/n_a of the antechamber as a function of the entrance hole radius r_{aHi} and the radius connecting the antechamber with the ionisation region r_{aIs} .

The radius r_{aIs} of the hole connecting the antechamber with the ionisation region has to be as big as possible. A bigger radius leads to a smaller length-to-diameter ratio resulting in a bigger transition probability a . The amount of gas flowing into the ionisation region increases (Fig. 16). The radius of the entrance holes r_{Hi} should be as small as possible to increase the number of collisions of the neutral particles with the antechamber walls to thermalise them. In addition, when the entrance holes are big, a big amount of gas flows out through them. From that perspective, the biggest gain is achieved when the radius of the entrance hole is close to zero. Eq. (44) does not take into account that at a certain opening radius is needed to allow particles to enter the antechamber for being amplified. The equation is only valid for small openings to guaranty enough collisions of the gas with the chamber walls. Therefore, the requirement was that the area of all openings of the antechamber has to be 10% of the total sphere surface.

It is very important to take materials with a high particle reflection coefficient k for the coating of the antechamber's inner surface. The particle reflection coefficient gives the probability of a particle being re-emitted when hitting the surface thus this value has to be close to 1. NIM has a gold coated antechamber because gold is electrically conductive preventing the surface from charging in the strong radiation field of Jupiter. In addition, gold is chemically inert and

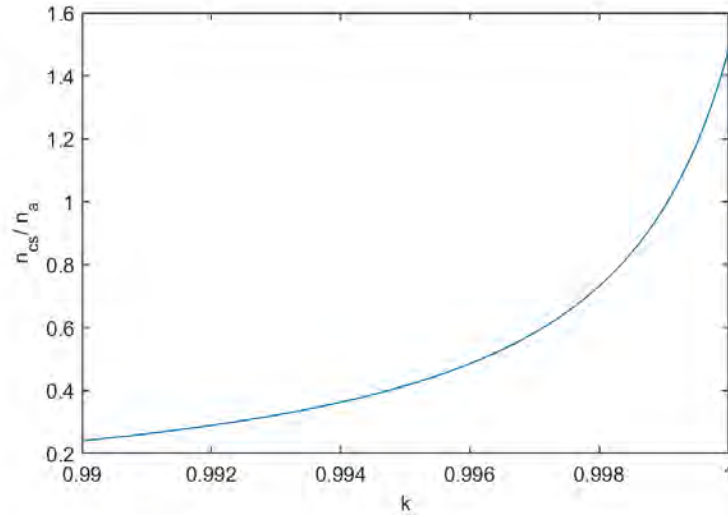


Figure 17: Density enhancement n_{cs}/n_a of the antechamber as a function of the particle reflection coefficient k .

therefore, there is a low probability of building chemical bonds with the test gas. Fig. 17 shows the density enhancement of the antechamber as a function of k . Already a change of 1‰ has a huge impact. The impact of k also depends on ω . A small ω implies a big surface area with which the particles interact before being detected. The bigger the number of interactions is, the bigger is the influence of k . The ω of NIM's antechamber is about 5.06° , which is very small and therefore a small change in k has a big impact on the density enhancement.

Fig. 18 shows the density enhancement of the antechamber as a function of the particles unit

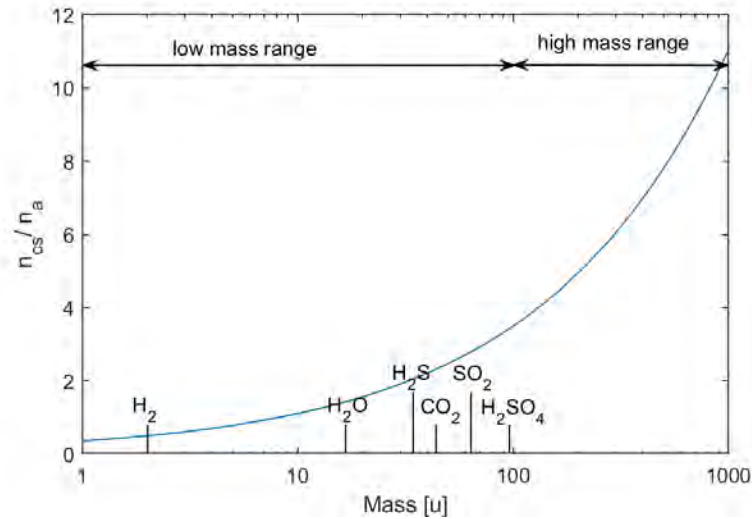


Figure 18: Density enhancement n_{cs}/n_a of the antechamber as a function of the particle mass m .

mass [u]. The figure shows that higher mass species have a higher density enhancement factor than low mass species. Since the higher mass species are usually of low abundance in the icy moons exospheres [39, 38], this mass dependence of the density enhancement factor is very helpful.

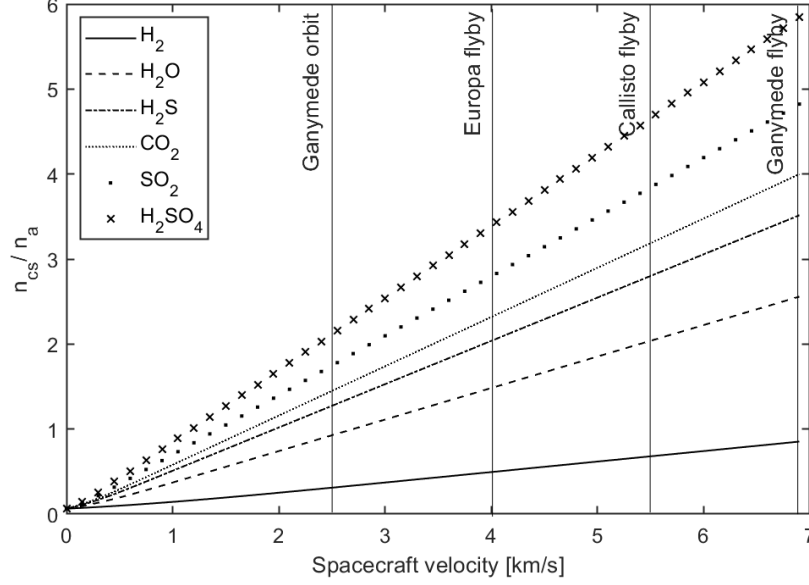


Figure 19: Density enhancement n_{cs}/n_a of the antechamber as a function of the spacecraft velocity v_{sc} for different species expected in the icy moons exospheres.

Fig. 19 shows the density enhancement of the antechamber as a function of the spacecraft velocity for different species. We expect H_2O and different radiolysis products such as H_2 , O_2 or HO in the icy moons' exosphere. Absorption lines in the near infrared recorded by the Near Infrared Mapping Spectrometer (NIMS) on board of the Galileo spacecraft indicate CO_2 bond to other solid materials in the soil. Sulphur is ejected by the Galilean moon Io and is therefore part of the Jupiter's plasma torus. The sulphur compounds are a result of the ion bombardment on the icy moons' surface. Sulphur reacts with water resulting in various different compounds such as sulphur dioxide (SO_2) or sulphuric acid (H_2SO_4) [12]. Fig. 19 shows that with increasing flyby velocity, the particles get more amplified. Heavier species are stronger amplified than light ones as it was already shown in Fig. 18.

Fig. 20 shows the density enhancement of the antechamber as a function of different particle influx angles χ . χ is measured in the x-/y- plane of NIM's coordinate system (see Fig. 14). The function was evaluated for different positions of the entrance holes. The minimal angle the two entrance holes can be apart from each other without overlapping is 3.6° . The holes of the PFM antechamber are at $\theta_0 = \pm 30^\circ$. With that configuration the biggest signal intensity is measured with a spacecraft ramp direction of 0° . When the two holes are at $\pm 60^\circ$ the intensity distribution has a plateau between $\pm 60^\circ$ and also a wider angular range. This is an interesting feature under certain circumstance. For NIM it is unnecessary because the spacecraft blocs the field of view (FoV) for angles bigger than 100° (see also Chap. 2.6).

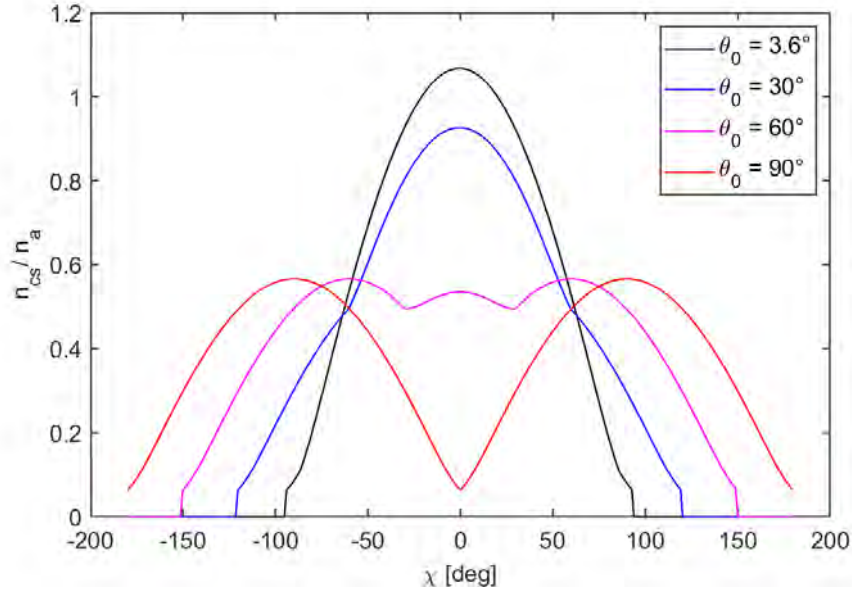


Figure 20: Density enhancement n_{cs}/n_a of the antechamber as a function of the angle χ between the gas inflow direction and the x-axis of the instrument for different positions of the two entrance holes θ_0 . $\theta_0 = 30^\circ$ is the position of the holes in flight configuration.

2.6. Field-of-View Analysis **finished**

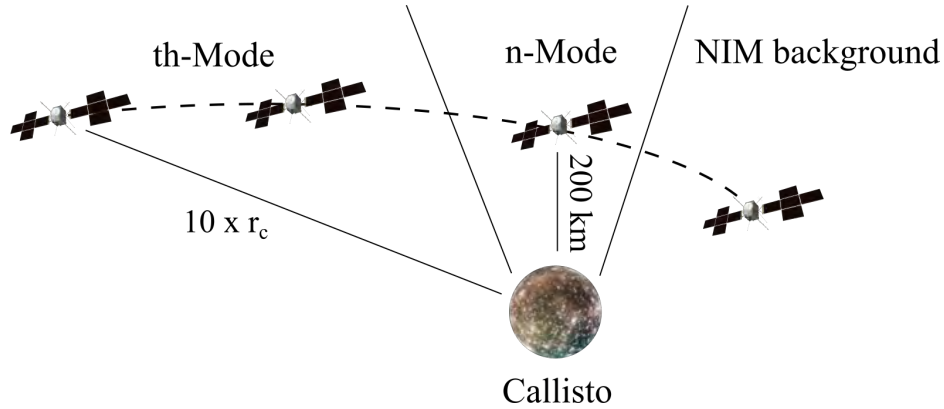


Figure 21: Schematics of a flyby at Jupiter's moon Callisto.

In the following section, the fourth Callisto flyby of JUICE according to the Consolidated Report on Mission Analysis (CReMA) version 3.2 trajectory 141a [9] is analysed as an example of the expected particle flux directions during a flyby. Fig. 22 – Fig. 27 show the changing FoV of the NIM instrument at different times. The reference coordinate system for these graphics is the ecliptic coordinate system. During the flyby, the spacecraft changes its orientation leading to a different appearance of the objects in the figures. The centres of the entrance holes of

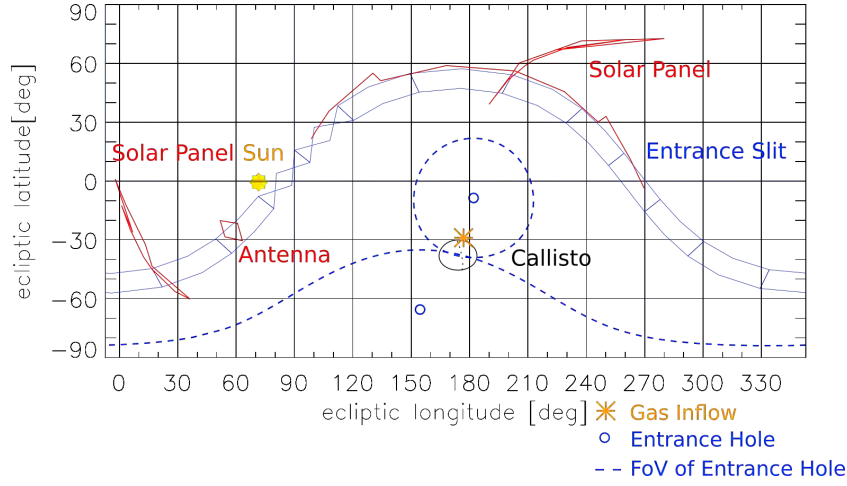


Figure 22: Fourth Callisto flyby of CReMA 3.2 trajectory 141a [9] 1 h before closest approach 15'600 km above Callisto's surface.

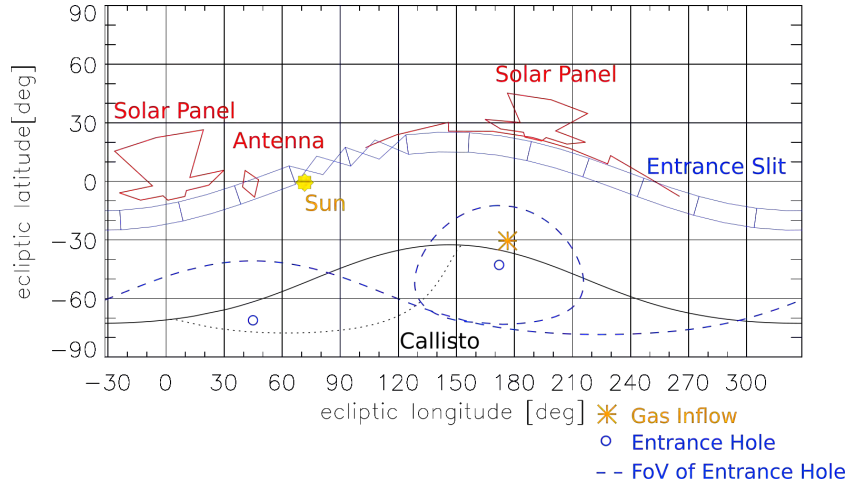


Figure 23: Fourth Callisto flyby of CReMA 3.2 trajectory 141a [9] 10 min. before closest approach 1'560 km above Callisto's surface.

the antechamber are marked as blue circles, the FoVs of the entrance holes of the antechamber are marked as dashed blue lines (actually, the 30° radius line of the FoV), the entrance slit at the open source entrance is the blue, striped band with the sinusoidal shape. The solar panels and the rim antenna of the spacecraft are marked in red. The gas inflow direction is marked as an orange asterisk. Fig. 22 shows the FoV 1 h before closest approach 15'600 km above Callisto's surface. The gas inflow direction is in between the two entrance holes thus both holes collect gas from Callisto's exosphere. As the spacecraft moves closer to the moon, the gas inflow direction moves towards the entrance slit. 5 min. before closest approach, NIM changes from thermal to neutral mode because of the narrow FoV of 10° of the entrance slit and the short time window during which the gas inflow direction is within the FoV of the entrance slit (Fig. 24). At this time, the gas inflow direction is still in the FoV of the antechamber. The

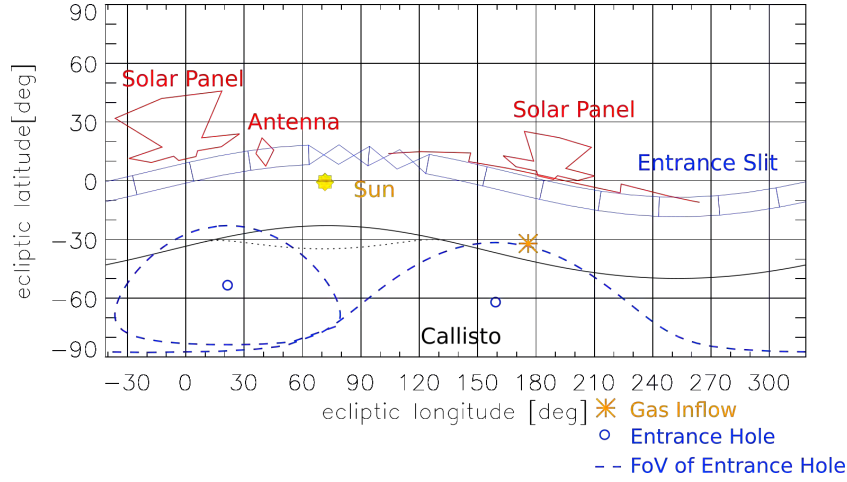


Figure 24: Fourth Callisto flyby of CReMA 3.2 trajectory 141a [9] 5 min. before closest approach 580 km above Callisto's surface.

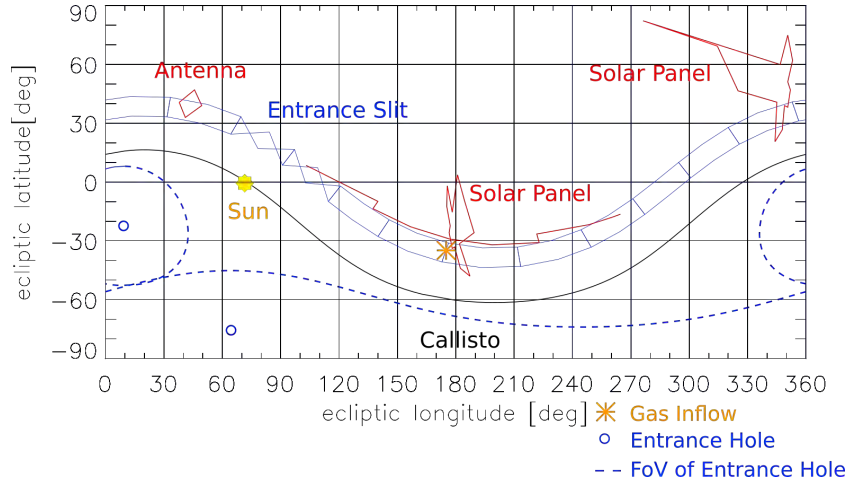


Figure 25: Fourth Callisto flyby of CReMA 3.2 trajectory 141a [9] closest approach 200 km above Callisto's surface with the spacecraft solar panels oriented toward the Sun to maximize power generation.

design goal for the switch over between the two modes is 1 s to minimize the number of lost measurements. These measurements are very crucial because the closer the spacecraft gets to the moon's surface, the higher is the exospheric density and therefore the signal intensity (see Fig. 30). 5 min. after closest approach, the gas inflow direction is below the FoV of the neutral gas channel and NIM takes background measurements (Fig. 27). In addition, the spacecraft structure obstructs angles higher than 105° either by the platform on which NIM is mounted or by the solar panels [36]. Fig. 28) shows the JUICE spacecraft with the solar panels in straight up position where they limit NIM's FoV to 75° in the direction along the solar panels. When the solar panels are tilted by 90° , they obstruct NIM's FoV for angles bigger than 100° which is configuration of the closest approach when NIM is measuring with the neutral gas channel. When gas strikes the spacecraft it sputters particles from the spacecraft's surface. NIM is

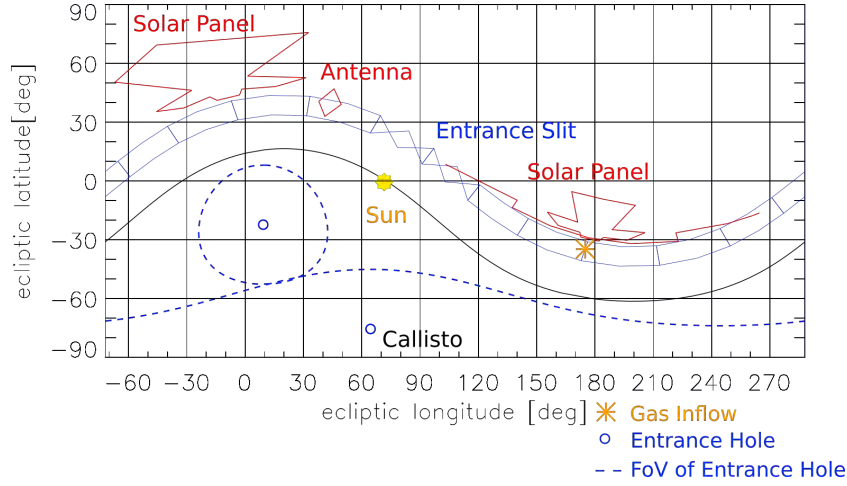


Figure 26: Fourth Callisto flyby of CReMA 3.2 trajectory 141a [9] closest approach 200 km above Callisto's surface with solar panels tilted to leave unobstructed NIM's field-of-view of the n-Mode.

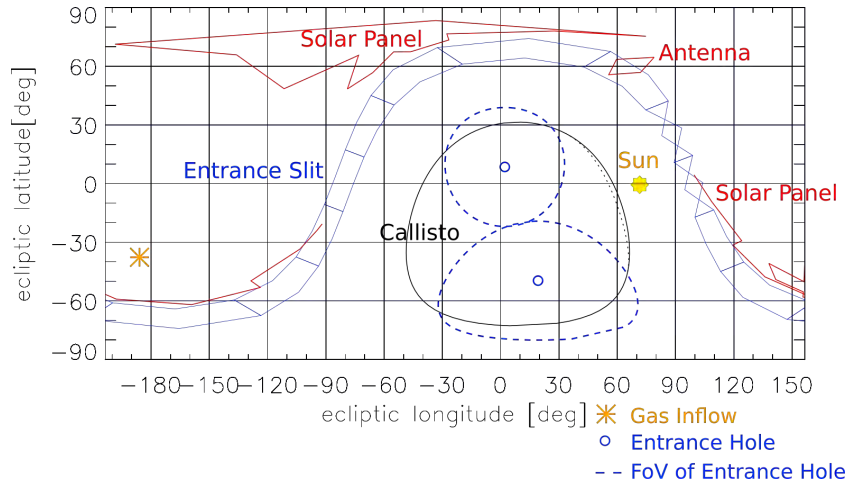


Figure 27: Fourth Callisto flyby of CReMA 3.2 trajectory 141a [9] 5 min. after closest approach 640 km above Callisto's surface.

not able to determine if these particles are part of the moons exosphere or if they originate from the spacecraft. In general, the solar panels are adjusted perpendicular to the Sun where possible to maximize power generation. 10 min. before closest approach, the solar panels are tilted to leave the FoV of NIM unobstructed to measure with the neutral gas mode. In case the solar panels would stay perpendicular to the Sun, the gas would graze the surface of the solar panel as it is shown in Fig. 25. Fig. 26 shows the same scenario but with the solar panels tilted to leave NIM's FoV unobstructed for the neutral gas channel.

Fig. 29 shows the density enhancement of the antechamber with the total FoV of the two entrance holes marked as red area $\pm 30^\circ$ around the position of the two entrance holes. The orange asterisks mark the gas inflow direction for the various scenarios mentioned above. De-

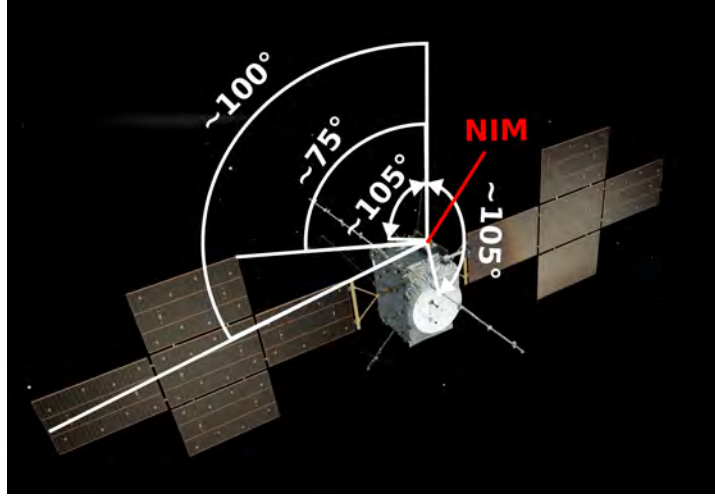


Figure 28: NIM field-of-View on the JUICE spacecraft.

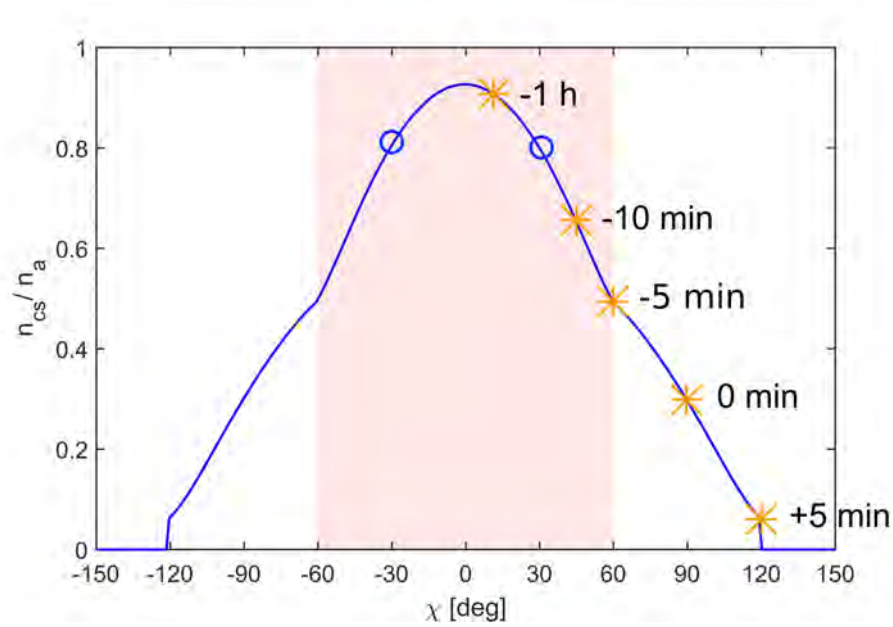


Figure 29: Density enhancement n_{cs}/n_a of the antechamber as a function of the angle χ between the gas inflow direction and the x-axis of the instrument for different positions of the two entrance holes θ_0 . The blue circles mark the entrance hole positions and the red area marks the FoV. The asterisks mark the gas influx direction from 1 h before until 5 min after closest approach of CReMA 3.2 trajectory 141a [9].

pending on the flyby, the main gas inflow direction is from the $+\chi$ or $-\chi$ side. Therefore, it was decided to make two entrance holes in the antechamber to allow measurements with angles different to the main direction to enlarge the FoV of the antechamber. The holes should also not be too close at the entrance because structures of the spacecraft bloc angles bigger

than 105° and the density enhancement at at such big angles would be useless.

Fig. 30 shows simulated density profiles of Callisto's exosphere. In this model, the particles

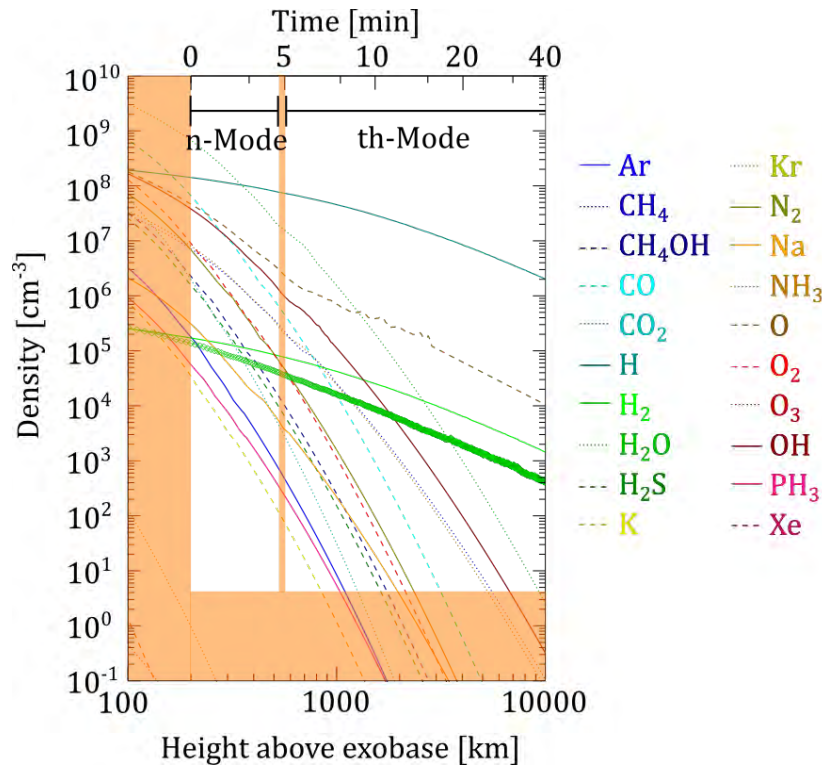


Figure 30: Gas density profiles of Callisto's exosphere simulated by Vorburger et al. [39]. Orange areas mark regions NIM is not able to detect either because the JUICE spacecraft does not fly closer to the moon's surface or because NIM's sees only particle densities higher than 4 cm^{-3} .

have been sublimated from Callisto's ice surface at the sub-solar point [39]. The x-axis at the bottom shows the height above the exobase and the x-axis at the top shows the time before closest approach of the spacecraft. The orange areas are density distributions NIM is not able to detect. For the flyby discussed above, the closest approach of the spacecraft is at 200 km above Callisto's surface. The detection limit of NIM in Jupiter's strong radiation environment is 4 cm^{-3} for an integration time of 5 sec [26]. 5 min before closest approach, NIM changes from thermal to neural mode indicated with the small orange bar at position 5 min. During the mode change, NIM cannot record any spectra. The longer the switch over takes, the bigger is therefore this area where precious spectra get lost.

NIM has different measuring modes with regards to the recording configuration of the spectra. One of these configuration parameters is the integration time. The integration time is the time during which the instrument sums up all recorded single spectra. With a pulse frequency of 10 kHz, a spectrum with an integration time of 5 sec consists of 50'000 summed up single spectra. The SNR increases with the square root of the integration time because when more single spectra are summed up, the random noise cancels out and the gas peaks remain because they appear always at the same position in the spectrum. Therefore, a longer integration time

improves the SNR and the amount of acquired data per time is smaller which is an advantage because JUICE can only transmit a certain amount of data per day back to earth. A longer integration time also implies a worse spacial resolution of the density profile along the flight path of the spacecraft because the sampling rate is lower.

For a flyby, 12 h before closest approach at the moons, NIM will start with a bake out and warm up of the system to get the system in a stable thermal state. The bake out is necessary to get rid of condensed particles at the instrument. Otherwise, these particles are released during operation of the instrument and are then visible in the recorded mass spectra. These particles cannot be distinguished from particles originating from the moons' exospheres. The integration time can be set to 1, 5, 10, 100 or 300 seconds. When the spacecraft is far away from the moon (11 h before closest approach), the integration time is set to 300 sec because at these far distances the neutral particle density and therefore a longer integration time is favourable because it corresponds to a higher SNR. In addition, spacial resolution is of minor importance at these distances. When JUICE gets closer to the moon, the integration time is decreased because the neutral particle number density increases and to get a better picture from the spacial distribution of gas composition in the icy moons' exosphere. At closest approach for the flybys at Ganymede and Callisto, the integration time is about 5 sec. To reduce the amount of produced data, NIM records most of the time spectra with a reduced mass range which records masses between 0-300 u. For the two Europa flybys, the recorded mass range will be 0-1000 u because there the main focus lies on the detection of potential organic compounds. As a trade-off the minimal integration time will be set to 10 sec instead of 5 sec as for the flybys at Ganymede and Callisto. This on one hand results in an increased sensitivity but on the other hand, the spacial resolution is then worse for these flyby. The Galileo spacecraft recorded plumes of water vapour on Europa. JUICE would like to fly through one these plumes and therefore, NIM has a special plume mode where the integration time is only 1 sec to get a good spacial resolution of the plume.

2.7. Shutter Performance **finished**

With the open-source entrance, NIM is able to measure neutral particles and ions directly without any interaction with the structure. Since the n-mode and the th-mode use the same ion-source, NIM has a shutter to close the entrance to the antechamber. This shutter is mounted between the ionisation region and the antechamber (Fig. 31 left). When the shutter is open, the gas flows from the antechamber right through the hole into the ionisation region. When the shutter is closed, the hole in the shutter moves to the side as it is indicated in Fig. 31 right panel. The shutter does not close the hole perfectly and therefore a small amount of gas flows through the gap around the shutter into the ionisation region. In the following section, the molecular flow conductance of the closed shutter is determined.

The molecular flow conductance C is:

$$C = \frac{A \cdot \bar{v} \cdot a}{4} \quad (57)$$

With A the cross-section of the tube connecting the antechamber and the ionisation region, \bar{v} the average velocity of the thermalised gas flowing through the opening and a the transmission

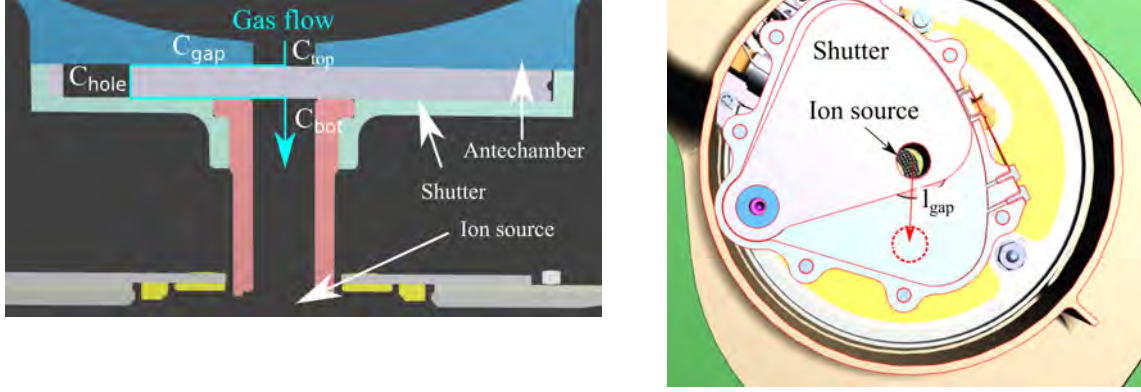


Figure 31: Left: side view when shutter is closed. Right: Top view with open shutter. When the shutter is closing, the central hole of the shutter blade moves to the red position.

probability depending on the length-to-diameter ratio of the tube (Eq. (53)). When the shutter is closed, the conductance of the tube C_{tot} is divided into four terms: The conductance of the upper part of the tube C_{top} , the conductance of the gap between the shutter blade and the pocket C_{gap} , the conductance of the hole in the shutter C_{hole} and the conductance of the lower part of the tube connecting the antechamber with the ionisation region C_{bot} (Fig. 31 left):

$$C_{top} = \frac{r_{aIs}^2 \cdot \pi \cdot \bar{v} \cdot a_{top}}{4} \quad (58)$$

$$C_{gap} = \frac{2 \cdot r_{aIs} \cdot \pi \cdot h_{gap} \cdot \bar{v} \cdot a_{gap}}{4} \quad (59)$$

$$C_{hole} = \frac{r_{aIs}^2 \cdot \pi \cdot \bar{v} \cdot a_{hole}}{4} \quad (60)$$

$$C_{bot} = \frac{r_{aIs}^2 \cdot \pi \cdot \bar{v} \cdot a_{bot}}{4} \quad (61)$$

a_{top}	0.73	h_{top}	1.5 mm
a_{gap}	0.07	h_{gap}	0.01 mm
a_{hole}	0.67	h_{hole}	2 mm
a_{bot}	0.28	h_{bot}	12 mm
r_{aIs}	2 mm	l_{gap}	7 mm

Table 3: Nominal transmission probabilities a , tube heights h , tube radius r_{aIs} and minimal gap length l_{gap} when the shutter between the antechamber and the ionisation region is closed.

With a_{top} , a_{gap} , a_{hole} and a_{bot} the transmission probabilities of the different sections (Eq. (53)) and h_{top} , h_{gap} , h_{hole} and h_{bot} the height of the different sections. r_{aIs} is the radius of the tube connecting the antechamber with the ionisation region and l_{gap} is the minimal distance between the hole in the shutter and the tube connecting the antechamber with the ionisation region. The nominal values for these parameters are listed in Table 3. The average velocity \bar{v} cancels out during the derivation of the geometry factor. The molecular flow conductance of the tube when the shutter is closed C_{tot} is:

$$\frac{1}{C_{tot}} = \frac{1}{C_{top}} + \frac{2}{C_{gap}} + \frac{1}{C_{hole}} + \frac{1}{C_{bot}} \quad (62)$$

The conductance of one of the entrance holes of the antechamber is:

$$C_{aHi} = \frac{r_{aHi}^2 \cdot \pi \cdot \bar{v}}{4} \quad (63)$$

The geometry factor of the tube when the shutter is closed G_{close} is:

$$G_{close} = \frac{C_{tot}}{C_{tot} + 2 \cdot C_{aHi}} \quad (64)$$

The geometry factor for the tube when the shutter is open was calculated with Eq. (56). Fig. 32 shows the damping factor G_{open}/G_{close} as a function of the gap size h_{gap} of the gap between the shutter and antechamber. With increasing gap size, the damping factor reduces significantly. The theoretical requirement was to damp the signal from the antechamber by a factor 1000 when the shutter is closed. A realistic gap size from the mechanical point of view is 0.01 mm resulting in a damping factor of 600 (optimal design), which is close enough to the requirement. The damping factor of the NIM PFM is only 25 implying a gap size of 0.1 mm (see Chap. 4.5). This can happen when the shutter is not properly fabricated and the tolerances are therefore bigger than originally designed.

When measuring with the open source channel, a small amount of gas will enter in addition the ionisation region through the antechamber. The open source slit is in the y-/z-plane and therefore χ is 90° (Fig. 14). When the shutter is closed, about 0.05 % of the signal originates from the antechamber, assuming a damping factor of 600. With a damping factor of only 25, 1.1 % of the measured signal originates from the antechamber.

2.8. Multichannel Plates **finished**

To count single ions, NIM uses Multichannel Plates (MCPs) in its detector to amplify the signal. MCPs are thin glass plates consisting of many small channels. When an ion hits a channel, an electron is ejected and accelerated along the channel axis until it hits the opposite wall. There it ejects more electrons generating an electron avalanche. One single MCP is able to amplify the signal of an ion by a factor of 10^4 [41]. NIM has two MCPs in Chevron configuration (Fig. 33) to reach a gain of about 10^6 (Chap. 4.7).

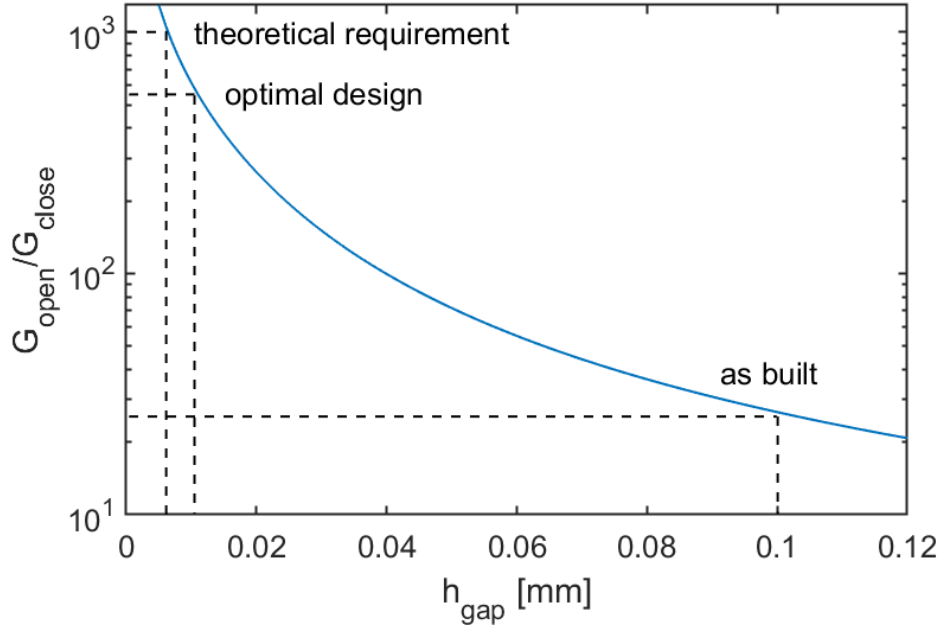


Figure 32: Damping factor G_{open}/G_{close} of the shutter as a function of the gap size h_{gap} of the gap between the shutter and antechamber.

2.8.1. Gain

In this section, the gain of a single MCP is derived as a function of the voltage U_{MCP} applied over the MCP. The derivation is based on the lecture notes of [43]. When an incoming particle hits the MCP channel wall there is a certain probability that it ejects an electron. By applying an electric field E over the MCP plate, this electron gets accelerated along the channel axis until it hits the opposite wall, where it ejects more electrons (Fig. 33):

$$E = \frac{U_{MCP}}{l} = \frac{F}{q_0} = \frac{am_e}{q_0} \quad (65)$$

With U_{MCP} the voltage applied over the MCP, l the channel length, F the force applied on the electron, q_0 the elementary charge and m_e the mass of the electron. The acceleration a of the electron is:

$$a = \frac{U_{MCP} \cdot q_0}{l \cdot m_e} \quad (66)$$

The distance s the electron travels along the channel until it reaches the channel wall is:

$$s = \frac{1}{2}at^2 = \frac{U_{MCP} \cdot q_0 \cdot t^2}{l \cdot m_e \cdot 2} \quad (67)$$

With t the flight time of the electron until it hits the wall again. Assuming the initial velocity v_{init} of the initial secondary electron is perpendicular to the channel wall, the flight distance until it hits the opposite channel wall is the channel diameter d . The flight time t can be written

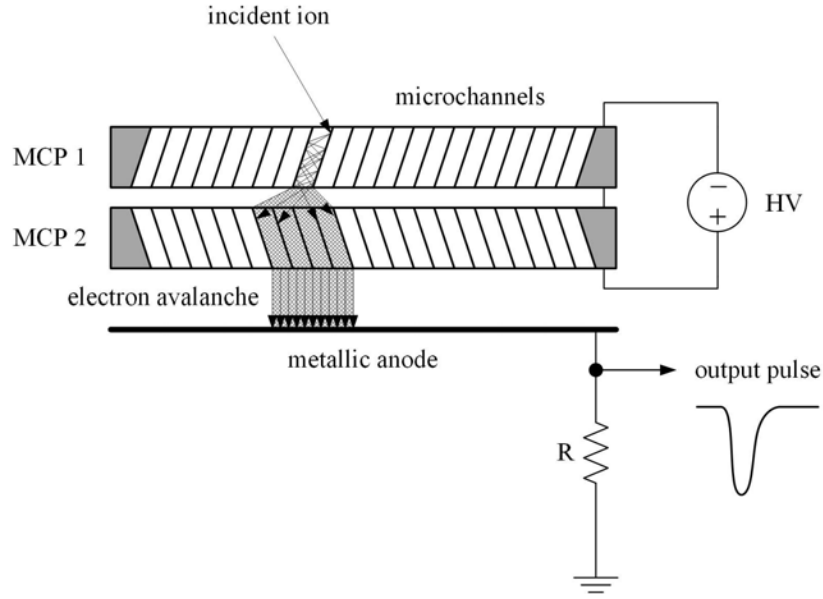


Figure 33: Working principle of a Multichannel Plates (MCPs) detector [41, 30].

as:

$$t = \frac{d}{v_{init}} \quad (68)$$

v_{init} is derived from the electron's initial kinetic energy U_{init} :

$$U_{init} = \frac{1}{2} m_e v_{init}^2 \rightarrow v_{init} = \sqrt{\frac{2U_{init}}{m_e}} \quad (69)$$

where U_{init} is the mean energy of a released electron (secondary electron) upon electron impact on the surface. By inserting Eq.(68) and Eq.(69) in Eq.(67) leads to:

$$s = \frac{q_0 \cdot U_{MCP} \cdot d^2}{l \cdot 4U_{init}} \quad (70)$$

The energy U_c the electron gains during the flight time t is:

$$U_c = q_0 E s = q_0 \cdot \frac{U_{MCP}}{l} \cdot \frac{q_0 \cdot U_{MCP} \cdot d^2}{l \cdot 4U_{init}} \quad (71)$$

$$= q_0^2 \frac{U_{MCP}^2 \cdot d^2}{l^2 \cdot 4U_{init}} \quad (72)$$

The secondary electron emission coefficient δ is proportional to the square root of the energy U_c :

$$\delta = A \cdot \sqrt{U_c} = A \cdot \frac{q_0 U_{MCP} \cdot d}{2\sqrt{U_{init}} \cdot l} \quad (73)$$

With A a fit constant. After n collisions, the gain G_{ch} of one channel is:

$$G_{ch} = \delta^n = \delta^{l/s} \quad (74)$$

The number of collisions is the channel length l divided by the distance s an electron flies within the channel before it hits the channel wall and ejects more electrons. Inserting now Eq.(73) and Eq.(70) in Eq.(74) leads to:

$$G_{ch} = \left(A \cdot \frac{q_0 U_{MCP} \cdot d}{2\sqrt{U_{init}} \cdot l} \right)^{\frac{4U_{init}}{q_0 U_{MCP}} \left(\frac{l}{d} \right)^2} \quad (75)$$

By writing the channel length to diameter ratio $\frac{l}{d}$ as α and expressing the electrons initial energy U_{init} in [eV], the equation turns into:

$$G_{ch} = \left(A \frac{U_{MCP}}{2\alpha\sqrt{U_{init}}} \right)^{\frac{4 \cdot U_{init} \cdot \alpha^2}{U_{MCP}}} \quad (76)$$

With A approximately $0.2 \left(\frac{1}{\text{eV}} \right)^{1/2}$ [41], U_{MCP} in [eV], α is a dimensionless number and U_{init} in the range of a few [eV].

2.8.2. Dead time

In this chapter, the dead time τ of the MCPs used in the NIM detector is derived. The dead time is the time one single channel of the MCP needs to replenish 63% of its charge. After 5τ the channel is fully recharged. When the ion count rate is too high, an ion will hit the channel during the time the channel is recharging. This results in a lower gain because the channel is not fully charged during the time of the event. Therefore, it is important to know the dead time to get an estimation of the upper limit of the count rate of the detector.

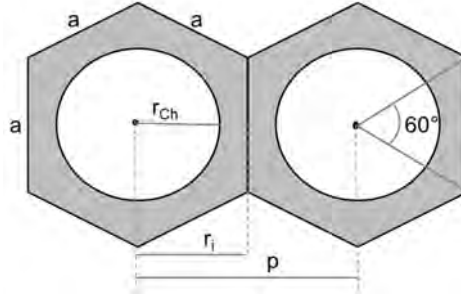


Figure 34: MCP honeycomb structure [33].

The number of channels N of an MCP is its active area A_{act} divided by the area of one channel A_{hex} . The MCP has a honeycomb like structure (Fig. 34). Thus, the area of one channel is the area of a hexagon:

$$N = \frac{A_{act}}{A_{hex}} = \frac{2 \cdot \pi r_{act}^2}{\sqrt{3} p^2} \quad (77)$$

r_{act} is the radius of the active area of the MCP, which is for the NIM MCPs 8 mm and p is the distance between the centres of two channels which is 6 μm . This results in $1.6 \cdot 10^6$ channels of a NIM MCP. The resistance of a single channel is the resistance of the whole MCP plate R_{MCP} times the number of channels N :

$$R_{ch} = R_{MCP} \cdot N \quad (78)$$

The channel resistance depends on the voltage applied over the plate. For a nominal voltage of 1000 V R_{MCP} is $\sim 70 \text{ M}\Omega$ resulting in a channel resistance of about $10^{14} \Omega$. The MCPs consist of two different materials: the structure (grey), which consists of a type of lead glass and the hole, which is approximated with vacuum (white) (Fig. 34). The area of the structure is equal to the area of the hexagon A_{ch}^{hex} minus the area of the channel hole A_{ch}^{hole} . The capacitance of one channel C_{ch} is:

$$C_{ch} = \frac{\epsilon_0(\epsilon_r \cdot (A_{ch}^{hex} - A_{ch}^{hole}) + A_{ch}^{hole})}{l_{ch}} \quad (79)$$

With ϵ_0 the vacuum permittivity, ϵ_r the relative permittivity of lead glass and l_{ch} the MCP thickness which is 0.3 mm. The manufacturer does not give details about the material characteristics as it is a company secret. In [33] is an analysis of different values for ϵ_r found in literature. These values are between 6 and 20. With these values, the resulting capacity is 5 aF per channel. The dead time of a single MCP channel is the channel resistance R_{ch} times the channel capacitance C_{ch} :

$$\tau = R_{ch} \cdot C_{ch} \quad (80)$$

This results in a dead time of $\tau = 500 \mu\text{s}$. With a duration of about 100 μs for the recording time of one waveform, this channel would be blind for the time when the next five waveforms are recorded. With $1.6 \cdot 10^6$ channels and assuming a uniform distribution of ions on the MCP surface, saturation is assumed at particle rates I_p higher than 10^9 particles/s. The current drawn by the MCPs due to that high count rate is the particle count rate I_p times the MCP gain G and the elementary charge q_0

$$I_{MCP} = I_p \cdot G \cdot q_0 \quad (81)$$

resulting in a current of $\sim 100 \mu\text{A}$. The MCPs have a leakage current between 6–30 μA . The additional current drawn by the NIM detector due to the amplification of the ions is lower than a few μA resulting in two decades of margin before the detector reaches saturation.

3. Instrument

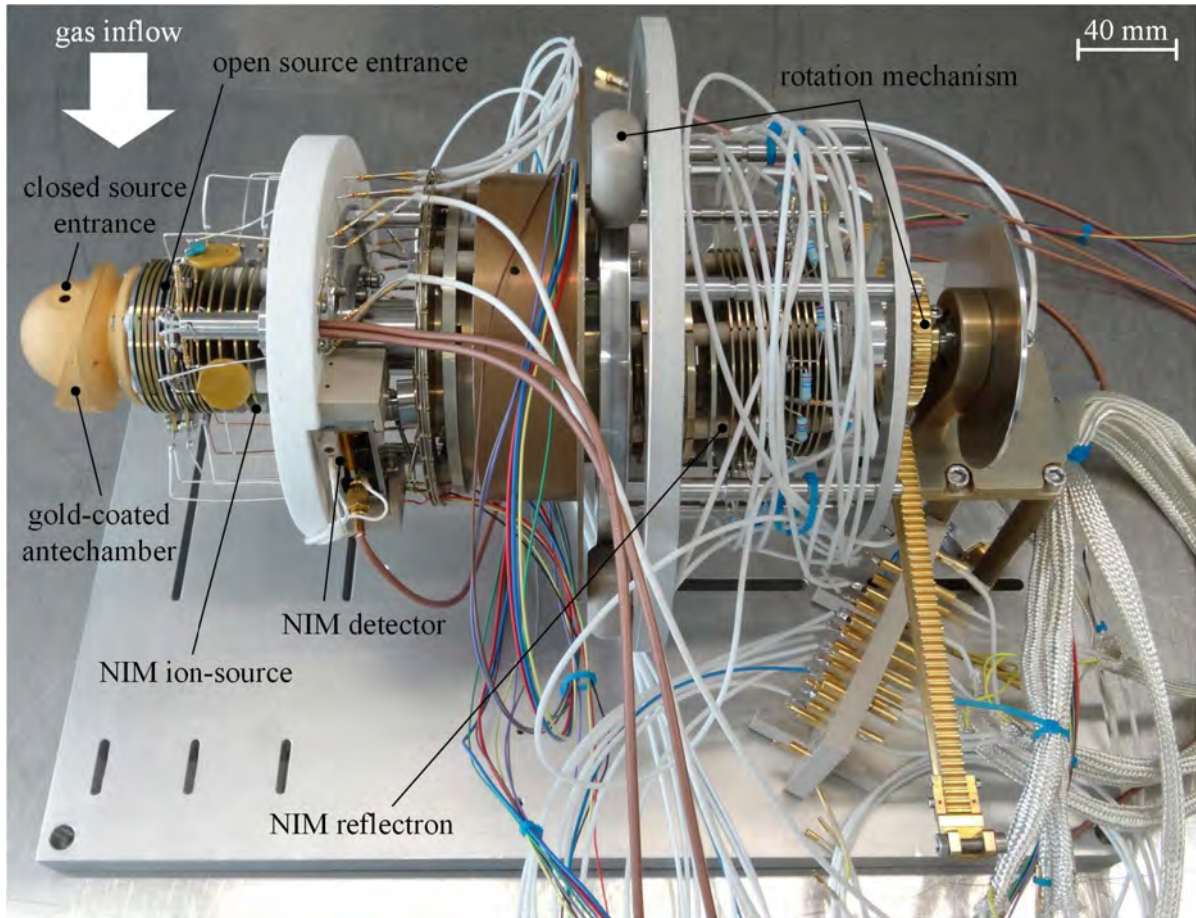


Figure 35: NIM Prototype [30].

This chapter compares the NIM prototype (Fig. 35) with the NIM ProtoFlight Model (PFM) (Fig. 36) from the mechanical point of view. It shows the key differences between the two models. Special focus lay hereby on the design of the detector because there were made some major design improvements.

Fig. 37 left shows the prototype antechamber and right the PFM antechamber. To improve the performance of the antechamber, the flight antechamber was made twice as big as the old one of the prototype. In addition, it has two entrance holes at $\pm 30^\circ$ relative to the x-axis of the instrument to be able to measure gas coming from both directions of the instrument (see Chap 2.6). The main inflow direction of the neutral particle beam generated by the CASYMIR test facility is 90° [19]. Therefore, a second flight-like test antechamber was made which has the second entrance hole at position 90° to be able to test the flight antechamber. The antechambers consists of two parts which are hold together with screws. Tests revealed that two of the mounting screws generate signal artefacts [31]. Therefore, the outer surface of the antechamber was redesigned (see also Chap. 4.2).

Fig. 38 shows the SIMION model of the Prototype ion-source, Fig. 39 shows the ion-source of

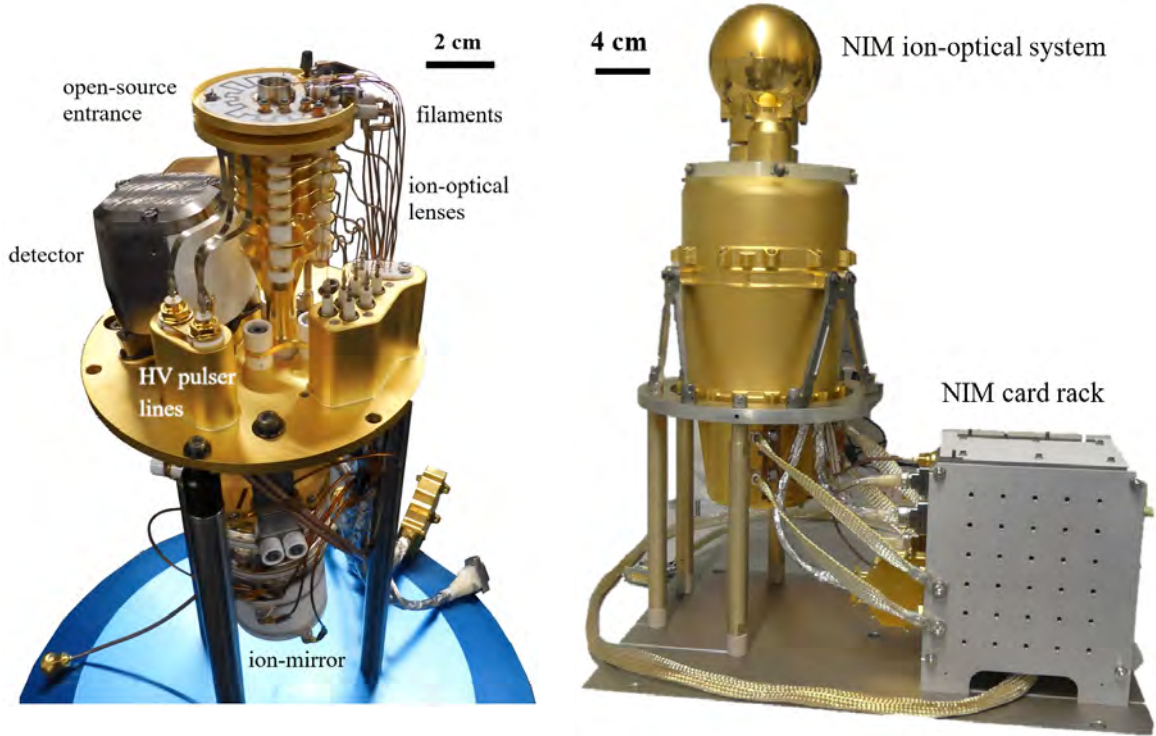


Figure 36: Left: NIM PFM ion-optical system without the closed-source antechamber. Right: NIM PFM ion-optical system with electronic box (card rack) attached [17].

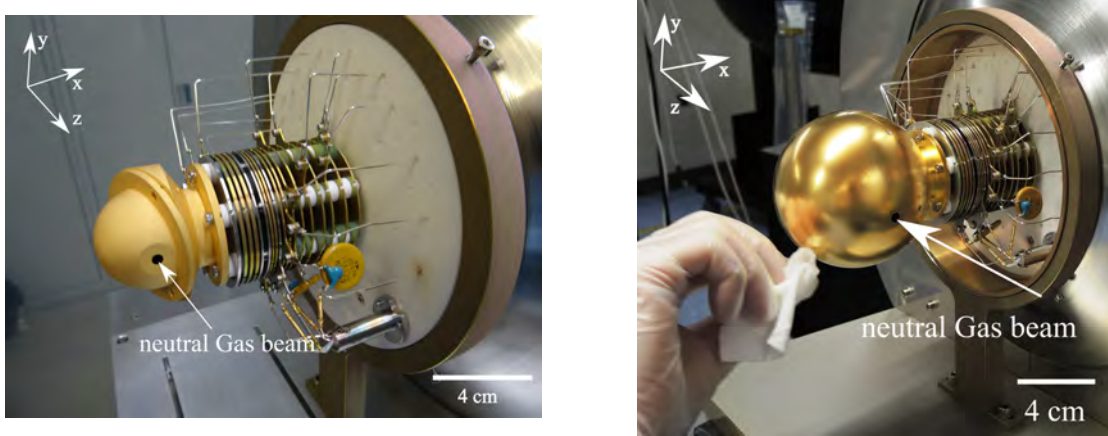


Figure 37: Left: Prototype antechamber [30]. Right: Flight-like antechamber.

the PFM and Fig. 40 shows the filament housing of the Prototype (left) and of the PFM (right). The PFM ion-source has seven electrodes less than the prototype to simplify the source and the flight electronics. Mainly LV electrodes were taken together such as IS1 & 2, IS3 & 4 and IS6 & 7. IS10 was removed and IS11 was shifted towards the ionisation region. In the filament housing the electron repelling electrodes Fil2–5 were taken together to one single electrode Fil2. The electron repelling electrode in the prototype was split into four parts to compensate

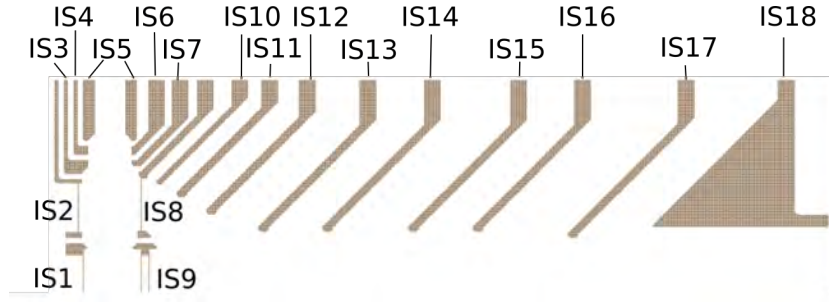


Figure 38: SIMION Model of the Ion-Source of the NIM Prototype [30].

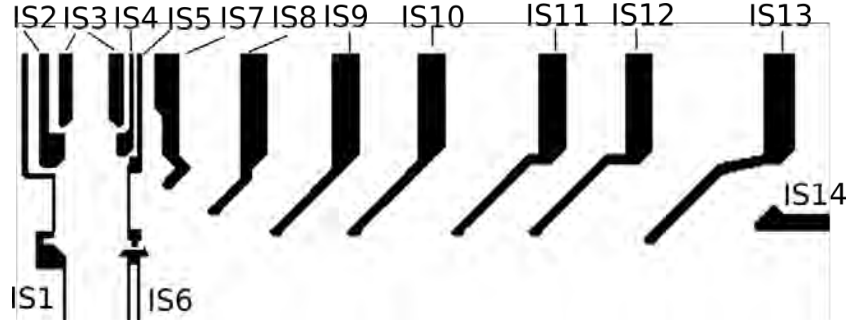


Figure 39: SIMION Model of the Ion-Source of the NIM ProtoFlight Model.

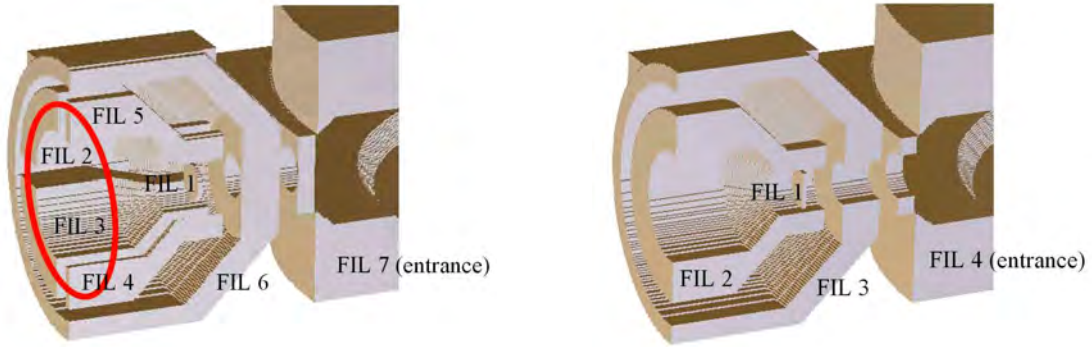


Figure 40: Left: Prototype filament housing [30]. Right: PFM filament housing [30].

with the electric fields for a bad alignment of the filament. For the PFM, the mounting of the filament holder was improved and therefore these four electrodes could be taken together to one single electrode.

Fig.41 shows a schematics of the ion-mirror. The prototype ion-mirror consists of 14 ring-electrodes (R2–R15). R1 is the drift tube. Between the electrodes R4–R15 are resistors to connect the electrodes with each other to generate a linear voltage gradient when a voltage is applied at electrodes R4 and R15. In addition, a voltage can be applied on electrode R8 allowing additional focusing of the ions in the ion-mirror. The flight ion-mirror consists of a ceramic tube with two resistance spirals on its inner walls replacing electrodes R5–R7 and R9–R14. From the electrical point of view, the two ion-mirrors behave the same.

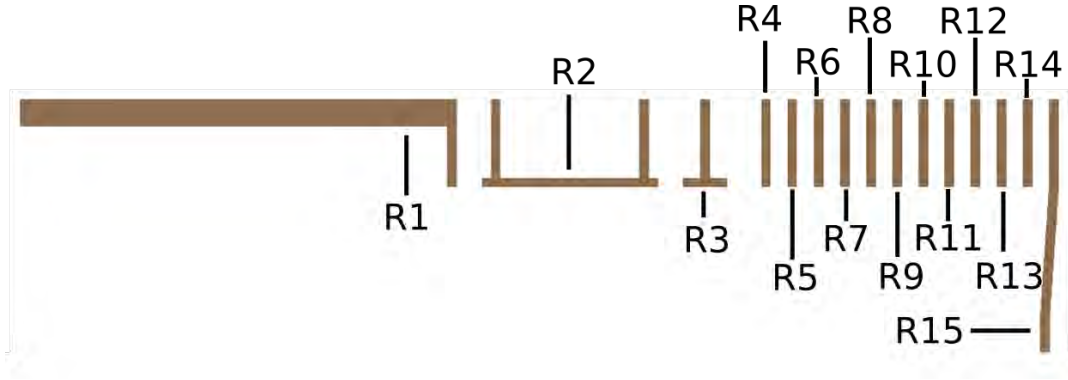


Figure 41: SIMION Model of the ion-mirror of the NIM Prototype [30].

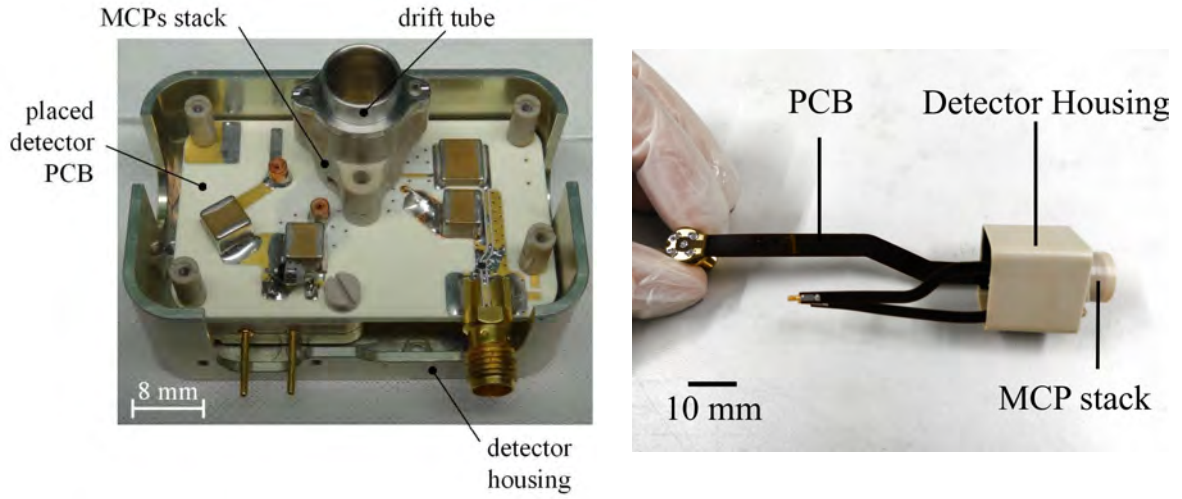


Figure 42: Left: NIM Prototype detector [30]. Right: NIM Flight detector without its radiation shield.

The NIM Prototype detector has a rigid Printed Circuit Board (PCB) on which the electrical components and the drift tube with the MCP stack are mounted (Fig. 42 left). Due to Jupiter's strong radiation field, the detector has to be shielded to reduce the noise level induced by the strong radiation and to increase the detector's lifetime. To minimize the required shielding mass, the flight detector has to be very compact. This was achieved by using a flex PCB to fold the detector into a peek housing (Fig. 42 right). Fig. 43 left shows the schema of a preliminary design of the peek housing containing the MCPs. The MCPs lay on a ledge 1 mm above the anode. A diode generates a voltage between the MCP backside and the anode to accelerate the electrons from the MCP backside towards the anode (see electrical schema Fig. 44). There are two contact lugs on top and at the bottom of the MCP stack to apply a voltage over the MCPs. The MCPs are fixed with a peek screw within the housing. In the old design, the screw

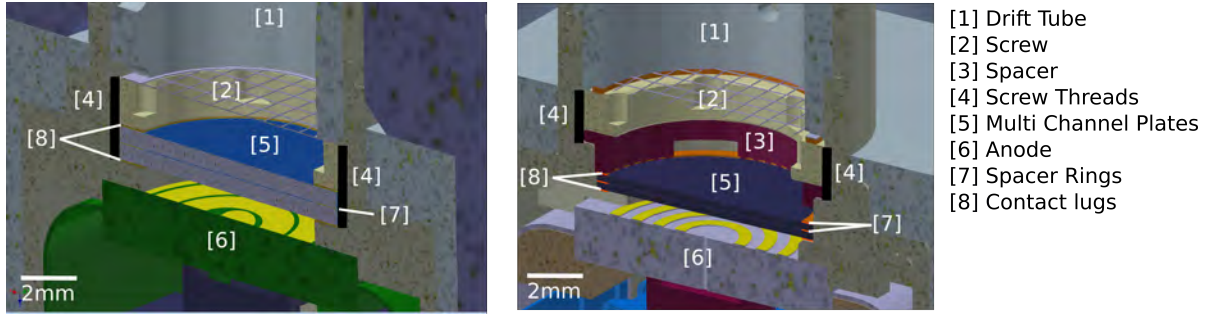


Figure 43: Schematics of the PFM detector housings. Left: preliminary design. Right: final flight design.

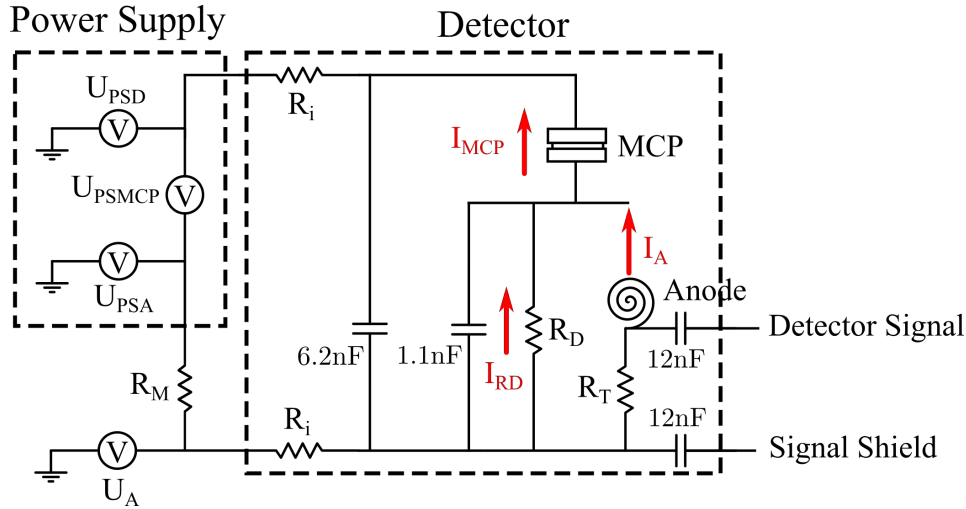


Figure 44: Electrical schematics of the NIM flight detector with laboratory electronics attached.

threads were milled down to the ledge. When the MCPs were mounted, they often canted in the threads. In addition, it was not possible to determine, how much the screw had to be tightened. When the screw was tighten too much, the MCPs broke as they consist of lead glass and are therefore very fragile. When the screw was too loose, the two contact lugs had no reliable contact to the MCPs. When applying a high voltage over the whole MCP stack, the gaps between the contact lugs and the MCPs act as an additional resistors over which the voltage builds up resulting in a discharge between the electrodes and the MCPs. The discharge can propagate through the whole MCP stack and damages the readout electronics. As a consequence, the screw thread was milled less far and an additional mechanical stop was made to tighten the screw only down to that stop (Fig. 43 right). This prevented the MCPs from canting in the screw thread thus it was not milled down to the bottom of the lower ledge and with the mechanical stop, the screw could not be tightened too much to break the MCPs. In addition, a peek space was added between the screw and the MCPs to push down the MCPs uniformly. Due to the tolerances in the manufacturing process of the different parts of the housing, metallic spacer rings are added between the peek spacer and the contact lug of the

top MCP to close the resulting gap. The number of added rings varies between each detector because the gap is different for each manufactured housing. With this design, the contact between the MCPs and the contact lugs could be improved but from the electrical point of view its still not a clean electrical contact. To make the system more robust against discharges the Zener diode was exchanged through a resistor (R_D in Fig. 44). The flight electronics sets the voltage U_{stack} between the top MCP and the anode. The MCPs and the diode act as resistors, which are connected in series. Therefore, the potential drop over the MCPs depends on the potential drop over the diode. The voltage drop over a Zener diode is 180 V independent of U_{stack} . Therefore, the voltage over the MCPs U_{MCP} is 180 V lower than U_{stack} . When having a resistor R_D instead of a diode, the voltage over the MCPs cannot be calculated by just having U_{stack} because the resistance of the MCPs R_{MCP} depends on the voltage U_{MCP} applied over them. It also changes with time due to ageing because the conductive material inside the MCP channels degrades over time. Therefore, the current I_{MCP} flowing through the system has to be known to be able to calculate U_{MCP} . The NIM flight electronics is not designed to measure this current because it was designed for a detector with a diode where a current measurement would be unnecessary. A calibration with the laboratory electronics was done to determine the relationship between U_{stack} and U_{MCP} (Chap. 4.7).

In the following section, U_{MCP} is derived as a function of the different voltages known when measuring with laboratory electronics. Fig. 44 shows the circuit diagram of the detector when operated with laboratory electronics and Table 4 summarizes the used variables. The current flowing through the MCPs I_{MCP} is measured with the resistor R_M :

$$I_{MCP} = \frac{U_{RM}}{R_M} \quad (82)$$

With U_{RM} the voltage over the resistor R_M which is:

$$U_{RM} = U_{PSA} - U_A \quad (83)$$

$$= U_{PSMCP} + U_{PSD} - U_A \quad (84)$$

With U_{PSA} the power supply output voltage for the anode, U_A the voltage applied on the detector anode, U_{PSD} the power supply output voltage applied at the top contact lug of the MCP stack and U_{PSMCP} the voltage difference between the two power supply outputs. U_{PSMCP} is:

$$U_{PSMCP} = U_{RM} + 2 \cdot U_{Ri} + U_{RD} + U_{MCP} \quad (85)$$

With U_{Ri} the voltage over the input resistors R_i , which are there to damp noise coupled into the detector circuit from the power supply:

$$U_{Ri} = I_{MCP} \cdot R_i \quad (86)$$

U_{RD} is the voltage over the resistor R_D replacing the former diode. The current I_A induced when an ion generates an electron avalanche, is very low compared to the current I_{RD} . Therefore, $I_{MCP} = I_{RD}$ and:

$$U_{RD} = I_{MCP} \cdot R_D \quad (87)$$

Solving Eq. (85) to U_{MCP} and inserting the different voltages results in:

$$U_{MCP} = U_{PSMCP} - U_{RM} - 2 \cdot U_{Ri} - U_{RD} \quad (88)$$

$$= U_{PSMCP} - U_{PSMCP} + U_{PSD} - U_A - 2 \cdot I_{MCP} R_i - I_{MCP} R_D \quad (89)$$

$$= (U_A - U_{PSD}) \cdot \left(1 + \frac{2R_i + R_D}{R_M}\right) - U_{PSMCP} \frac{2R_i + R_D}{R_M} \quad (90)$$

R_D	Resistor replacing the former diode	U_A	Voltage on the detector anode
R_i	Detector input resistor	U_{MCP}	Voltage over the MCPs
R_M	Resistor used to determine I_{MCP}	U_{PSA}	Anode voltage output of power supply
R_{MCP}	MCP resistance	U_{PSD}	Drift voltage output of power supply
R_T	50 Ω termination	U_{PSMCP}	Voltage difference between U_{PSA} and U_{PSD}
I_A	Current induced in the MCPs when an ion hits the MCPs	U_{RD}	Voltage over R_D
I_{ion}	Ion current hitting the MCPs	U_{Ri}	Voltage over R_i
I_{MCP}	Current flowing through the MCPs	U_{RM}	Voltage over test resistor R_M
I_{RD}	Current flowing through R_D		

Table 4: List of the variables used in the schematics of the flight detector Fig. 44 when the detector is operated with laboratory electronics.

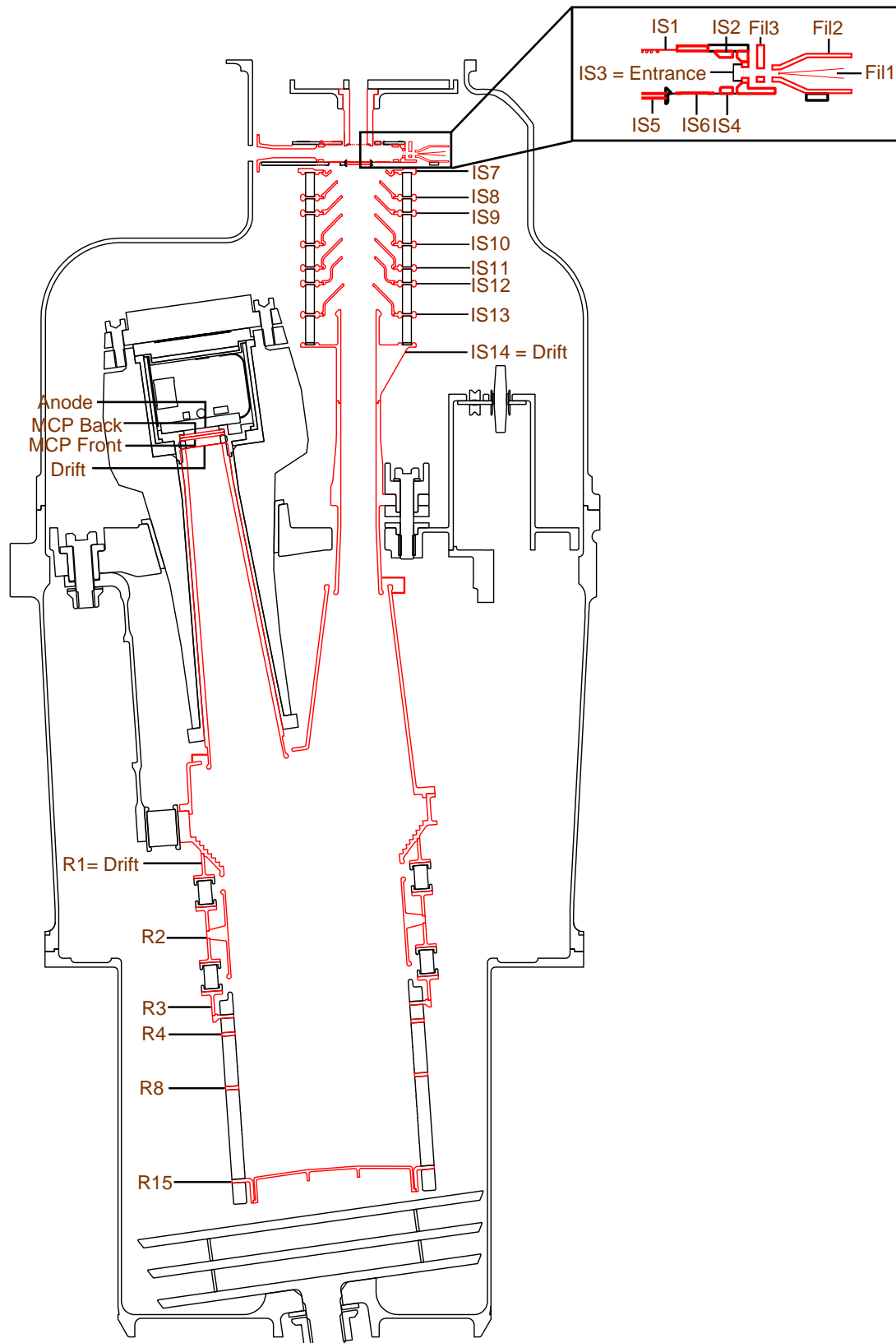


Figure 45: Schematics of the NIM flight design with all electrodes marked in red.

4. Experiments

This section includes tests of flight components and also system tests of the NIM Proto Flight Model (PFM) and the Flight Spare (FS) model. The tests of the flight ion-mirror and the flight antechamber were performed with the NIM Prototype where the other tests were performed with the NIM PFM model unless otherwise mentioned.

4.1. Flight Ion-Mirror **Finished**

In this section the performance of two ion-mirrors is compared. As described in Chapter 3, the prototype ion-mirror consists of several ring-electrodes connected with each other with resistors to generate a linear voltage gradient. The flight ion-mirror consists of a ceramic tube with two resistance spirals replacing some of the ring-electrodes. Fig. 46 left shows the prototype ion-mirror and Fig. 46 right shows the flight ion-mirror mounted to the NIM prototype in the test setup. An ion-mirror of the same type as the flight ion-mirror was also used in the RTOF mass spectrometer, which flew in ROSINA [34] and the in the NGMS [23]. From the electrical point of view, the two ion-mirror types behave the same.

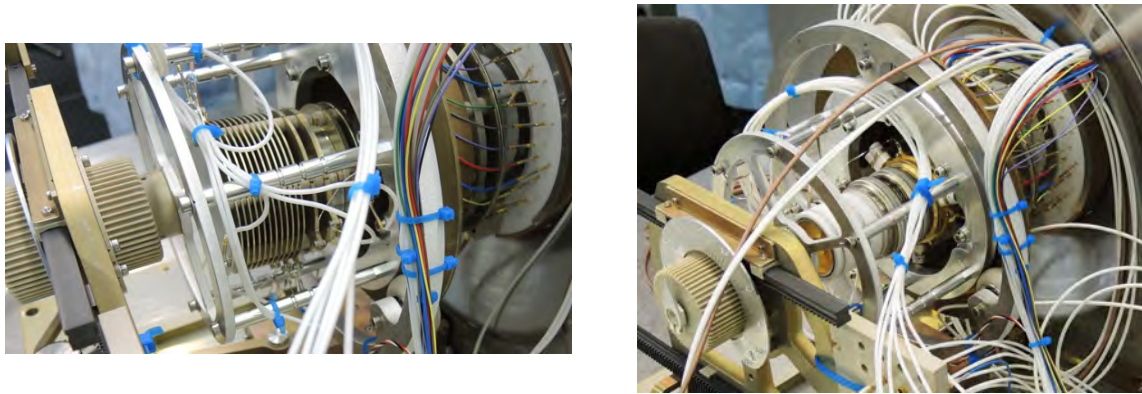


Figure 46: Left: Prototype with prototype ion-mirror with ring-electrodes. Right: Prototype sensor with flight ion-mirror.

The measurements were performed in a vacuum chamber. The residual gas pressure for the measurements with the prototype ion-mirror was $5 \cdot 10^{-10}$ mbar and for the measurements with the flight ion-mirror $1.4 \cdot 10^{-9}$ mbar. The test gases were injected directly through a leak valve to increase the chamber pressure up to $1 \cdot 10^{-8}$ mbar. The used test gases were: Ne, Ar, Kr and Xe. 3 Mio. single spectra were histogrammed for each of the measurements. All voltages of the instrument were manually optimized for the measurements with the two ion-mirrors. Table 5 shows the signal-to-noise ratios and the mass resolution of the different test gases measured with the two instrument configurations.

The SNR of the measurements with the flight ion-mirror is for all gases lower than the SNR of the measurements with the prototype ion-mirror. This is due to the higher amount of

Gas	SNR ProtoR	SNR PFMR	m/ Δ m ProtoR	m/ Δ m PFMR
²⁰ Ne	2022.9	562.4	200 \pm 12	236 \pm 16
⁴⁰ Ar	4732.6	1808.4	212 \pm 9	267 \pm 15
⁸⁶ Kr	746.1	414.3	224 \pm 7	292 \pm 12
¹³⁶ Xe	185.5	97.1	265 \pm 8	332 \pm 13

Table 5: Table listing the signal-to-noise ratios (SNR) and the mass resolution (m/ Δ m) of the prototype ion-mirror (ProtoR) and the flight ion-mirror (PFMR).

residual gas in the vacuum chamber during the measurements with the flight ion-mirror. The mass resolution of all of the test gases is higher when measuring with the flight ion-mirror. Therefore, the flight ion-mirror has passed the test. **Rewrite the discussion. Especially about the SNR!!!**

4.2. Flight Antechamber **finished**

After successfully testing the flight ion-mirror, the flight antechamber was tested. A picture of the prototype and the flight antechamber is shown in Fig. 47. The antechambers consist of two parts. In the old design the two parts of the antechamber had a rim on which the screws were mounted to put the two parts together. These screws were at position $\pm 45^\circ$. Tests with this antechamber revealed that neutral particles hit these screws and scatter into chamber (Fig. 48 a) [31]). Therefore, an antechamber with a flat outer surface was required. In the new design the screws are recessed into the 1 mm thin surface of the antechamber to get rid of the needed rim in the old design. In addition, the new antechamber is by a factor two bigger than the prototype antechamber with the aim to get more signal. Simulations of the flight trajectory revealed that two holes were required at positions $\pm 60^\circ$ to get optimal signal [9]. The CASYMIR test facility is not able to shoot the neutral particle beam under an angle of 60° onto the instrument. To test the new design, an slightly different antechamber was used with the second entrance hole at position $\theta_0 = -90^\circ$ instead of -60° . With a rotation mechanism, the instrument can be rotated around the x-axes by $\pm 90^\circ$.

These measurements were conducted at the CASYMIR test facility at the University of Bern. CASYMIR is able to generate a neutral particle beam with velocities up to 5.5 km/s [19]. For these measurements the particle velocity was about 2.5 km/s because this is the velocity of the spacecraft in Ganymede orbit, which will be 90% of the measuring time of NIM.

Fig. 48 a) shows measurements conducted with the thermal mode when the old antechamber was attached [31]. For these measurements, the instrument was rotated around the x-axis by keeping the beam at the same position. When rotating the antechamber, the hole moves out of the neutral particle beam because the beam is smaller than the antechamber. The expected intensity distribution I_{ant} is a combination of the function of the moving hole through the

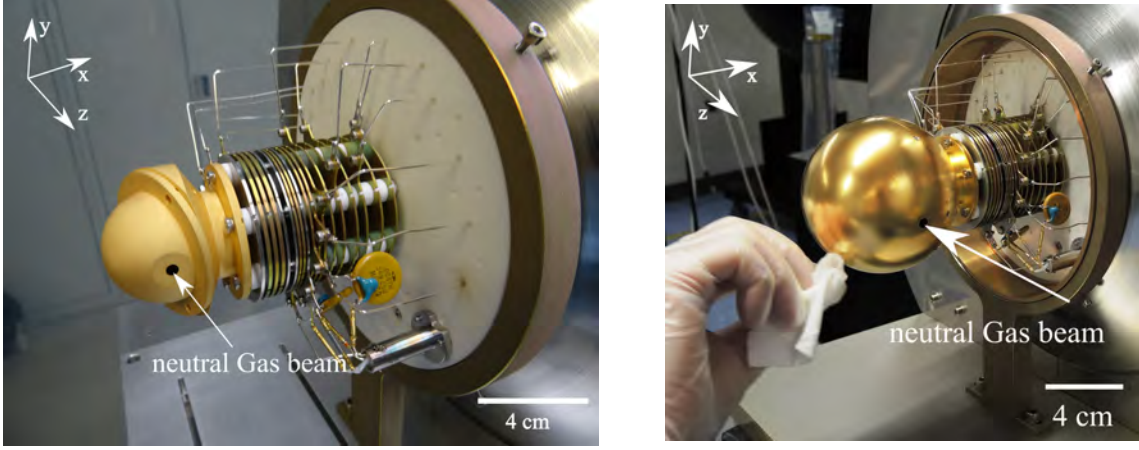


Figure 47: Left: Prototype antechamber. Right: flight-like antechamber with two entrance holes at positions $+60^\circ$ and -90° .

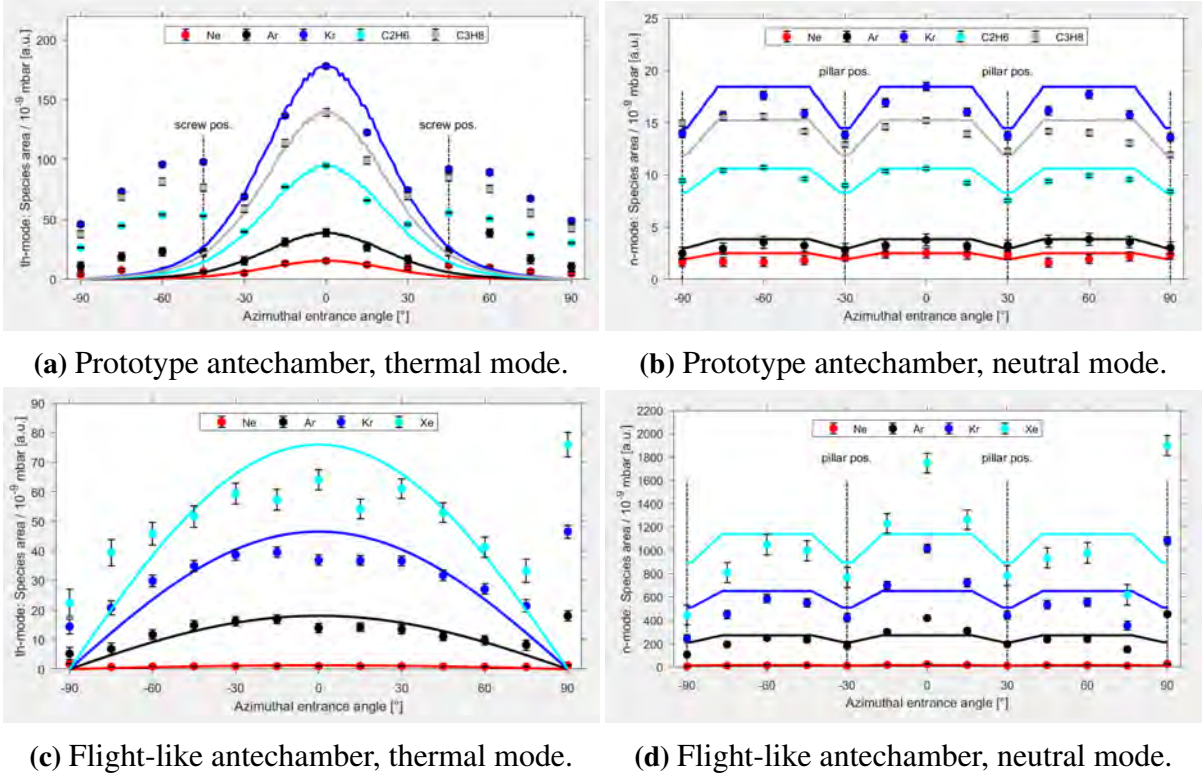


Figure 48: Panel a) and b) show measurements done with the NIM Prototype sensor with the old antechamber attached. a) shows measurement conducted with the thermal gas mode and panel b) shows measurements of the neutral mode respectively [31]. c) and d) are the corresponding measurements performed with the new antechamber attached to the NIM Prototype.

beam with a normal distribution:

$$I_{ant} = \frac{A}{\sigma\sqrt{2\pi}} \int_{x_{min}}^{x_{max}} \exp \frac{(x-\mu)^2}{2\sigma^2} dx \quad (91)$$

With A a constant taking the beam intensity into account, σ the standard deviation of the beam and μ the position of the beam centre relative to the centre of the antechamber, which is zero in this coordinate system. The borders of the integral (Eq. (91)) determine the section of the beam entering the antechamber:

$$x_{max} = r_{ant} \sin \alpha - r_{aHi} \cos \alpha \quad (92)$$

$$x_{min} = r_{ant} \sin \alpha + r_{aHi} \cos \alpha \quad (93)$$

With r_{ant} the radius of the antechamber and r_{aHi} the radius of the antechamber entrance hole. The sine contribution considers the shift of the hole in y-direction when the hole is rotated. The cosine contribution comes from the projection of the beam on the entrance hole. For the measurements with the new antechamber, the shift in y-direction when rotating the instrument was compensated by shifting the whole instrument. Therefore the sine contribution in Eq. (92) and Eq.(93) cancels leading to a cosine-like function.

When comparing Fig. 48 a) and c), the artefacts successfully vanished after the redesign. The higher intensity at angle $+90^\circ$ is most probable an outlier because it appears in both the thermal (Fig. 48 b)) and the neutral mode figure (Fig. 48 d)) of the measurements with the new antechamber. The lower measured signal intensity for the measurements with the new antechamber is a result of having an additional entrance hole which was necessary because of the flyby trajectories (see Chap.2.5).

Fig. 48 b) shows measurements conducted with the neutral gas mode with the old antechamber attached and Fig. 48 d) shows measurements conducted with the neutral gas mode when the new antechamber was attached. At position $\pm 30^\circ$ and $\pm 90^\circ$ are pillars holding the stack of the ion-optical lenses together. When the beam hits these pillars, the particles scatter in all directions leading to a reduction of the signal. For the neutral gas channel, no difference in the signal distribution and intensity is expected because a change in the antechamber design does not influence the signal measured with the neutral gas channel. The observed signal of the neutral gas mode when the new antechamber is attached, is significantly higher than with the old antechamber. This is due to a better voltage set. A different voltage set for the voltages in the ionization region changes the distribution of the electron beam thus leading to a different ion distribution in the ionization region. This leads to a different angular distribution of the signal for the neutral gas channel when comparing the results of the two measurement series.

4.3. Density Enhancement **finished**

For the first tests with the NIM PFM, the front side of the NIM instrument was scanned with the neutral particle beam to find the position of the entrance slit and the antechamber entrance hole to align the beam properly with the instrument. Fig. 49, left panel shows the scan of the front side and Fig. 49, right panel shows the corresponding structural part. The antechamber

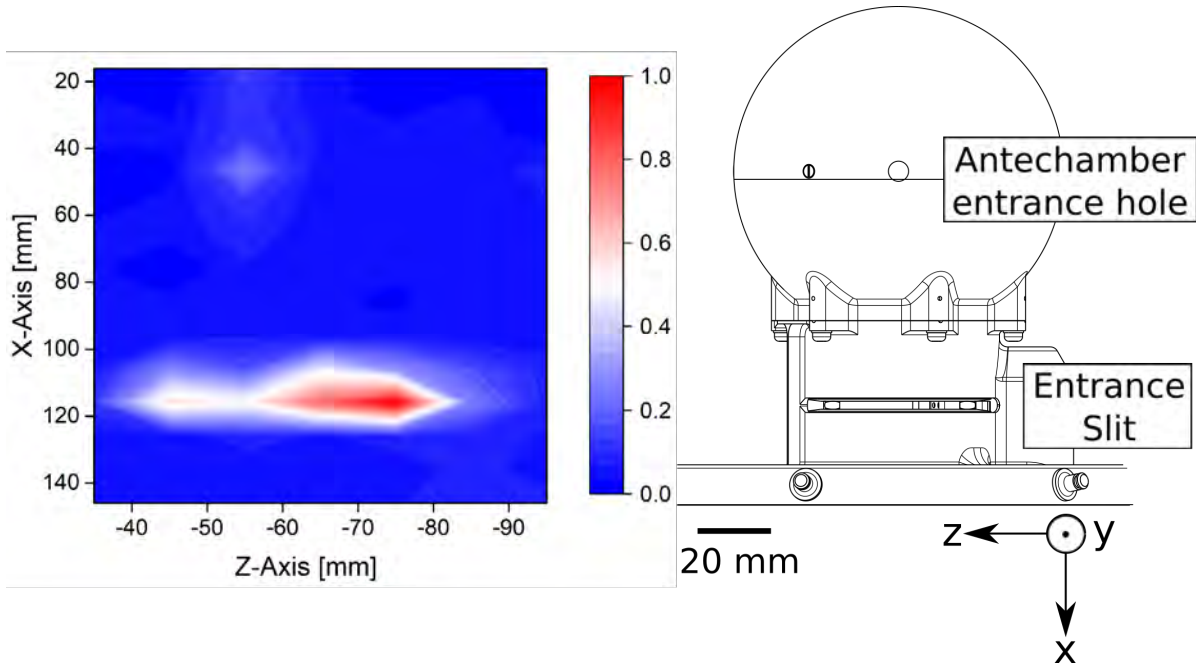


Figure 49: Left: Intensity profile when shooting with the neutral particle beam at the structure of the NIM PFM instrument. Right: Front view as seen by the neutral particle beam.

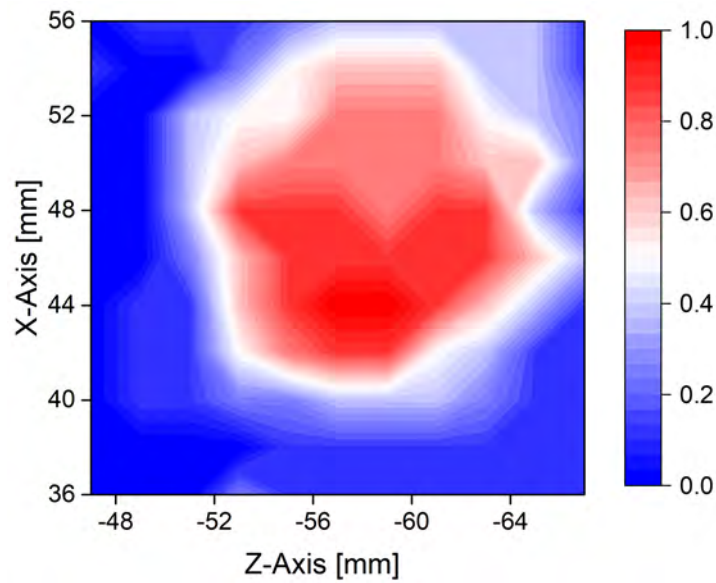


Figure 50: Zoom on the antechamber hole when shooting with the neutral particle beam at the structure of the NIM PFM instrument.

entrance hole is clearly visible as a small dot. Fig. 50 shows a zoom with a better resolution of the antechamber entrance hole which shows a nice Gaussian distribution. When looking at the entrance slit, there are two positions with increased intensities. The zoom on Fig. 51

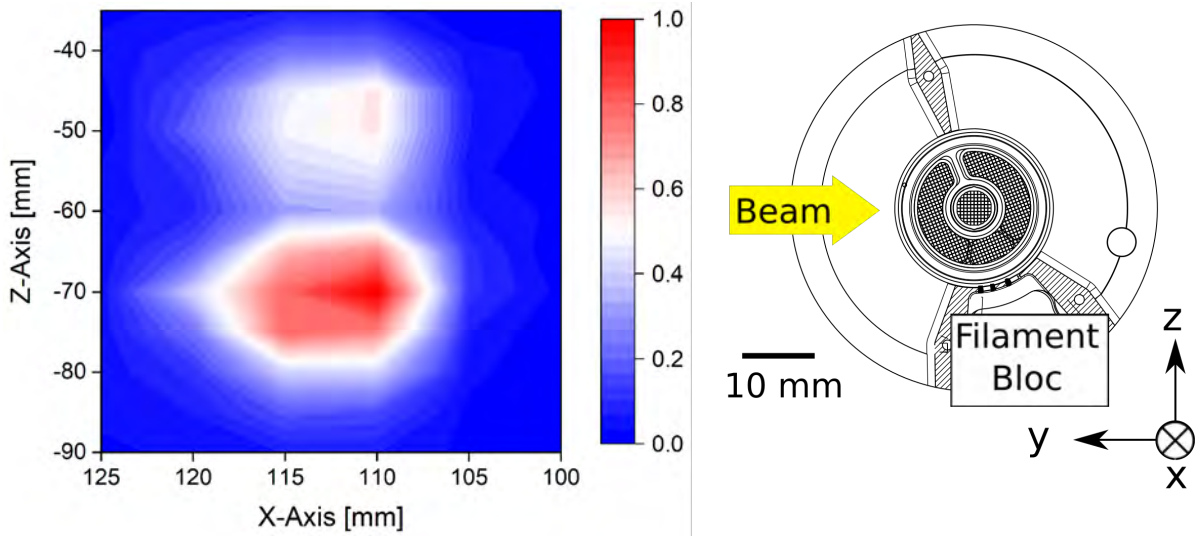


Figure 51: Left: Zoom on the entrance when shooting with the neutral particle beam at the structure of the NIM PFM instrument. Right: Top view on the entrance.

reveals that the positions of biggest intensity is where the beam hits the structure covering the two electron emitting filaments. The other intensity maximum is where the beam hits the supporting structure opposite of the filament bloc. When the gas hits these structures, the gas slows down leading to a local increase of the gas density. Therefore, the structure partially thermalizes the gas similar as the closed source antechamber. This was not intended because with the neutral gas channel the aim is to measure incoming particles directly without any interaction with the structure. In the design of the PFM, the filament bloc and the supporting structure act like a funnel directing the scattered gas to the central grid. The thermalization of the incoming gas when it hits the filament bloc is unavoidable. For the supporting structure opposite of the filament, a pillar instead of the plate like structure would have been the better option. When the gas hits the pillar, the pillar scatters the gas in all directions instead of scattering only in the direction of the central grid. This phenomenon was observed when doing a similar measurement with the NIM prototype (Fig. 52).

The ion-source of the prototype had six pillars holding the different focusing lenses together. In Fig. 52 the pillars are marked as red circles. The electron emitting filament was opposite of the main gas inflow direction. For these measurements, the ionization region was scanned with the neutral particle beam at angles 0° and $\pm 60^\circ$ to direct the beam in between the pillars over the extraction grid. When scanning from the front side, the signal intensity has a nice Gaussian shape. When scanning the ionisation region at angles of $\pm 60^\circ$ the Gaussian distribution is visible when the neutral particle beam is aligned over the centre grid with an asymmetry toward the side of the filament bloc. The gas hitting the filament bloc gets thermalised leading to a higher signal than on the other side where the gas only scatters on the pillars. Here the signal increase due to thermalization is less dominant than in the design of the PFM because the part of the filament structure seen by the beam is tilted outward. At distances bigger than ± 25 mm from the centre, the signal drops again. This is where the beam is completely outside of the ionization region.

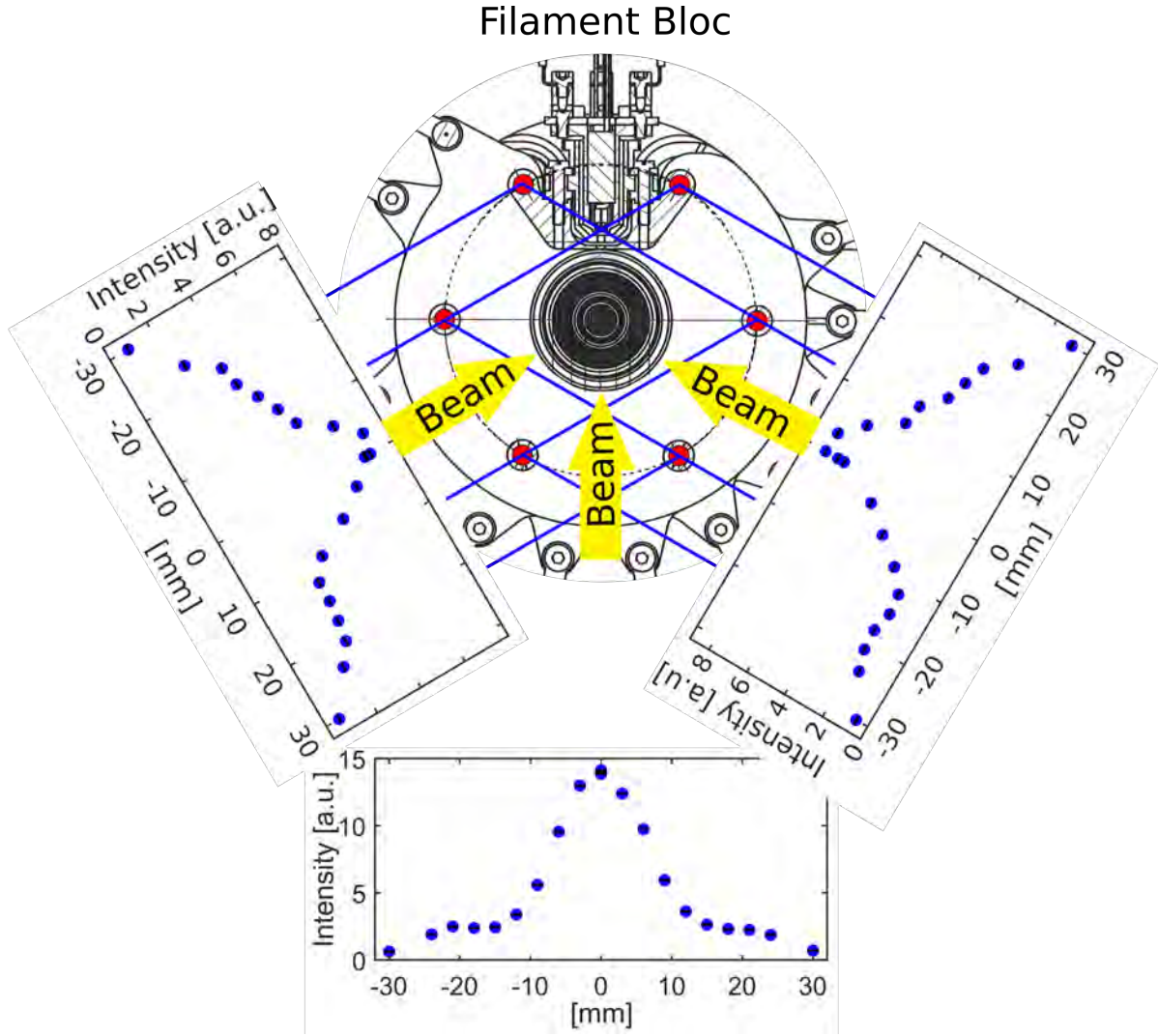


Figure 52: Zoom on the entrance when shooting with the neutral particle beam at the structure of the NIM Prototype. The red circles mark the positions of the pillars holding the ion source together.

4.4. Entrance Ion and Electron Position Simulations

This chapter shows at which start positions the ions in the ionisation region have to be when the extraction pulse is applied to successfully reach the detector. In addition, this chapter includes simulations of the flight path of the electron beam which is used to ionize the neutral particles.

Fig. 53 top shows the ionization region from the side. The pink tube opposite of IS5 is the tube connecting the antechamber with the ionization region. Neutral particles are ionized with an electron beam (blue arrow) and pulled into the spectrometer with the inner extraction grid IS5 (th-Mode and n-Mode). Ions penetrating the ionization region are pulled with the outer extraction grid IS6 into the spectrometer (i-Mode). Fig. 53 bottom shows the top view of the

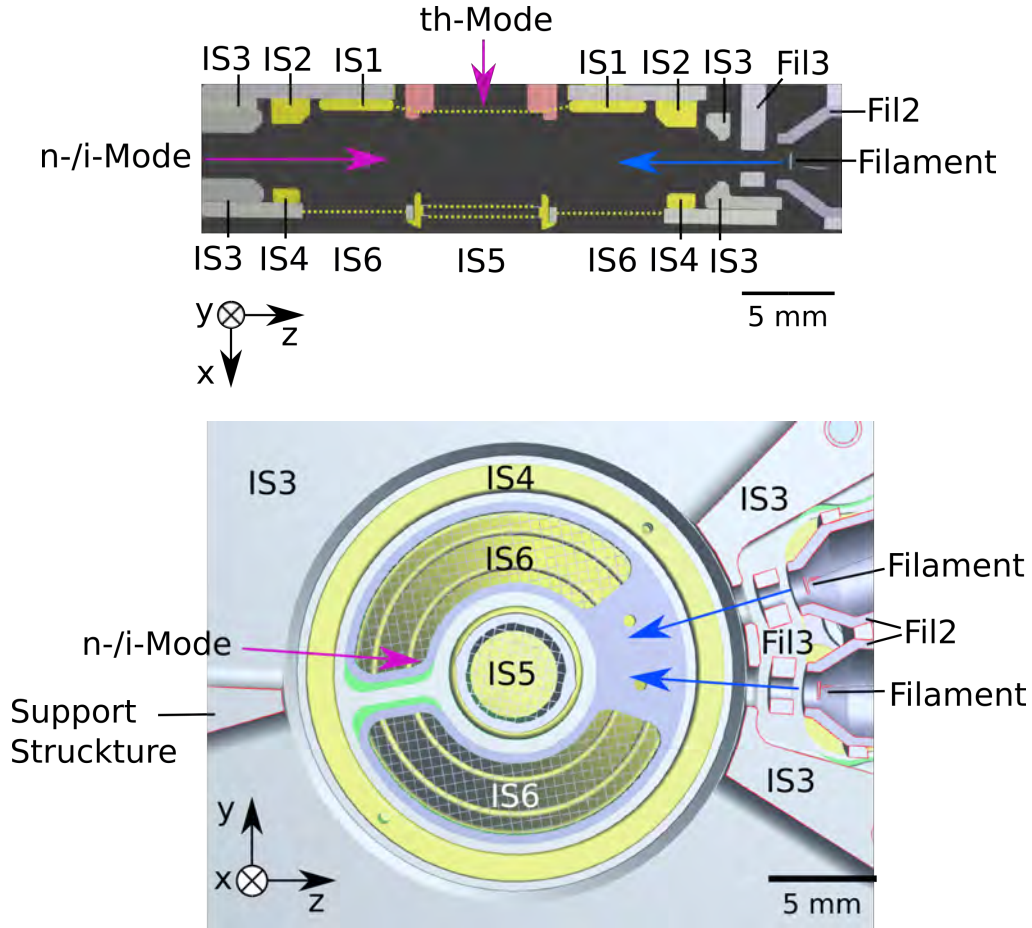


Figure 53: Side (top) and top view (bottom) of the ionisation region. The violet arrows mark the gas inflow direction and the blue arrows mark the direction of the electron beam.

ionisation region when looking from the antechamber. On the right side are the two filaments used to generate the ionising electron beam and on the left side is a supporting structure to support the antechamber from the other side. In n-Mode and i-Mode, the gas can enter the ionisation region from every direction in the yz-plane except from where the filaments and the supporting structure are, resulting in a field-of-view of 300° . For the lab measurements, the gas inflow direction is from the bottom as it is also shown in Fig. 51. For the simulations, a gas inflow direction parallel to the electron beam was chosen as it is marked in Fig. 53 bottom. The generated ions of the th- and n-Mode were generated in a cuboid volume with a height of 2 mm and a square base area of 8×8 mm. For the simulations of the i-mode, the base area was 20×20 mm because the ions are pulled with the outer extraction grid into the spectrometer. Fig. 54 a) and c) show the simulated data for thermal mode where the particles have thermal velocity. Fig. 54 b) and d) show the simulated data for the neutral mode and Fig. 55 shows the simulated data for ion mode where the penetrating neutrals and ions respectively have a velocity of 4 km/s. The particles are displayed as velocity vectors. The ions marked in blue

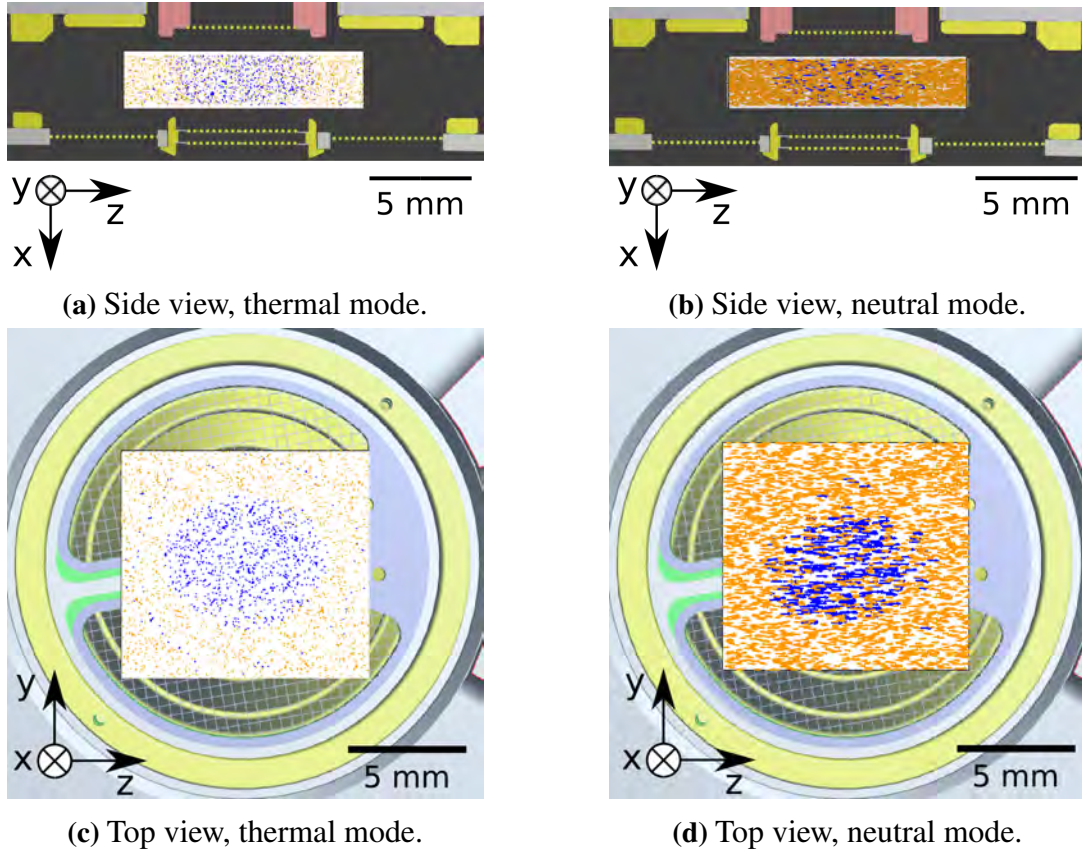


Figure 54: Simulated ions marked as small arrows starting at different positions in the ionisation region. The ions in n-mode enter the entrance with 4 km/s. Ion reaching the detector are marked in blue and ions hitting the structure during their flight to the detector are marked orange.

are the ones reaching the detector and the orange ones hit the structure somewhere during their flight to the detector. The simulated particles have unit masses from 1 up to 1000 m/z. Fig. 54 shows that only ions reach the detector which are generated directly above the inner extraction grid IS5 which is also the one extracting the ions in these two modes. In thermal mode, also some ions generated over the outer grid IS6 reach the detector. They are visible as a small blue ring close to the structure separating the inner and the outer grid in Fig. 54c). In thermal mode the neutral particle flow comes through the pink structure and is directed over the inner pull grid. Therefore, only a small amount of gas reaches the outer grid. In neutral mode, only ions generated over the inner grid reach the detector due to their velocity perpendicular to the x-axis of the instrument. In ion mode, the ion optics is optimized for ions penetrating the ionisation region from the side as it is shown in Fig. 56. Due to their charge, ions react to the electric field as soon as they are close to the ion-optical lenses of the ionisation region. Their main starting position is therefore at the edge of the ionisation region and not in the centre as it is for the neutral particles. The ionisation of the neutral particles is focused on the central extraction grid and therefore, most of the ions are generated above the inner extraction grid

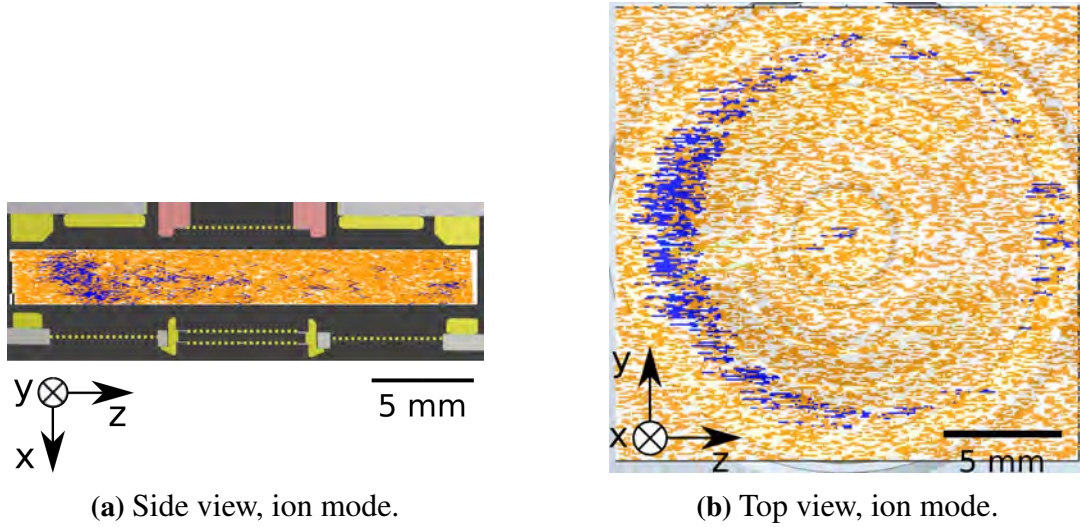


Figure 55: Simulated ions marked as small arrows starting at different positions in the entrance slit with a velocity of 4 km/s. The blue ions reach the detector where the orange ions hit the structure during their flight to the detector.

IS5 when measuring with the thermal and the neutral mode channels start. When measuring with the ion mode, the ion-optical system is optimized for ions starting close the focusing lenses in the ionisation region as it is shown in the simulations in Fig. 56 and Fig. 55. The central grid is close to 0 V to additionally deflect the ions.

Fig. 57 and Fig. 58 show the flight path of the electrons which are used to ionise the neutral gas. During vibration tests of the sensor, a weakness in the structure of the ion source was identified. This lead to a small redesign where the opening for the electron beam in the entrance electrode IS3 had to be enlarged (Fig. 57). Simulations were done to see how big the impact of that design adaption was. Fig. 57 bottom panel shows the old design with an additional ring to reduce the diameter of that hole and the top panel shows the new design without the ring in the entrance electrode. Dark blue is the flight path of the electrons and light blue shows the electric potential lines. The adaption of IS3 had not impact on the flight path of the electrons. As previously discussed, the aim is to ionise the cylinder volume above the inner pull grid because only ions generated in this volume will reach the detector. Therefore, the electron beam should cover the whole volume. Fig. 58 shows the top view from the ionisation region. The porous ring structure is the outer extraction grid IS6. The inner grid is covered by the electron beam. In this model, only one filament is display. Between the two potentials lines which mark the 50 V ring is electrode IS4 which is on 130 V. Fig. 57 top and Fig. 58 show, that with the applied voltages the electron beam covers the whole volume over the inner extraction grid.

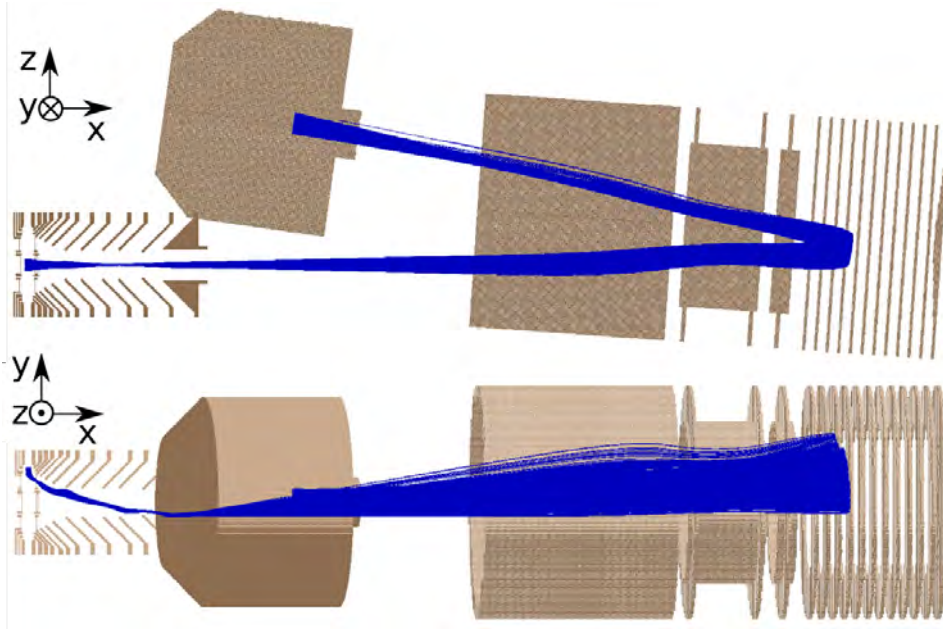


Figure 56: SIMION model of NIM prototype with ion trajectories in optimised i-mode, from -y direction [30].

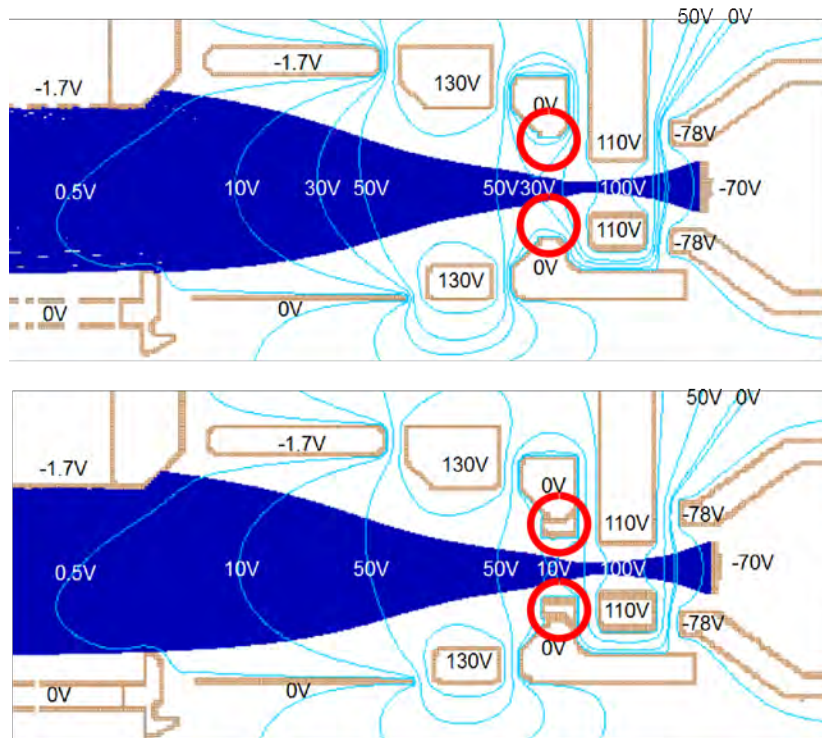


Figure 57: Top: New entrance with enlarged hole for the electron beam. Bottom: Old entrance with additional ring to reduce the diameter of hole.

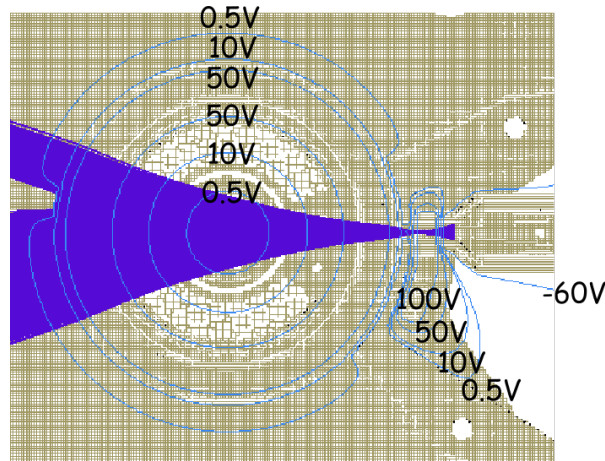


Figure 58: Top view into the entrance of NIM with simulated electron beam (dark blue) and potential line (light blue).

4.5. Shutter Performance Test **finished**

When measuring with the neutral gas channel, the aim is that the particles are measured directly without any interaction with the structure of the instrument. Therefore, a shutter between the antechamber and the ionization region was required to close the particle entrance from the antechamber. In this section the performance of the shutter was tested. According to the model stated in Chap. 2.7 the shutter should attenuate the signal from the antechamber by a factor 600.

These tests were performed with the NIM PFM. The PFM was operated with laboratory electronics. The tests were performed at the CASYMIR test facility. The used particle beam consisted of hydrogen and xenon with a velocity of 2 km/s. Three different measurements were performed: One with the beam directed onto the antechamber with the shutter open, one with the shutter closed and a background measurement, where the particle beam was pointed onto the outer structure of NIM to estimate how much of the signal arises from the test gas scattering into the ionization region when the beam is directed in an arbitrary direction. This background was subtracted from both signals before they were divided through each other to determine the damping factor G_{close} of the shutter.

The resulting attenuation factor of the shutter is 12 instead of the required 600 with a proper fabricated shutter. The biggest impact has the actual thickness of the gap between the shutter and the antechamber when the shutter is closed. The damping reduces significantly when the gap is bigger than actually designed. This is shown in Fig. 32 in Chap. 2.7. With a gap size of about 0.1 mm instead of 0.01 mm the damping factor is only about a factor 25. Other reasons are that the portion of the beam which scatters on the antechamber outer walls gets thermalized in the vacuum chamber and adds to the signal intensity in the neutral channel, which is estimated to contribute equally to the measured signal. In the outer space, the gas scatters on the antechamber but does not reach the ionization region because it will flow around the instrument.

4.6. Pulser finished

The high-voltage pulser is used to accelerate the generated ions in the ionisation region to a certain energy. During the time when no high voltage pulse is applied, the potential has to be stable at the bias voltage to allow ion storage as previously discussed in Chapter 2.4.

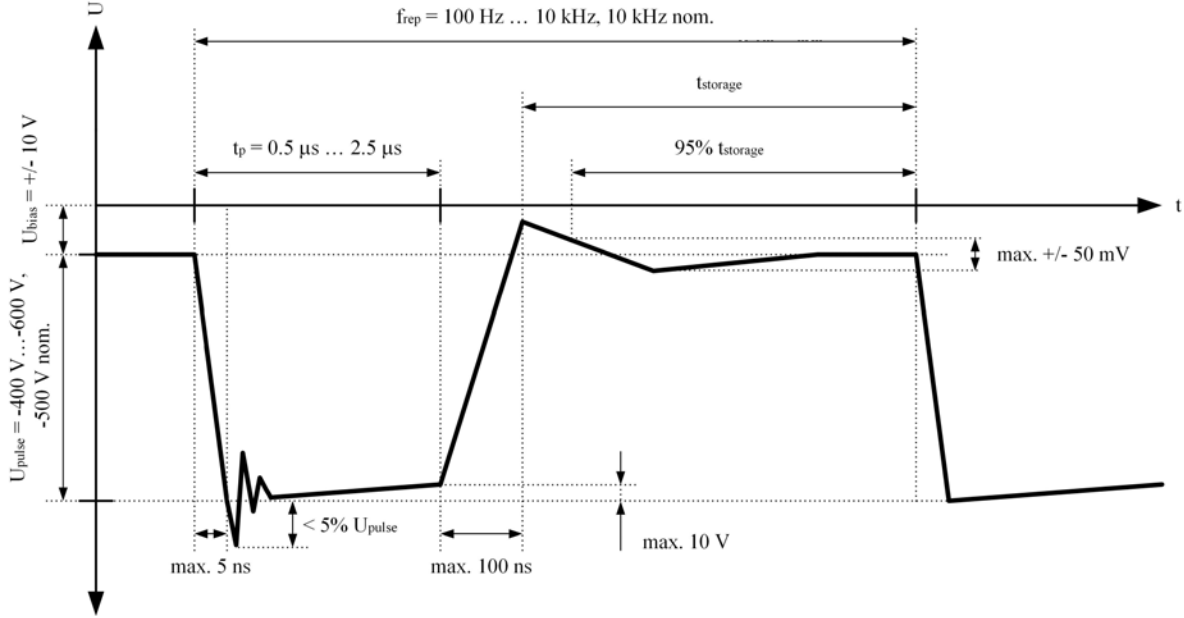


Figure 59: Specifications for the pulse shape generated by a realistic pulser [30].

Fig. 59 shows a schema of a realistic high voltage pulse and Table 6 shows the characteristics of the flight pulser compared to the requirements. The fall time is the time to build up the negative high voltage on the extraction grid. This time has to be very short to give all ions the same amount of energy. When the fall time is long, low mass ions receive less energy resulting in a lower mass resolution for these species. A fall time of 1 ns leads to a 0.1 % lower mass resolution of hydrogen compared to an ion with mass 200 u. A fall time of 5 ns results in a reduction by 10 % (see Chap. 2.1). The fall time of the flight pulser is a bit longer than according to the specifications. When applying a high voltage, the pulse overshoots its set value and drops slightly. The overshoot and the voltage drop result in a variation of the ion energy for the different species. The ringing of the high voltage, and the pulse drop of the flight pulser are within the specifications. The pulse duration has to be longer than 0.2 μs because that is the minimum time ions with masses of 1000 u need to leave the ionisation region. With some margin, the specifications were set to 0.5 μs. The rise time to bias voltage should be smaller than 100 ns to leave enough time for ion storage. This is well achieved with the flight pulser. The ripple of the bias voltage should be smaller than ±50 mV to generate a stable electric field during the time when no high-voltage is applied on the extraction grid. A variation by ±100 mV of the voltage of the electrode opposite of the pulser grid results in a

visible variation of the signal intensity during manual optimisation with laboratory electronics. However, the baseline ripple of the flight pulser exceeds this value.

	Ringings of HV Pulse	Pulse drop at full HV	Baseline Ripple	Fall Time	Rise Time
Requirement	$< 5\%$	$< 10\text{ V}$	$\pm 50\text{ mV}$	$< 5\text{ ns}$	$< 100\text{ ns}$
Flight Pulser	2.5%	1.9 V	300 mV	5.76 ns	19.7 ns

Table 6: Characteristics of the flight pulser compared with the requirements.

4.7. Detector Tests **finished**



Figure 60: NIM flight detectors ready for tests. Top: flat configuration. Bottom: folded configuration.

This chapter describes the testing procedure of the flight detectors and shows calibration results. The flight detectors consist of a flexible PCB (Printed Circuit Board) with a peek housing for the MCPs (Chap. 3). Due to Jupiter's harsh radiation environment, the NIM detector has to be shielded with a tungsten copper shielding. To minimize the shielding mass, a flex PCB was used to fold the detector into the small peek structure to minimize the detector volume. The detectors are tested in flat configuration with test MCPs and in folded configuration with flight MCPs (Fig. 60). The detectors were put in a vacuum chamber and baked out for 2 days. The conditioning was started one day after bake out when a residual gas pressure lower than $5 \cdot 10^{-8}$ mbar was reached. The conditioning procedure is attached in the Appendix Chap. A.2.

Depending on the outgas behaviour of the detector, the conditioning took 2.5 to 4.5 h. After the conditioning, the measurements of the detector gain were performed.

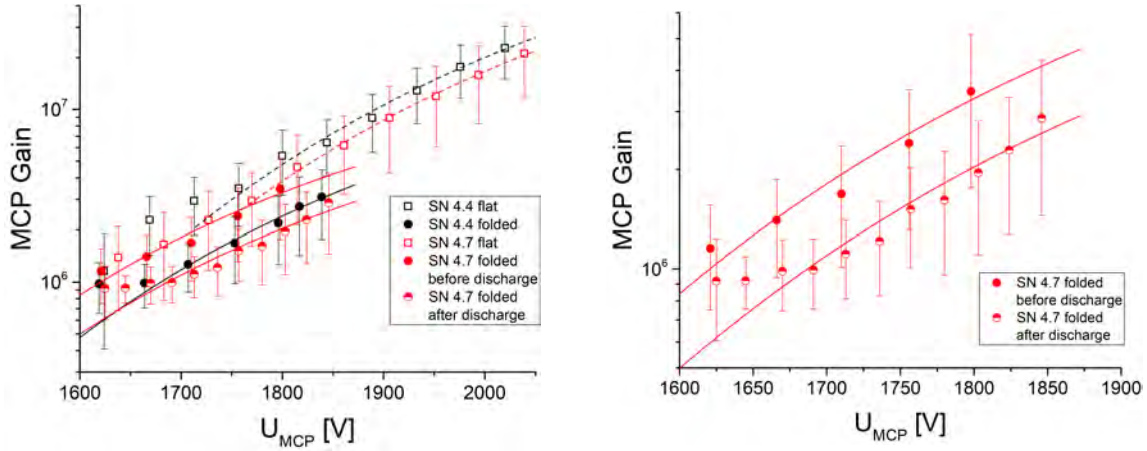


Figure 61: Left: Gain curves of two NIM FS detectors. The difference in gain is because for each measurement curve, a different set of MCPs was used. Right: Gain curves of a folded NIM FS detector. The lower gain curve was recorded after a discharge at an MCP voltage of 1.8 kV.

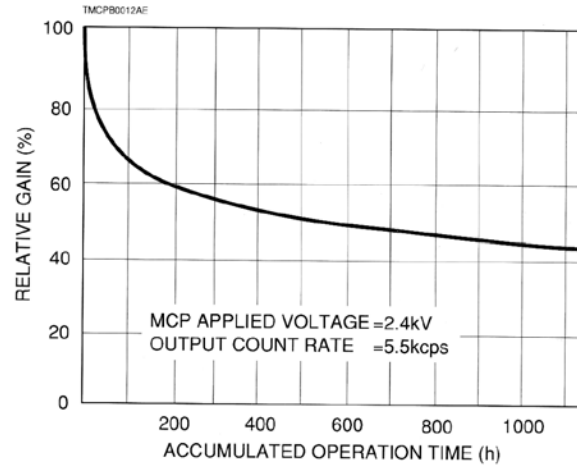


Figure 62: Relative gain of an MCP as a function of operation time [43].

Fig. 61 left shows the gain curves of two FS detectors in flat and folded configuration. The conditioning and the measurements in the folded configuration were done up to lower voltages to spare the potential flight MCPs. The gain of the MCPs depends on different factors. As described in chapter 2.8 the gain is a function of the voltage applied over the MCPs as it is shown in Fig. 61. The MCPs also degrade over time. This process depends on the residual gas pressure at which the MCPs are operated and the residual gas composition. The rapid decline

in gain during the first few operation hours is a result of cleaning the channels through operation (Fig. 62). When the MCPs were exposed to air, water and other substances deposit in the MCP channels. During operation, these deposits are sputtered and the surface of the channels are cleaned. After a few hours of operation, the gain reaches a plateau. In flat configuration SN 4.7 has a lower gain than SN 4.4 because its conditioning took longer than the conditioning of detector SN 4.4. Therefore it was cleaned better. In the folded state, SN 4.4 was 3 days longer in vacuum than SN 4.7 and had therefore more time to outgase. Fig. 61 right shows a zoom on the two measurement series of SN 4.7 both recorded in folded configuration. During the first measurement series, a discharge happened when the MCP voltage was at 1.8 kV. To amplify a signal, a minimal voltage has to be applied over the MCPs. When they are barely used, this voltage is in the range of 1.6 kV. During ageing, the decrease in gain can partially be compensated by increasing the voltage. When an ion induces an electron avalanche, the electrons are free in the channel and their main moving direction is towards the channel output. When a discharge suddenly lowers the applied acceleration voltage, these free electrons get pushed towards the channels walls due to space charge. These electrons destroy the conductive coating of the channels leading to a signal reduction of about 30 % per discharge. The higher the applied MCP voltage is, the higher is the signal loss.

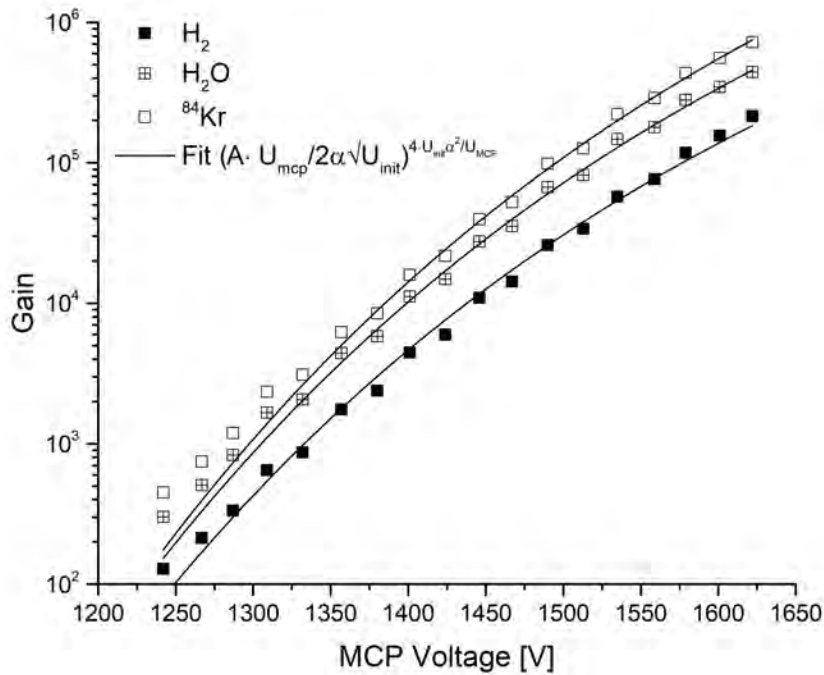


Figure 63: Gain curves of the detectors measured with the NIM FS ion-optical system.

Fig. 63 shows the gain curve of detector SN 4.7 recorded when it was build into the NIM FS instrument. H_2 and H_2O are part of the residual gas and ^{84}Kr is the used test gas. The curves follow nice the theoretical curve. The initial energy of the first electron U_{init} is about 6 eV and the probability A to emit the first electron is in the range of $0.3 \text{ eV}^{-1/2}$ for the three species.

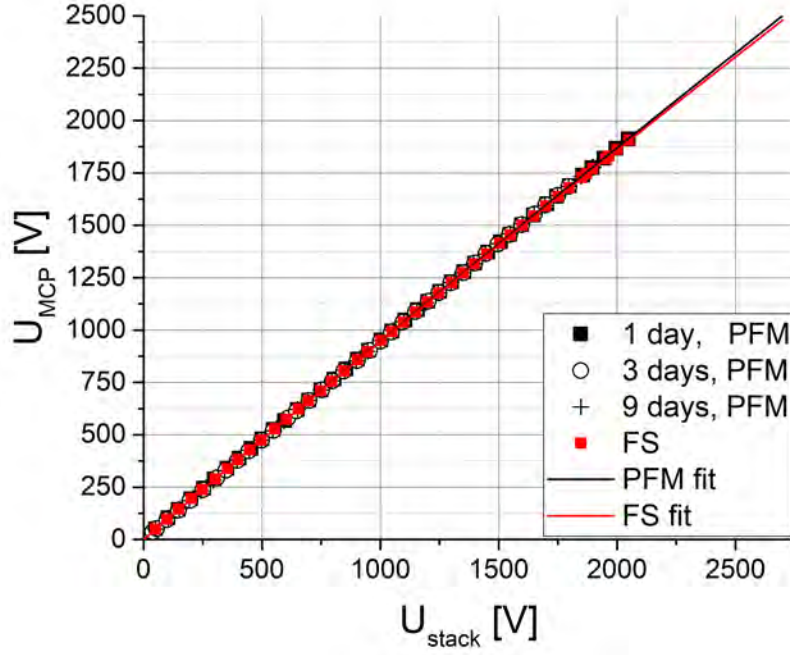


Figure 64: MCP voltage (U_{MCP}) as a function of the voltage applied between the MCP front and the anode (U_{stack}) for different measurement series with the PFM (black symbols) and the FS instrument (red squares) with the quadratic extrapolation.

	PFM	FS
a	$(-1.25 \pm 0.05) \cdot 10^{-5}$	$(-1.54 \pm 0.05) \cdot 10^{-5}$
b	0.96 ± 0.001	0.96 ± 0.001

Table 7: Fit parameters of the quadratic interpolation for the PFM and the FS detector for the function: $U_{MCP} = a \cdot U_{stack}^2 + b \cdot U_{stack}$.

The NIM flight detector has a resistor built in between the MCPs and the anode to accelerate the electrons from the MCPs towards the anode. The flight power supply sets the voltage between the MCP front and the anode U_{stack} . To determine the relation between the voltage over the MCPs U_{MCP} and the stack voltage U_{stack} a calibration was done with the laboratory power supplies. Fig. 64 shows the results of that calibration for the PFM and the FS detector with an quadratic extrapolation up to 2.4 kV for the MCP voltage. 2.4 kV is the upper voltage limit of the MCPs according to the manufacture. The fitparameters are in Table 7. The MCPs in the two detectors have similar resistances which is the reason why the measurement data

of the two detectors overlap. For the PFM detector, a longer measurement campaign was done to characterize the PFM instrument (Chap. 4.8.1). During that campaign, this curve was recorded frequently every time the instrument was turned on. The resistance did not change significantly during the short time of the measurement campaign.

4.8. Sensor performance tests

This chapter shows the performance of the NIM PFM and the NIM FS sensor when operated with laboratory electronics.

4.8.1. PFM

Include IEEE paper!!!.

4.8.2. FS finished

Ion Storage

Ion storage is very crucial for a time of flight mass spectrometer because every ion generated and not stored in the ion source is lost and can generate additional electrical noise on the detector signal line. In this test the ion storage capability of the ion source was analysed for thermal and neutral mode for hydrogen and krypton with velocities of 2 km/s and 4 km/s. The emission current was varied from 20 to 600 μA . Ion storage of positive ions in x- and y- direction is supported by the negative space charge potential generated by the electron beam (see Chap. 2.4). Two ring electrodes with a positive voltage applied generate a positive potential ring to trap generated ions in y- and z- direction (Fig. 65). For emission currents from 20 to 600 μA according to Eq. (43) the negative potential in the centre of the electron beam is -0.08 to -2.59 V. Fig. 66 left shows the ion storage behaviour of the ion source of hydrogen and right the ion storage behaviour of krypton. In case of no ion storage, the relationship between the electron emission current I_{em} and the signal intensity is linear because then only ions would be extracted which are generated during the time when the extraction pulse is applied on the extraction grid.

In case of ion storage there is a quadratic relationship between I_{em} and the signal intensity. When measuring with the thermal mode, the particles get slowed down until they have energies in the range of 0.01 eV and are therefore easy to trap in the potential field. When measuring with the neutral mode, particles enter the ionisation region directly. The kinetic energy of hydrogen for velocities between 2-4 km/s is 0.07-0.27 eV. Therefore it can be trapped with the potential field generated by an electron beam with an emission current higher than 20 μA .

The kinetic energy of ^{84}Kr for the same velocities is 2.8-11.2 eV. This energy exceeds the potential of the centre of the electron beam and the ions are therefore more difficult to trap with only the electron beam. The ions are kept in the middle of the ionisation region with the positive potential ring. According to Fig. 66 ion storage for ^{84}Kr starts to dominate at emission currents higher than 100 μA . In thermal mode, an increase in beam velocity leads to an increase in signal intensity due to the density enhancement effect (Chap. 2.5). Therefore a higher signal intensity is expected in thermal mode for 4 km/s compared to 2 km/s. Like in the PFM, the FS shows a nice ion storage behaviour. For krypton ion storage just starts at an emission current of 100 μA where hydrogen is stored already at lower emission currents due to its lower kinetic energy at the same beam velocity.

Mass resolution and Signal-to-Noise Ratio

According to the requirements stated in [24] NIM has to achieve a mass resolution for neutral mode of 500 and for thermal mode of 1000 but to be able to distinguish between different masses at unit masses of 1000 m/z NIM has to have a mass resolution of 1000. Otherwise, the different unit masses cannot be distinguished.

Fig. 67 shows two spectra recorded with the NIM FS sensor with laboratory electronics attached with an electron emission current of 100 μA . With a mass resolution of 708 for neutral gas mode NIM fulfils the requirements. In thermal gas mode the highest mass resolution achieved was 830 m/ Δm . Fig. 68 shows mass spectra recorded with the NIM FS sensor with

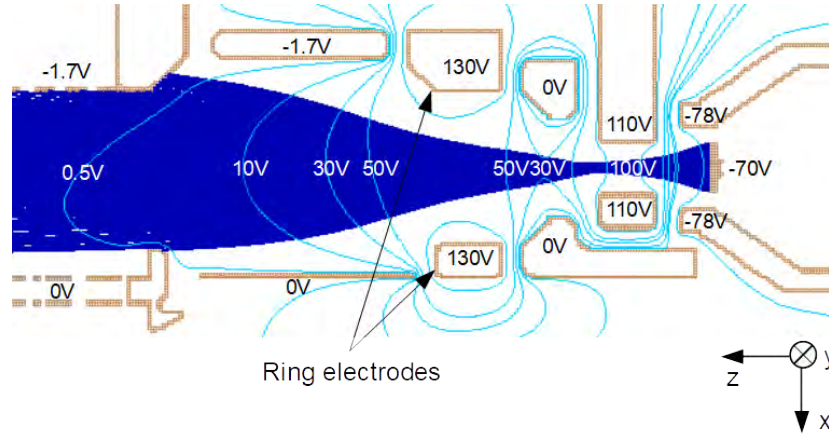


Figure 65: Ion storage source with sample voltage set applied to the electrodes. In light blue are the potential lines and in dark blue a simulated electron beam.

the flight electronics attached. The electron emission current was $200 \mu\text{A}$. The highest mass resolution achieved at the current state is $490 \text{ m}/\Delta\text{m}$ for neutral gas mode and $462 \text{ m}/\Delta\text{m}$ for thermal mode. The mass resolution can be improved by further optimizing the system. With an emission current of 300μ the ^{78}Kr isotope is visible in the spectrum which has a natural abundance of 0.36 % (Fig. 69).

The signal to noise ratio for the spectra recorded with the flight electronics is very low compared to the SNR of the spectra recorded with the laboratory electronics. The SNR can be improved by adding proper noise filters. A wandering noisy part is already identified. In Fig. 68 left and right it appears between masses m/z 40 and 70. In Fig. 69 it start right after the noise of the extraction pulse an ends at m/z 30. At the moment it is unclear what induces that noise but with a proper filter this noise can be detected and significantly reduced without affecting the mass signal peaks.

Fig. 70 shows a mass spectrum recorded with the FS sensor with the laboratory electronics attached. The highest SNR achieved was $6 \cdot 10^5$ and therefore almost 6 decades. The mass peaks m/z 355, 390 and 429 are some oil components with water adducts originating from the turbo pumps of the test facility. m/z 415 is an artefact generated by the algorithm used for the background subtraction. This peak is also wider then the other surrounding mass peaks. A SNR of 6 decades is important to conduct optimal measurements during the flybys at Jupiter's icy moon Europa. The particle density of Europa's exosphere is about $10 - 10^8 \text{ cm}^{-3}$ [38] corresponding to a pressure of $10^{-15} - 10^{-8} \text{ mbar}$. With a chamber pressure of $1.5 \cdot 10^{-9} \text{ mbar}$ NIM has to achieve a SNR of 6 decades to measure particles at a pressure of 10^{-15} mbar .

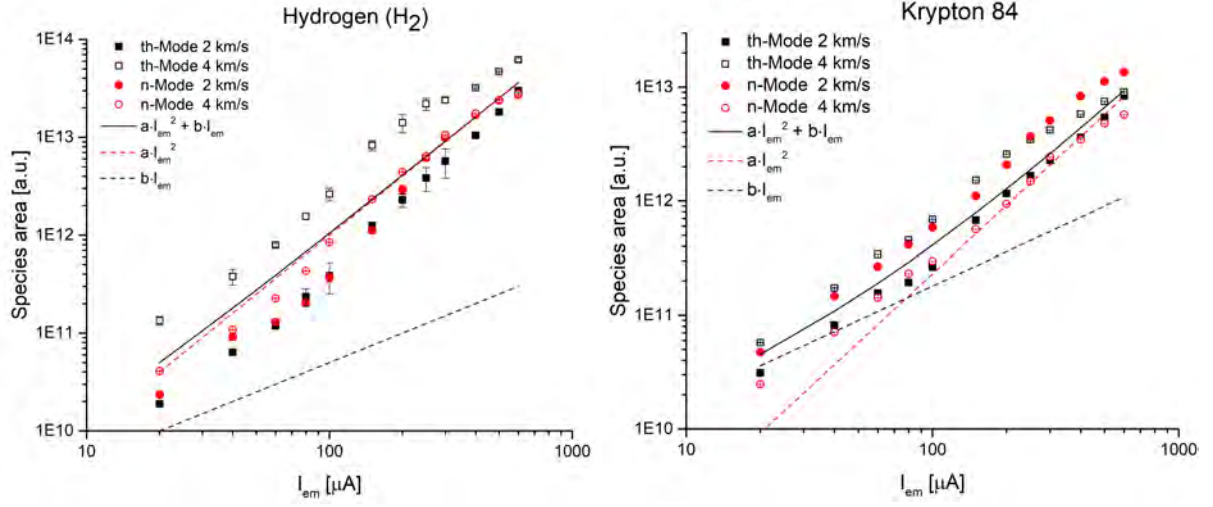


Figure 66: Ion storage measurements performed with the flight spare sensor operated with laboratory electronics for H₂ and ⁸⁴Kr for two different gas velocities.

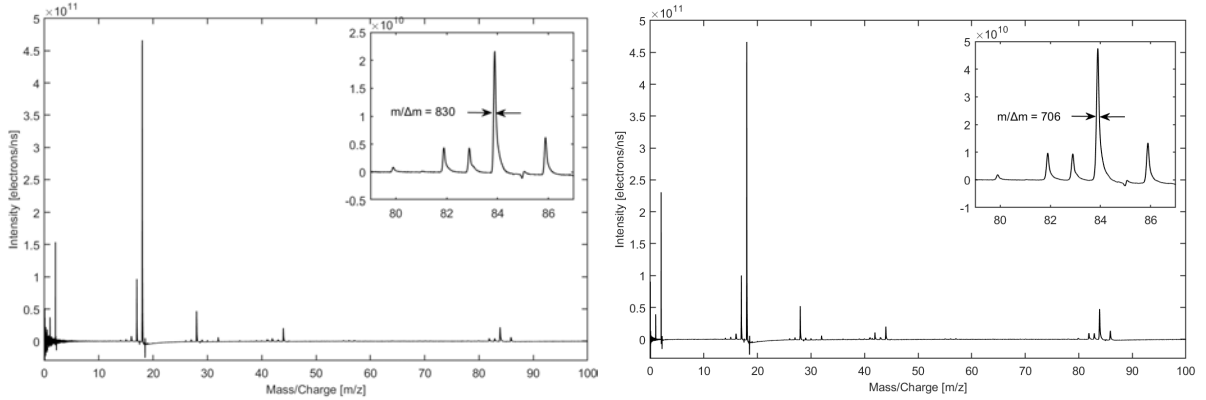


Figure 67: Mass spectra measured with the flight spare sensor with the laboratory electronics attached. Left: thermal gas mode. Right: neutral mode.

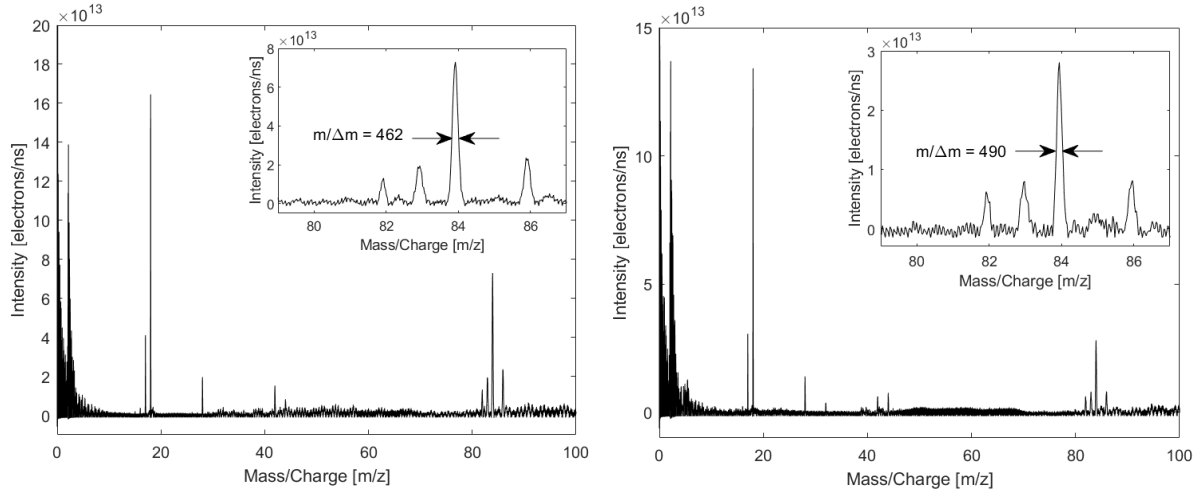


Figure 68: Mass spectra measured with the flight spare instrument with the flight electronics attached. Filament emission current was $200\ \mu\text{A}$. Left: thermal gas mode. Right: neutral mode.

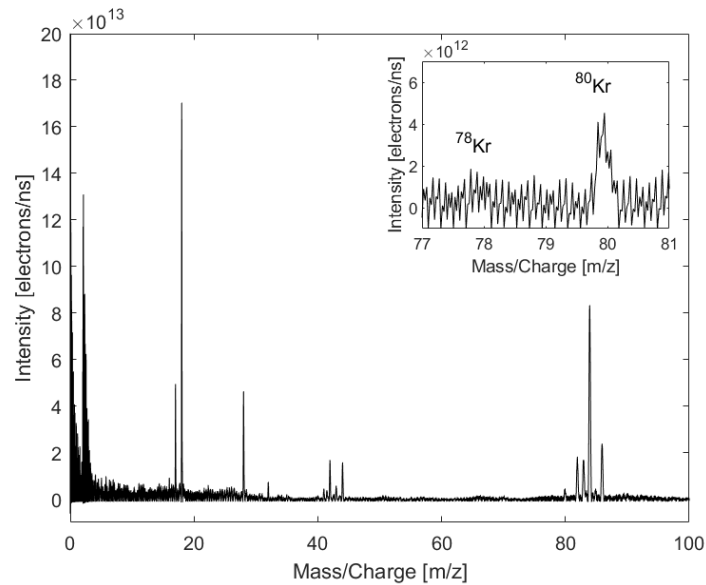


Figure 69: Mass spectrum measured with the flight spare instrument with the flight electronics attached with a filament emission current of $300\ \mu\text{A}$.

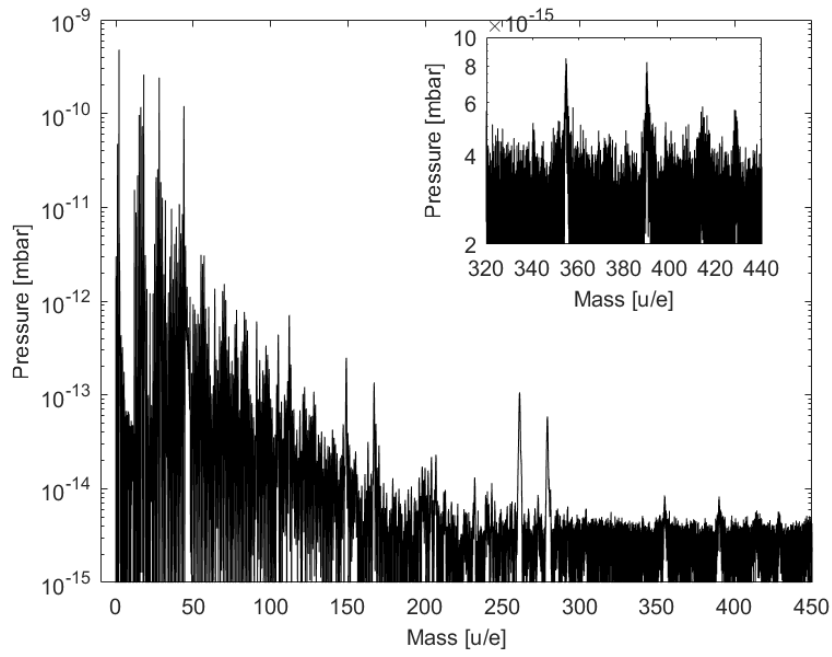


Figure 70: SNR plot for the flight spare sensor but with laboratory electronics attached. The residual gas pressure was $1.5 \cdot 10^{-9}$ mbar.

5. Conclusion

The thesis consists of two main parts. Chap. 2 showed theoretical analyses of different components of the NIM instrument and summed up theoretical aspects to understand the performance results of the different subsystems presented in Chap. 4. Chap. 4 ends with test results of the NIM PFM and FS sensors. This chapter sums up the most important findings from the calculations and tests from the before mentioned chapters.

The first analysis that was performed was a simulation to compare the impact of the ion temperature, the spacial spread of the ions in the ionisation region and the impact of the fall time of the high-voltage extraction pulse on the mass resolution (Chap. 2.1). The simulations revealed that compared to the other two effects the impact of the temperature on the mass resolution is negligible. The fall time of the extraction pulse has a major impact on low mass species. The fall time changes the potential in the ionisation region during the time when the ions get extracted. Ions with a lower mass/charge ratio (m/z) are therefore more affected. For a fall time of 5 ns, corresponding to the fall time of the flight extraction pulse, an ion with m/z of 1 has a 5 % lower mass resolution than an ion with m/z 200. When the fall time is smaller than 1 ns, the impact on the mass resolution is below 0.1 % according to the simulations. This fall time should be the target time for future pulse generator designs. The spacial spread of the ions in the ionisation region has the biggest impact on the mass resolution. To minimize it, proper focusing of the ions in the ionisation region is necessary of the ion-optical lenses.

The flight pulse generator fulfils most of the requirements. For future designs there is potential in reducing the ringing of the baseline voltage. This is the low voltage applied on the extraction grid during the time between two extraction pulses (Chap. 4.6).

Filament.

A detailed analysis of the different factors influencing the density enhancement ability of a closed source antechamber has been performed in Chap. 2.5. In this summary I focus on the parameters influencing the geometry of the antechamber. For details about the impact of the spacecraft velocity or the particle mass, read Chap. 2.5. The analysis showed, that the diameter of the hole connecting the antechamber with the ionisation region should to be bigger than 5 mm with the geometry of NIM's antechamber. A big hole area increases the probability that the thermalised particles from the antechamber flow into the ionisation region and not out of the entrance holes. In addition, the conductance of a tube decreases rapidly when the tube gets longer compared to its cross-section area [37]. The tube length is given because it has to have a certain length to build in a shutter to close this entrance when measurements with the open source channel are conducted. Therefore, the hole area should be larger in a future design. The particle reflection coefficient of the coating of the antechamber inner walls has to be very close to 1. Otherwise the particles get absorber by the chamber walls. For the geometry of the NIM antechamber a particle reflection coefficient of 0.999 instead of 1 results in a signal reduction of 30 %.

The impact of the density enhancement behaviour is also visible when measuring with the PFM entrance slit (Chap. 4.3). When the neutral particle beam is directed on the filament bloc or the metal sheet opposite of the filament bloc, the neutral particles get decelerated leading

to an enhanced density in the ionisation region. The purpose of the open source channel is to measure incoming neutral particles and ions directly that they do not interact with the structure of the instrument **Rewrite**. An analysis of the data conducted with the NIM Prototype revealed that a pillar instead of a metal sheet would have been a better choice as a supporting structure because incoming particles get deflected in all directions instead of being channeled towards the central extraction grid.

The FoV analysis of Chap. 2.6 revealed, that NIM's FoV is blocked for angles bigger than 100° from the spacecraft. Simulations showed that during the flybys at the icy moons' NIM has to change very rapidly between thermal and neutral mode. Due to the entrance hole positions of the closed source antechamber, the antechamber is still able to measure also in the FoV of the neutral gas channel although with a reduced signal intensity due to the bad inflow angle for the antechamber. Therefore it is very important to switch between the two modes as fast as possible because during the switch-over time NIM cannot record any spectra resulting in a loss of precious data.

The shutter to close the entrance between the antechamber and the ionisation region is a very important part in the NIM design because when measuring with the open source channel, the aim is to measure neutral particles and ions directly meaning that they should not interact with any surface of the spacecraft. Neutral particles entering through the closed source antechamber will hit multiple times the antechamber's inner walls to get thermalised and have the opportunity to interact with the wall material. With the open source channel, neutral particles and ions enter the ionisation region undisturbed. Therefore it is important to close the entrance to the antechamber properly to guarantee that as less particles as possible enter the ionisation region from the antechamber when measuring with the neutral or the ion mode channel. The shutter is a plate with an opening in the plate. The plate lies in a pocket between the antechamber and the ionisation region. When the shutter is closed, the plate moves to the side and the gas has to flow around the shutter to reach the ionisation region through the antechamber. The amount of gas reaching the ionisation region through this path depends heavily on the gap size between the shutter plate, the pocket and the antechamber. Simulations revealed that with decreasing gap size, the attenuation increases rapidly. A gap size of 0.01 mm results in an attenuation of a factor 600 where a gap size of 0.1 mm results in an attenuation of 25 (Chap. 2.7).

The mechanical and electrical design of the detector was improved (Chap. 3). In the mechanical design, the detector housing was improved to easier assemble the MCPs and the electrical contact of the contact lug to the MCPs was also improved. In the electrical design the Zener diode was replaced by a resistor because the resistor is more robust concerning discharges. It is a step back in the design but because the detector suffered frequently discharges, it was a necessary solution to improve the robustness of the circuitry with regards to discharges.

Finally, the NIM PFM and FS sensors were tested. The sensors were operated with laboratory electronics because in the case of the PFM, there was only very little time to test the whole system before it was delivered to the spacecraft in December 2020 and in the case of the FS instrument, the complete electronics was not ready at the time writing this thesis.

Both sensors showed good performance regarding mass resolution and SNR. The FS sensor

shows with 830 for thermal mode and 706 for neutral mode a slightly better performance regarding mass resolution than the PFM, which has a mass resolution of 757 for thermal mode and 534 for neutral mode respectively. Both sensors showed a SNR of almost 6 decades which is within the requirements of the two sensors. The NIM PFM and FS ion-optical systems showed both a very good ion storage behaviour. The reason lies in the special designed ion storage source consisting of ring electrodes to store the electrons in 2 directions where the ionising electron beam traps the generated ions in the third direction generating a potential trap for the ions.

In conclusion, the NIM PFM and IS sensor were successfully tested. Different subcomponents were qualified and the analysis showed different drawback which future designers of such instruments may should take care of a bit more than we did.

6. Outlook

The NIM PFM was successfully delivered to the JUICE spacecraft in December 2020 and at the current state, the NIM FS model waits until the JUICE spacecraft started its journey to Jupiter in September 2022. Until then, the FS waits as it is the spare model for the case that something happens to the PFM on the spacecraft until launch. After the start of the spacecraft, the NIM FS has to be properly calibrated with the actual flight electronics. Most results presented in this thesis were conducted with laboratory electronics attached to the two sensors because there was only very little time to test the whole system. The NIM ion-optical system was first qualified as a separate unit and now there follows the calibration of the whole NIM instrument.

In addition, the flight software is still under development and has to be tested with the full system. The optimizer to optimized the voltage sets during the flight is still under development. As soon as it is available for tests, it has to be tested and the target function used to improve the voltage sets has to be adapted for NIM. First results of the FS sensor operated with flight electronics revealed that there lies a lot of potential in the postprocessing of the data especially in regards to filtering. Therefore a proper filter has to be written to improve the SNR of the final spectra.

References

- [1] D. Abplanalp. Development of a sensitive TOF-Mass Spectrometer for Space Research. Universität Bern, 2009.
- [2] D. Abplanalp, P. Wurz, L. Huber, I. Leya, E. Kopp, U. Rohner, M. Wieser, L. Kalla, and S. Barabash. A neutral gas mass spectrometer to measure the chemical composition of the stratosphere. Advances in Space Research, 44(7):870–878, 2009. doi: 10.1016/j.asr.2009.06.016. URL <http://dx.doi.org/10.1016/j.asr.2009.06.016>.
- [3] E. S. Agency. A history of astrometry - part i mapping the sky from ancient to pre-modern times. URL <https://sci.esa.int/web/gaia/-/53196-the-oldest-sky-maps>. Accessed: 2021-10-17.
- [4] H. Anderson, P. Wurz, P. Brandt, S. Jaskulek, and S. Barabash. Pep eid-b (se-01).
- [5] J. W. Arblaster. Selected electrical resistivity values for the platinum group of metals Part II: Rhodium and Iridium:. Johnson Matthey Technology Review, 60(1):4–11, 2016. doi: 10.1595/205651316X691618.
- [6] R. Arevalo Jr, Z. Ni, and R. M. Danell. Mass spectrometry and planetary exploration: A brief review and future projection. Journal of Mass Spectrometry, 55(1):e4454, 2020. doi: <https://doi.org/10.1002/jms.4454>. URL <https://analyticalsciencejournals.onlinelibrary.wiley.com/doi/abs/10.1002/jms.4454>.
- [7] H. Balsiger, K. Altwegg, P. Bochsler, P. Eberhardt, J. Fischer, S. Graf, A. Jäckel, E. Kopp, U. Langer, M. Mildner, J. Müller, T. Riesen, M. Rubin, S. Scherer, P. Wurz, S. Wüthrich, E. Arijis, S. Delanoye, J. De Keyser, E. Neefs, D. Nevejans, H. Rème, C. Aoustin, C. Mazelle, J. L. Médale, J. A. Sauvaud, J. J. Berthelier, J. L. Bertaux, L. Duvet, J. M. Illiano, S. A. Fuselier, A. G. Ghielmetti, T. Magoncelli, E. G. Shelley, A. Korth, K. Heerlein, H. Lauche, S. Livi, A. Loose, U. Mall, B. Wilken, F. Gliem, B. Fiethe, T. I. Gombosi, B. Block, G. R. Carignan, L. A. Fisk, J. H. Waite, D. T. Young, and H. Wollnik. Rosina - Rosetta orbiter spectrometer for ion and neutral analysis. Space Science Reviews, 128(1-4):745–801, 2007. ISSN 00386308. doi: 10.1007/s11214-006-8335-3.
- [8] S. Barabash, P. Brandt, P. Wurz, and PEP Team. Particle Environment Package (PEP) for the ESA JUICE mission. In AAS/Division for Planetary Sciences Meeting Abstracts #48, volume 48 of AAS/Division for Planetary Sciences Meeting Abstracts, page 422.06, Oct. 2016.
- [9] A. Boutonnet and G. Varga. JUICE- Jupiter Icy moons Explorer Consolidated Report on Mission Analysis (CReMA), esa document jui-esoc-moc-rp-001 edition, 04 2017.
- [10] G. K. Burgess and R. G. Waltenberg. The emissivity of metals and oxides, II: Measurements with the micropyrometer. Physical Review, 4(6):546–547, 1914. doi: 10.1103/PhysRev.4.546.
- [11] F. Cardarelli. Materials Handbook. Springer-Verlag London, 2008.
- [12] G. Collins and T. C. Johnson. Chapter 37 - Ganymede and Callisto. Elsevier, 2014. URL

- <https://doi.org/10.1016/B978-0-12-415845-0.00037-2>.
- [13] P. D. Desai, T. K. Chu, H. M. James, and C. Y. Ho. Electrical resistivity of selected elements. *Journal of Physical and Chemical Reference Data*, 13(4):1069–1096, 1984. doi: 10.1063/1.555723. URL <https://doi.org/10.1063/1.555723>.
 - [14] ESA. Juice mission. URL http://www.esa.int/spaceinimages/Images/2017/07/Juice_mission. Accessed: 2017-10-07.
 - [15] R. G. Fausch. Mass Spectrometry for In Situ Planetary Research. Universität Bern, 2020.
 - [16] R. G. Fausch, P. Wurz, M. Tulej, J. Jost, P. Gubler, M. Gruber, D. Lasi, C. Zimmermann, and T. Gerber. Flight electronics of gc-mass spectrometer for investigation of volatiles in the lunar regolith. In 2018 IEEE Aerospace Conference, pages 1–13, 2018. doi: 10.1109/AERO.2018.8396788.
 - [17] M. Fohn, A. Galli, A. Vorburger, M. Tulej, D. Lasi, A. Riedo, R. G. Fausch, M. Althaus, S. Brungger, P. Fahrner, M. Gerber, M. Luthi, H. P. Munz, S. Oeschger, D. Piazza, and P. Wurz. Description of the Mass Spectrometer for the Jupiter Icy Moons Explorer Mission. IEEE Aerospace Conference Proceedings, 2021-March, 2021. ISSN 1095323X. doi: 10.1109/AERO50100.2021.9438344.
 - [18] P. V. GmbH. Quadrupole mass filter. URL <https://www.pfeiffer-vacuum.com/en/know-how/mass-spectrometers-and-residual-gas-analysis/quadrupole-mass-spectrometers-qms/>. Accessed: 2021-10-12.
 - [19] S. Graf, K. Altweg, H. Balsiger, A. Jäckel, E. Kopp, U. Langer, W. Luithardt, C. Westermann, and P. Wurz. A cometary neutral gas simulator for gas dynamic sensor and mass spectrometer calibration : Space simulations in laboratory: Experiments, instrumentation, and modeling. *Journal of Geophysical Research*, 109, 2004.
 - [20] C. R. G. Wells, H. Prest. Technical Note: Signal, Noise and Detection Limits in Mass Spectrometry. Agilent Technologies. doi: 5990-7651EN.
 - [21] A. E. Hedin, C. P. Avery, and C. D. Tschetter. An analysis of spin modulation effects on data obtained with a rocket-borne mass spectrometer. *Journal of Geophysical Research*, 69(21):4637–4648, nov 1964. doi: 10.1029/jz069i021p04637. URL <https://doi.org/10.1029%2Fjz069i021p04637>.
 - [22] R. W. L. P. E. Ho, C. Y. Powell. Thermal conductivity of the elements.
 - [23] L. Hofer. Development of the gas chromatograph – mass spectrometer to investigate volatile species in the lunar soil for the Luna-Resurs mission. Universität Bern, 2015.
 - [24] H. Hussmann, P. Palumbo, R. Jaumann, M. Dougherty, Y. Langevin, G. Piccioni, S. Barabash, P. Wurz, P. van den Brandt, L. Gurvits, L. Bruzzone, J. Plaut, J. Wahlund, B. Cecconi, P. Hartogh, R. Gladstone, L. Iess, D. Stevenson, Y. Kaspi, O. Grasset, and L. Fletcher. JUICE JUpiter ICy moons Explorer: Exploring the emergence of habitable worlds around gas giants, volume ESA/SRE. ESA, 2014. Definition Study Report.
 - [25] B. Johnson. Power sources for space exploration. URL <http://large.stanford.edu/>

- courses/2012/ph240/johnson1/. Accessed: 2021-10-12.
- [26] D. Lasi, M. Tulej, S. Meyer, M. Lüthi, A. Galli, D. Piazza, P. Wurz, D. Reggiani, H. Xiao, R. Marcinkowski, W. Hajdas, A. Cervelli, S. Karlsson, T. Knight, M. Grande, and S. Barabash. Shielding an mcp detector for a space-borne mass spectrometer against the harsh radiation environment in jupiter’s magnetosphere. *IEEE Transactions on Nuclear Science*, 64(1):605–613, 2017. doi: 10.1109/TNS.2016.2614040.
 - [27] E. Lassner and W.-D. Schubert. *Tungsten*. Springer US, 1999.
 - [28] W. R. McMahon and D. R. Wilder. High temperature spectral emissivity of yttrium, samarium, gadolinium, erbium and lutetium oxides. 1 1963. URL <https://www.osti.gov/biblio/4704246>.
 - [29] S. Meyer. *Development of Fully Automated and Highly Precise Data Analysis for a Miniaturized Laser-Ablation Mass Spectrometer*. Universität Bern, 2013.
 - [30] S. Meyer. *Development of a Neutral Gas-and Ion-Mass Spectrometer for Jupiter’s Moons*. Universität Bern, 2017.
 - [31] S. Meyer, M. Tulej, and P. Wurz. Mass spectrometry of planetary exospheres at high relative velocity: direct comparison of open- and closed-source measurements. *Geoscientific Instrumentation, Methods and Data Systems*, 6(1):1–8, 2017. doi: 10.5194/gi-6-1-2017. URL <https://gi.copernicus.org/articles/6/1/2017/>.
 - [32] N. Milosevic, G. Vukovic, D. Z. Pavicic, and K. Maglic. Thermal properties of tantalum between 300 and 2300 k. *International Journal of Thermophysics*, 20:1129–1136, 1999.
 - [33] M. B. Neuland. *In situ mass spectrometry for planetary exploration: Quantitative chemical composition measurements on planetary surfaces*. Universität Bern, 2015.
 - [34] S. Scherer. *Design of a high-performance Reflectron Time-of-Flight mass spectrometer for space applications*. Universität Bern, 1999.
 - [35] S. Scherer, K. Altwegg, H. Balsiger, J. Fischer, A. Jäckel, A. Korth, M. Mildner, D. Piazza, H. Reme, and P. Wurz. A novel principle for an ion mirror design in time-of-flight mass spectrometry. *International Journal of Mass Spectrometry*, 251(1):73–81, 2006. ISSN 1387-3806. doi: <https://doi.org/10.1016/j.ijms.2006.01.025>. URL <https://www.sciencedirect.com/science/article/pii/S1387380606000510>.
 - [36] M. C. Sitja and A. E. Lopez. Pep nim field of view obstruction study.
 - [37] D. van Essen and W. C. Heerens. On the transmission probability for molecular gas flow through a tube. *Journal of Vacuum Science and Technology*, 13(6):1183 – 1187, 1976.
 - [38] A. Vorburger and P. Wurz. Europa’s ice-related atmosphere: The sputter contribution. *Icarus*, 311:135–145, 2018. ISSN 0019-1035. doi: <https://doi.org/10.1016/j.icarus.2018.03.022>. URL <https://www.sciencedirect.com/science/article/pii/S0019103517305377>.
 - [39] A. Vorburger, P. Wurz, H. Lammer, S. Barabash, and O. Mousis. Monte-Carlo simulation of Callisto’s exosphere. *Icarus*, 262:14–29, 2015. ISSN 10902643. doi: 10.1016/j.icarus.

2015.07.035.

- [40] D. D. R. Williams. Jupiter. URL <https://nssdc.gsfc.nasa.gov/planetary/planets/jupiterpage.html>. Accessed: 2021-10-17.
- [41] J. Wiza. Microchannel plate detectors. Nuclear Instruments and Methods, 162(1): 587–601, 1979. ISSN 0029-554X. doi: [https://doi.org/10.1016/0029-554X\(79\)90734-1](https://doi.org/10.1016/0029-554X(79)90734-1). URL <https://www.sciencedirect.com/science/article/pii/0029554X79907341>.
- [42] M. Wüest, D. S. Evans, and R. von Steiger. Calibration of Particle Instruments in Space Physics. 2007.
- [43] P. Wurz. Lecture notes mass spectrometry and ion optics, 2017.
- [44] P. Wurz, D. Abplanalp, M. Tulej, and H. Lammer. A neutral gas mass spectrometer for the investigation of lunar volatiles. Planetary and Space Science, 74(1):264–269, 2012. ISSN 0032-0633. doi: <https://doi.org/10.1016/j.pss.2012.05.016>. URL <https://www.sciencedirect.com/science/article/pii/S0032063312001298>. Scientific Preparations For Lunar Exploration.

A. Appendix

A.1. Papers

A.2. Datasheets

Chevron MCP and Detector Initial Start-up and Electrical Test Procedure

NOTES: Read the entire start-up procedure before applying any voltages.

Refer to Diagram 1 - Typical Wiring Diagrams - for each detection mode.

The suggested bias voltage for a Resistive Anode Encoder (RAE) is 300 volts.

CAUTION:

Do not exceed 1000V per Microchannel Plate (MCP) for 40:1 aspect ratio MCPS. 1200V/MCP for 60:1 aspect ratio MCPS.

When installing flange mounted detectors gradually tighten the bolts in a star pattern (DO NOT exceed 20 foot-pounds per bolt). Failure to do so could cause the fiberoptic to crack.

RECOMMENDATIONS:

For optimal lifetime, operate the detector at the minimum voltage necessary to obtain a useable signal.

Do not operate the phosphor screen at a higher than recommended potential.

PROCEDURE

Make all connections to the assembly.

Check all electrical connections for possible shorted or open circuits.

Pump down to 2×10^{-6} torr and hold for at least 15 hours.

VOLTAGE APPLICATION

Electron/Negative Ion/UV Photon Detection: (for a metal anode or Resistive Anode Encoder, skip to next section)

Phosphor Screen

Ground the input of the assembly (V_i). Apply voltage to the phosphor screen (V_a) in +250V, 1 minute increments. Stop at +1.0 kV.

Apply voltage to the output of the assembly (V_o) in +100V, 2 minute increments. Stop at +1.0 kV.

Increase the voltage to V_a in +100V, 5 minute increments to +3.0 kV. Wait 5 minutes.

Increase the voltage to V_a in +100V, 10 minute increments to +4.0 kV. Wait 5 minutes.

Simultaneously increase the voltage to V_a and V_o in +100V, 10 minute increments to +4.5 kV at V_a and +1.5 kV at V_o .

For screens requiring a 5.0 kV potential - Increase the voltage to V_a in +100V, 10 minute increments to +5.5 kV. Wait 10 minutes.

For screens requiring a 5.0 kV potential - Increase the voltage to V_a in +50V, 10 minute increments to +6.5 kV. Wait 10 minutes.

Simultaneously increase the voltage to V_a and V_o in +50V, 10 minute increments to +2.0 kV at V_o .

When through using the detector, turn off the voltage to V_a . When the voltage drops below +2.0 kV, turn off the voltage to V_o .

Metal Anode/Resistive Anode Encoder

Ground the input of the assembly (V_i). Apply the specified anode bias to V_a .

Increase the voltage to both V_a and V_o in +100V, 2 minute increments by +1.0 kV at V_a and to +1.0 kV at V_o . Wait 5 minutes.

Increase the voltage at V_o and V_a in +100V, 5 minute increments to +1.5 kV at V_o . Wait 10 minutes.

Increase the voltage at V_o and V_a in +50V, 5 minute increments to +2.0 kV at V_o .

When through using the detector, turn off the voltages to V_o and V_a .

Positive Ion/UV Photon Detection (for a metal anode or Resistive Anode Encoder, skip to next section).

Phosphor Screen

Ground the output of the assembly (V_o). Apply voltage to the phosphor sheen (V_a) in +250V, 1 minute increments. Stop at +1.0 kV.

Apply voltage to the input of the assembly (V_i) in -100V, 2 minute increments. Stop at -1.0 kV.

Increase the voltage to V_a in +100V, 5 minute increments to +2.0 kV. Wait 5 minutes.

Increase the voltage to V_a in +100V, 10 minute increments to +3.0 kV. Wait 5 minutes.

Adjust the voltage to V_i in -100V, 10 minute increments to -1.5 kV.

For screens requiring a 5.0 kV potential - Increase the voltage to V_a in +100V, 10 minute increments to +4.0 kV. Wait 10 minutes.

For screens requiring a 5.0 kV potential - Increase the voltage to V_a in +50V, 10 minute increments to +5.0 kV. Wait 10 minutes.

Adjust the voltage to V_i in -50V, 10 minute increments to -2.0 kV.

When through using the detector, turn off the voltages to the V_i and V_a .

Metal Anode/Resistive Anode Encoder

Ground the output of the assembly (V_o). Apply the specified anode bias to V_a .

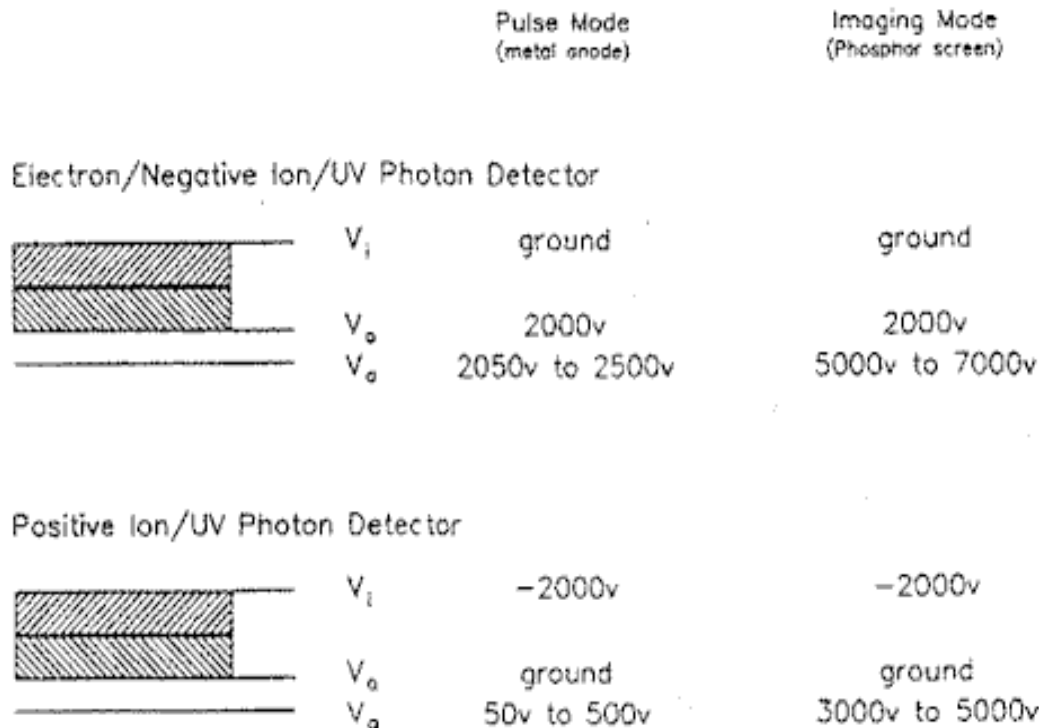
Apply voltage to V_i in -100V, 2 minute increments. Stop at -1.0 kV. Wait 2 minutes.

Adjust the voltage at V_i in -100V, 5 minute increments to -1.5 kV. Wait 5 minutes.

Adjust the voltage at V_i in -50V, 10 minute increments to -2.0 kV.

When through using the detector, turn off the voltages to V_i and V_a .

TYPICAL WIRING DIAGRAMS



Acknowledgement

My thanks go to:

Prof. Dr. Peter Wurz for the opportunity to work on the NIM instrument giving me a very good insight on how such projects work. The work was very instructive from the physical and the technical point of view. I also appreciated the educational discussions.

Stefan Meyer who introduced me to the NIM instrument and made me familiar with all the other teams members.

Harald Mischler and the team from the mechanic's workshop of the University of Bern and also to my office colleagues Georg Bodmer, Adrian Etter and Joël Gonseth for their technical support in the laboratory and the amusing discussions in our office.

Daniele Piazza, Michael Gerber and Stefan Brüngger from the mechanical construction.

Matthias Lüthi, Severin Oegschger, Andreas Nentwig, Michael Althaus, Philipp Fahrer and Hans Peter Munz for the electronics workshop.

André Galli as an office mate and also for the very stimulating discussions especially during the time writing this thesis.

The Wabschli-WG namely Marc Trautmann, Jonathan Gasser, Viviane Tanner and Sabrina Waldburger.

My family

The members of the Dinner's club, the Friday beer and the Alpweeked. Especially Lukas Jaun.

Colleagues at the institute for their

Erklärung

gemäss Art. 28 Abs. 2 RSL 05

Name/Vorname: Föhn Martina

Matrikelnummer: 11-105-145

Studiengang: Master of Science in Physics

Bachelor ☐ Master ☒ Dissertation ☐

Titel der Arbeit: Application of Surface Physics for Instruments in Space Science

LeiterIn der Arbeit: Prof. Dr. Peter Wurz

Ich erkläre hiermit, dass ich diese Arbeit selbständig verfasst und keine anderen als die angegebenen Quellen benutzt habe. Alle Stellen, die wörtlich oder sinngemäss aus Quellen entnommen wurden, habe ich als solche gekennzeichnet. Mir ist bekannt, dass andernfalls der Senat gemäss Artikel 36 Absatz 1 Buchstabe r des Gesetzes vom 5. September 1996 über die Universität zum Entzug des auf Grund dieser Arbeit verliehenen Titels berechtigt ist. Ich gewähre hiermit Einsicht in diese Arbeit.

Ort/Datum

Unterschrift